Blocking Endocytosis:
A Novel Cancer Treatment

Elham Bidram

Submitted in total fulfilment of the requirements of the degree of

Doctor of Philosophy

September 2016

Department of Chemical & Biomolecular Engineering

The University of Melbourne

Dedicated to

My lovely husband

Rouhollah

And

My dearest family

My parents and brothers

Abstract

The ultimate purpose of current cancer research is to develop a comprehensive series of personalised treatments for different cancers. One approach involves investigating the capacity of delivery systems and pharmaceutical conjugations for cancer treatment with the purpose of limiting adverse effects and toxicity. To this end, targeted delivery has been widely investigated for tumour therapy, as it has the potential to improve therapeutic efficiency and reduce adverse effects. However, these therapies can still cause adverse effects if the transported anti-cancer drugs interact with the non-tumour cells. Consequently, this thesis develops a novel therapeutic system utilising graphene oxide (GO) polymer and ligands for certain receptors known to be over-expressed on tumour cells. These reagents are designed to block endocytosis in tumour cells, resulting in cell metabolic deprivation and death.

To develop a selectively cytotoxic therapeutic system, modified GO networks were synthesised and tested. Folic acid (FA) and arginylglycylaspartic acid (RGD) ligands on the polymeric networks target and capture tumour cells, blocking the targeted over-expressed receptors, resulting in cell metabolic deprivation and death.

Due to the importance of particle size in therapeutics, a facile separation method, glycerol gradient density, was developed to discretely separate the GO polymers into appropriate sizes. This method successfully fractionated and separated the GO sheets into a wide range of sizes from 150 nm to 850 nm.

To develop a simple surface functionalisation, polyethylene glycol (PEG) was employed to modify the GO polymer and provide a bifunctional polymeric linker PEG serves to reduce the steric hindrance between the ligand and receptor, and so allows the attached ligand greater freedom of movement.

To understand the impact of the modified GO networks on cellular function, confocal live imaging was performed, exploiting the fluorescence properties of GO and its derivatives. Upon incubation of these networks with tumour cells, varied behaviour was observed depending on the surface chemistry of the attached ligand. FA-modified GO was taken up by the treated cells, whereas the RGD and FARGD-modified GO

behaved differently and associated to the cell membrane, without showing any evidence of internalisation.

The cytotoxicity of modified GO networks on three different cell lines, tumour (KB) and non-tumour (BEAS-2B, fibroblast) cells was also examined using a cell proliferation/toxicity assay (WST assay). Using modified GO networks resulted in a 35% reduction in tumour cell viability, whereas the viability of the non-tumour cells was decreased by only 20% and 10%, respectively. This latter effect was attributed to diminished cell proliferation rate: BEAS-2B cells, transformed non-tumorigenic epithelial cells, are able to highly proliferate, while the lung fibroblast is a non-tumour connective tissue cell with a normal proliferation rate.

To investigate the potential for synergy, a combination of modified GO with two common anti-cancer drugs, methotrexate (MTX) and doxorubicin (DOX), was studied. This combination showed cytotoxicity of up to 80%, compared to a 35% and 50% toxicity for modified GO, and MTX and DOX, respectively.

Combinations of modified GO polymeric networks provide a promising therapeutic system for cancer therapy and imaging applications.

Declaration

This is to certify that this thesis comprises only the original work by the author towards the degree of Doctor of Philosophy, except where indicated in the preface to duly acknowledge the work of others. This thesis is less than 100,000 words in length, exclusive of tables, figures, bibliography and appendices. To my knowledge, this work contains no material previously published or written by others.

Elham Bidram

Mar 2017

Preface

This work was carried out in the Complex Fluid and Polymer Science Laboratories, Department of Chemical and Biomolecular Engineering, and Immunopharmacology laboratory, Department of Pharmacology and Therapeutics, School of Biomedical Sciences, The University of Melbourne, Australia, under the supervision of Prof. Dave. E. Dunstan and Prof. Alastair Stewart. The project was funded by the University of Melbourne and Australian government.

Chapter 3 of this thesis has been published in the following article:
E Bidram, A Sulistio, A Amini, Q Fu, GG Qiao, A Stewart and D. E. Dunstan., *Fractionation of Graphene Oxide Single Nano-Sheets in Water-Glycerol Solutions using Gradient Centrifugation*. Carbon **2016** (103), 363-371.

Chapter 4 of this thesis has been published in the following article:
E Bidram, A Stewart and D. E. Dunstan., *Graphene Oxide as a photoluminated carrier*. Materials Today: Proceedings 2016 (3) 240-244.

Chapter 5 of this thesis has been submitted as the following article:
Elham Bidram, Adrian Sulistio, Hyun-Jung Cho, Trudi Harris, Greg Qiao, alastair stewart., *Starving Cancer cells by blocking endocytosis with graphene oxide*. Materials Today Communications 2017.

In chapter 3, NMR spectroscopy was carried out by Dr. Adrian Sulistio from polymer science group and TGA and XPS was conducted by Hao Wei and Alex Duan respectively from School of Chemistry and TEM imaging was carried out by Dr Simon Crawford, School of BioSciences.

In chapter 5, CLSM imaging was carried out with the assistance of Dr. Ellie Cho from Biomedical school.

Acknowledgments

Firstly, I would like to express my appreciation to my supervisor Prof. Dave Dunstan for giving me the opportunity to pursue my PhD in his laboratory. I thank him for his generous provision of financial and scientific supports during my candidature. He gave me freedom to think, analyse and direct the project. I would also like to thank my co-supervisor Prof. Alastair Stewart for giving me the chance to be a part of his group and for his amazing patience and expert guidance. I also would like to thank Mrs Trudi Harris for many hours of hands-on assistance and more importantly teaching me how to design the experiments actively and skilfully.

Thanks to my PhD committee members Prof. Greg Qiao and Prof. George Frank, University of Melbourne for their support and guidance. I would like to thank Dr. Adrian Sulistio from polymer science group for his valuable contribution in materials preparation. He was always available for helpful discussions and directions.

I am thankful to all past and present members of the lab particularly Sian-Yang, Halleh, Dylan, Kenneth and Donglin and wish them all the best in their future research. I would like to appreciate the assistance of the Alastair lab members specially Nuha, Asmaa, Meina, Danica for their wonderful friendship and the lab Post-Docs Christine Ruth Keenan and Michael Jerome Schuliga for giving me motivations with a big smile. A special thanks to Shenna Langenbach, Alastair Research Assistant for her kind technical assistance during the project. Also thankful for the support received from other students and staff in the Department of Chemical Engineering, and Pharmacology and Therapeutics.

I am thankful of my parents since I have many of my management skills and problem solving ability from them. I owe to them a lot teaching me how to be patient and hard working in difficulties. I appreciate their generous soul since even I was far from them and they missed me but always encouraged me. Thanks to my brothers, for their kindness, understanding and support in all my life. Whilst we have all been separated by distance, they have never been far from my thoughts.

Lastly, I would like to express my sincere gratitude and special thanks to my beloved husband, Rouhollah for bearing me through the thick and thin and for being a true friend. He always listened to me when I was down and helped to cheer me up and encourage me to continue with the research. Thanks to him for bearing my frustrations,

sharing my worries and without him, I would have never fulfilled this dream. I wish him all the best of luck and success in his future endeavour.

Table of Contents

List of Tables

List of Figures

Abbreviations

EPR	Enhanced permeability and retention
FA	Folic acid
FR	Folate receptor
GO	Graphene oxide
NDT	Nanoparticle-drug therapy
CPT	Camptothecin
DDS	Drug Delivery System
DOX	Doxorubicin
ECM	Extra Cellular Matrix
MTX	Methotrexate
PEG	Polyethylene glycol
RES	Reticulo-endothelial system
RGD	Arginylglycylaspartic acid
AFM	Atomic Force Microscopy
NMR	Nuclear Magnetic Resonance
SEM	Scanning electron microscope
SFM	Scanning-force microscopy
SPM	Scanning probe microscopy
TEM	Transmission electron microscope
TGA	Thermal Gravimetric Analysis
FTIR	Fourier transform infrared spectroscopy
IR	Infrared spectroscopy
DLS	Dynamic Light Scattering
RI	Refraction Index
DMEM	Dulbecco's Modified Eagle Medium
DMF	Dimethylformamide
MTS	Colorimetric cell viability assay
MWCO	Molecular weight cut-off

NIR	Near-infrared
PBS	Phosphate Buffered Saline
WST	Cell Proliferation assay
XPS	X-ray photoelectron spectroscopy
DAPI	4',6-diamidino-2-phenylindole
FITC	Fluorescein isothiocyanate
DMAP	4-Dimethylaminopyridine
EDC	1-Ethyl-3-(3-dimethylaminopropyl)carbodiimide
TCEP	Tris (2-carboxyethyl) phosphine hydrochloride

Journal papers and conferences

Journal papers

1) Fractionation of graphene oxide single nano-sheets in water-glycerol solutions using gradient centrifugation. Carbon (103) 363-371. 2016.

2) Graphene Oxide as a Photoluminated Carrier. Materials Today: Proceedings (3) 240-244. 2016.

3) Starving Cancer cells by blocking endocytosis with graphene oxide. Materials Today Communications. Under revision. 2017.

Conference presentations

1) Graphene Oxide as a Photoluminated Carrier. Advances in Functional Materials (Conference 2015), Stony Brook University, USA. Jun 29 - Jul 3, 2015.

2) Graphene Oxide networks as the traceable components. 24th Australian Conference on Microscopy and Microanalysis. Melbourne, Australia. January 31 – Feb 4, 2016.

Chapter 1

Introduction and Literature Review

1 Introduction and Literature Review

1.1 Introduction

Following cardiovascular diseases, cancer is the second biggest cause of death worldwide [1]. Given the seriousness of the issue, it is worthwhile defining cancer. Carcinogenesis is a multistep process in which changes in tissue architecture and in cell phenotype can induce local regions of hypoxia [2-4]. Hypoxia can induce epithelial–mesenchymal transitions (EMT) which is involved in regulating cellular plasticity in carcinomas [5]. This promotes the survival and growth of tissue stem cells and the formation of precancerous and cancerous lesions [6, 7]. The most fundamental traits of tumour cells are their ability to survive beyond their normal life span and to sustain chronic proliferation, whereas the growth of normal tissue is tightly regulated [8-10]. The lack of normal growth control is operative in both early tumour genesis and metastasis [11, 12]. In order to grow exponentially, tumour cells must circumvent pathways that negatively control cell proliferation by evading growth suppressors and resisting programmed cell death (apoptosis) [10, 13]. Apoptotic evasion is one of the hallmarks of cancer and appears to play a key role in inducing resistance to both chemotherapy and radiotherapy [7, 14].

Remarkable progress has been made towards a better understanding of cancer development, which has led to remarkable advances in cancer treatment [15-18]. However, cancer is an aggressive disease that is difficult to treat due to several reasons, including major inter- and intra-tumour heterogeneity, and mutations in hundreds of different genes contributing to cancer [19, 20]. Further, cancer can affect a wide range of cells (e.g., epithelial, stromal, blood-based) and organs in the body [2, 21]. In addition, cancer is generally not a static disease but evolves and progresses over time accumulating new mutations [22]. Traditional cancer treatment modalities comprise radiation therapy, surgery, chemotherapy and proton therapy (Table 1). Radiation therapy, despite causing side effects, remains an important component of cancer treatment for at least 50% of all cancer patients [23]. Chemotherapy, which utilises cytotoxic drugs, likewise inevitably damages normal tissue surrounding the tumour [24, 25]. Chemotherapeutic agents target cells with a high basal level of proliferation and regeneration, including tumour cells and non-tumour rapidly proliferating cells found in

the skin, hair, bone marrow and epithelium of the gastrointestinal tract [26-28]. This causes the high level of cytotoxicity associated with such treatments [26, 27]. Furthermore, a variety of long-term complications often follow conventional cancer therapies, such as cardiotoxicity, neurotoxicity, infertility, and chronic liver damage [28].

Table 1. Summary of major traditional cancer therapies looking at their positive and negative aspects.

Strategy	Definition	Positive points	Negative points	References
Surgery	Removal of cancerous tissue	Removing a clearly localised tumour	Invasion of cancer cells into other tissues, high risk of recurrence, location dependent, permanent disfigurement, complications due to surgery (during or after)	**[29-32]**
Chemotherapy	Using cancer drugs (anti-neoplastic agents)	High rate of tumour cells killing	Many side effects because of the lack of targeting	**[29, 32-37]**
Radiation therapy	Killing cancer cells by high-energy radiation	Cancer-fighting in situ	Damage to healthy tissues by an undesirable pattern of energy placement, and side effects due to indiscriminate nature	**[29, 30, 32, 38-40]**
Proton therapy	Using a beam of protons to target the tumour (a precise form of radiotherapy)	Fewer harmful side effects, more direct impact on the tumour, and increased tumour control	Applicable for just some kinds of cancers, Proton beam clinics are very expensive	**[29, 41, 42]**

In order to minimise the side effects of common cancer therapies, this project aims to develop a novel cancer therapeutic system using over-expressed receptors to explore new strategies to fight cancer in a selectively toxic way. Modified polymeric networks using graphene oxide (GO) and two different ligands, i.e. folic acid (FA) and

arginylglycylaspartic acid (RGD) peptide, have been developed for cancer therapy and imaging purposes.

Different aspects of cancer, various cancer therapies, particularly targeted delivery systems, and GO as a recent candidate for cancer therapy and its related applications are described in the following sections.

1.2 Cancer is a Multiple Disease

Unlike apoptotic evasion which was described in section 1.1, tumour angiogenesis, the process of growth and formation of new blood vessels (i.e. neovascularisation), is an essential pathological feature of cancer [43, 44]. To be able to promote neovascularisation, tumour cells have to acquire an angiogenic phenotype, which is believed to occur in the early stages of tumour development [44]. Angiogenesis is crucial for the growth and spread of tumour cells [45, 46]. Although tumour blood vessels are often described as structurally and functionally abnormal, they are functional enough to provide nutrients and oxygen to growing tumours and to support tumour cell dissemination and metastasis [47, 48].

Metastasis is another critical aspect of tumour genesis and the primary reason for the high mortality rate of cancer, being responsible for the majority of cancer-associated deaths [49]. Metastasis is a complex process that requires close collaboration between cancer, immune, inflammatory, and stromal cells [50]. It is generally divided into a number of steps including the detachment of tumour cells from the primary tumour, invasion, migration, survival in the vasculature, and colonisation of the secondary site [51]. Table 2 summarises the main differences between normal and tumour cells.

Table 2. Tumour cells compared to non-tumour cells.

Size	Smaller and rounded shape	[52, 53]
Nuclei	Much bigger than normal cells	[52-54]
Genome	Lack of genomic integrity with different mutations	[55-57]
Cell function	Lose some or all differentiated functions of their parents	[52, 56, 58, 59]
Blood vessels	Disorganised, leaky and irregular blood flow	[53, 57, 60]
Cell membrane composition	Loss of polarity, over-expression of some proteins and receptors	[56, 61-68]
The rate of proliferation	Self-renewable (non-controllable)	[29, 32, 55, 56, 59]

1.3 Novel Cancer Treatments

The traditional treatments of surgery, radiation therapy, chemotherapy and proton therapy for cancer were described in section 1.1. However, new treatments based on nanoparticles, utilisation of specific ligands and the delivery of macromolecular therapeutics, are being potentially developed to provide more effective treatment of cancer [69-71].

1.3.1 Nanotechnology in Cancer Treatment

Nanoparticle-drug therapy (NDT) is a newer type of cancer treatment that utilises drugs along with nanoparticles to more precisely identify tumour cells, and operates as a drug delivery system (DDS) [71, 72]. Nanoparticles can more specifically approach tumour cells due to their size, special properties and the attached targeting ligands [73]. It is hoped this method will improve the pharmacological properties of free drugs and specifically treat tumours with minimal effects on normal tissues [74, 75]. Table 3 illustrates some instances of problems caused by free chemotherapeutic drugs, which are improved by NDT. This treatment can be designed either by directly conjugating the desired drug to a suitable ligand [75], which is then used to target the specific affected area, or by using a macromolecular conjugate to carry both drug and targeting ligand to the tumour [75]. The large capacity of these conjugates allows a higher loading of drugs compared to ligand-drug systems carrying just one molecule of

the drug [75-77]. Tumour accumulation of NDT depends on the size and circulation time of the targeting system as well as on the tumour type and grade [70, 73, 78-82].

In summary, NDT is designed to increase the efficacy of drugs and improve their bioavailability at the target site [83]. It also improves the stability of drugs while minimising the exposure of noncancerous tissues, which can reduce the common side effects associated with cancer chemotherapies [84].

Table 3. Non- Perfect characteristics of free drugs and improvement of their clinical functions in a DDS [82, 85].

Problem of free drugs	The effect of DDS
Poor solubility and distribution	Providing hydrophilic or hydrophobic environments to increasing solubility and distribution, such as liposomal vincristine [86].
Rapid breakdown and unfavourable pharmacokinetics	Protecting drugs from degradation and enabling slow release, thus decreasing the number of doses administered, such as liposomal amphotericin B [87, 88] and liposomal topotecan [82].
Lack of selectivity and severe side effect	Improve drug selectivity by targeting ligands and concentrating the drug in the affected tissue

Nanoconjugates with distinctive natural and structural properties have been widely investigated for tumour targeted delivery of various compounds (e.g. chemotherapeutic drugs, photosensitizer (PS) molecules, photothermal agents and genetic materials) in order to improve their therapeutic efficiency and reduce negative features [89]. Suitable nanoconjugates (Figure 1-1) include linear polymeric conjugates [90, 91], dendrimers [92, 93], liposomes, micelles, and non-polymer nanoparticles [70, 90, 94, 95].

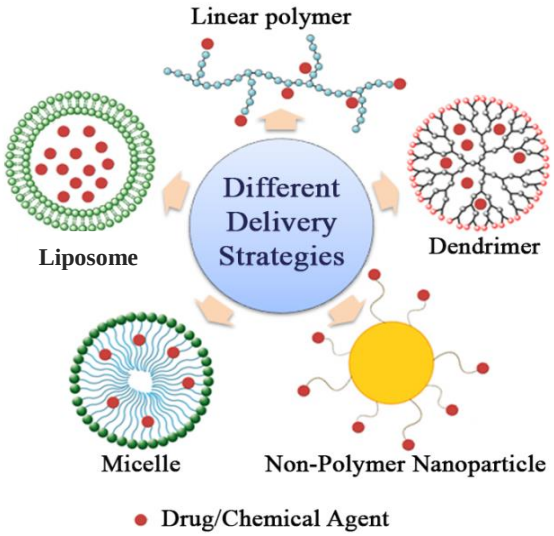

Figure 1-1. Various delivery strategies for drug and chemical agents.

These vehicles are the polymeric structures formed differently based on the specific delivery purposes.

On the other hand, the enhanced permeability and retention (EPR) effect is another parameter to consider in cancer therapy systems. The EPR effect allows certain sizes of therapeutic molecules accumulate in solid tumours [89, 96]. Notably, EPR is not universally present in all tumour types or even in all areas of a tumour, and is often limited by the degree of tumour vascularisation [97]. This means the EPR effect is quite heterogeneous and may exist for only a few types of tumours, or small size cancers [98]. Therefore, the localisation of passive targeted nanoparticles within the tumour can be inconsistent [99]. This heterogeneity also causes higher concentrations of nanoparticles in one part of the tumour, which do not exist in other parts [75]. Consequently, EPR effect enriches the required drugs in the tumour interstitial space, with the higher osmotic pressure leading to drug leakage from the affected tissue [100, 101]. As a result, fewer NDT nanoparticles are accumulated in proangiogenic or necrotic tumours [102, 103].

Overall, the accumulation of the designed nanoparticles in specific tumours depends on their size, chemical characteristics, and circulation time [104]. This accumulation is improved by choosing the appropriate targeting ligands (active targeting strategies) and and the degree and intactness of the vasculature [59, 97].

1.3.2 Ideal Ligands in Cancer Therapy

The first significant point in cancer targeted therapy is that the ideal markers to be targeted need to be uniquely highly expressed on tumour cells with a lower expression on non-tumour cells [105]. Table 4 lists tumour markers for various tumour types. Another important criterion in the selection of appropriate targeting ligands is whether the targeted nanoconjugates can be internalised into the directed cells [59, 106]. Further, the targeted marker needs to be easily accessible to the designed conjugates [105]. Over-expressed markers/receptors on the cell surface are better candidates for targeted therapy compared to some intracellular ones, such as steroid or retinoic acid receptors [100]. When an ideal marker is identified for targeting purposes, a ligand with appropriate specificity, binding affinity, proper size and functional group availability must be chosen for receptor-targeted delivery [105]. Different types of ligands have been used for delivery of nanoconjugates to the targeted tumour cells [107]. The most commonly utilised ligands include antibodies, oligosaccharides, cationic and short peptides/motifs (e.g. RGD) and some vitamins such as FA or biotin [108-110]. These molecules interact with higher expressed receptors or proteoglycans, promoting cellular uptake via endocytosis [38–45]. In the wide range of the appropriate targeting compounds, antibody-based delivery systems are one of the most successful molecules in drug delivery purposes [111]. However, these systems face some hitches such as immunogenicity, unreasonable cost, and complex conjugation chemistry [112].

Table 4. Tumour markers by tumour type.

Marker	Cancerous tissue	References
CD98hc (SLC3A2)	Renal cancer	[113]
CD133/AC133 cell surface markers	Variety of cancers, especially brain, ovary and colon cancer	[39, 55, 61, 62]
CD44 cell surface markers	Variety of cancers	[61, 114]
CXCL12 and its receptor	Brain cancer	[115]
CXCR4	Brain cancer	[115, 116]
CD34+/CD38−cell population	Acute myeloid leukaemia and skin tumour	[56, 57]
CD44+/CD24−/lineage−cells	Breast cancer	[56, 114, 117]
Epidermal growth factor receptor (EGFR)	Majority of cancers	[33, 118]
Fibroblast growth factor receptor (FGFR),	Prostate	[33]
Folate receptor (FR)	Majority of cancers	[119-123]
Insulin-like growth factor (IGF1)	Thyroid, brain, intestine, kidney, breast and prostate	[124]

In general, affinity and density, which are the two essential properties of ligands, play a crucial role in the effective targeting of delivery systems to the affected tumour area [125]. For instance, higher ligand density does not necessarily lead to higher intracellular accumulation [126]. The higher densities affect the surface characteristics (i.e. charge ratio), thus influencing the cellular uptake [78]. Given this, the best ligand density and charge ratio on the nanocarrier surface must be considered. Moreover, the method by which the ligands are attached to the nanoparticles can also affect the optimal ratio of the targeting ligand [126].

Two methods are involved in the preparation of targeted nano-systems: “post-coupling” and “pre-coupling” techniques [127]. The first method is bioconjugation of the targeting ligands to the prepared nanoparticle surface [128]. This technique does not allow the optimal efficiency for ligand-nanoparticle surface density [129]. On the other hand, the most efficient chemical technique is “pre-coupling”, which involves pre-conjugation of a targeting ligand to the base carrier with nano-formulation. This method

provides more homogenously targeted nanosystems capable of controlling ligand/nanoparticle ratios [130]. Clearly, a combination of factors influences the efficiency of nanosystem–tumour cell association, which in turn affects the biological behaviour [78, 95, 131]. These factors include the targeting ligand as well as the size, shape and structure of the applied nanoconjugate [78, 132]. The balance of the ligand/nanoparticle surface ratio also affects the association of nanocarriers and targeted cells which need to be investigated in developing NDT therapies [95].

1.3.3 Folate-Mediated Delivery of Macromolecular Therapeutics

Folate receptor (FR) is considered an attractive targeting site for tumour–specific therapeutics as it is over-expressed in the majority of tumour cells [34, 70, 133-156]. This receptor not only assists ligand association of the therapeutic conjugates on the cell surface, but also acts as a carrier for transferring extracellular drugs/nanocarriers inside of the cells [123, 157].

FR is present on some special non-tumour cells in particular tissues which raises concerns about using this receptor in therapeutic applications [31]. Notably, FR expression is restricted to the apical sides (the side toward the lumen) of polarised epithelial cells (face to body cavities) and would be unapproachable to intravenous drugs [100]. In the kidney, for instance, FR is detectable only on the apical/luminal side (the inside space of a tubular structure) of the proximal tubule polarised cells. This possibly helps in re-absorption of the small amount of FA from urine [158]. In the brain, FR is expressed on the brain side of the blood-brain barrier where it might collect FA inside the cerebrospinal fluid [159]. While FR is also expressed on activated macrophages [37, 160], this is not a major concern, because activated macrophages are replaced by resting macrophages, which cannot bind to FA and its conjugates [161]. Therefore, the transport of some FA-conjugates into the activated macrophages is probably not a serious threat. Upon malignant transformation, however, this apically regulated receptor spreads over the whole cell surface and is consequently available to administered drugs and nanocarriers [100]. Moreover, FA (FR ligand) with the molecular weight of 441 g mol^{-1} is one of the large numbers of small molecules being considered as potential targeting ligands [162]. These molecules are organic molecules with a molecular weight as low as 500 g mol^{-1} and considered as a promising class of

targeting ligands due to their size, high stability, simple coupling chemical procedure and low production cost [95]. The possible modulation of their densities contributes to the stability, size, morphology and targeting efficiency of the designed nanosystems [95]. Several types of folate-therapeutic systems have been developed for *in vivo* delivery of drugs or diagnostic molecules to FR-over-expressed tumour cells (Table 5).

Table 5. Summary of various cancer treatments using folate as a targeting ligand.

Delivery strategy	Type of carrier	Treatment method	Therapeutic agent	Reference
Dendrimer	Polyamidoamine	Gene therapy	siRNA	[163]
	Polyamidoamine	NDT	Antisense oligonucleotides	[164]
Liposome	Thermosensitive bubble-generating	NDT/ Photodynamic therapy	Doxorubicin/ IR780	[165]
	Phosphatidylcholine-cholesterol	Gene therapy	HSV-TK	[166]
Micelle	Polyethylene glycol-b-poly-L-lactide-co-carbonate	NDT	Paclitaxel	[167]
	Poly-2-ethyl-2-oxazoline-b-poly-d,l-lactide	Photodynamic therapy	Meta - tetra (hydroxyphenyl)chlorin	[168]
Non-polymer nanoparticles	Iron Oxide	NDT	Unknown	[169]
	silica–coated upconversion fluorescent nanoparticles	Photodynamic therapy	Zinc (II) phthalocyanine	[170]

1.3.4 RGD-Mediated Delivery of Macromolecular Therapeutics

Integrin is a kind of heterodimer membrane molecule (with two different subunits: α and β) that mediates cell adhesion to the nearby extra cellular matrix (ECM) [171, 172]. The combination of α and β subunits (integrin classes) determines the specificity of integrin-ligand binding and therefore the intracellular signalling [173].

Different integrin classes are expressed on different cell types, such as epithelial, endothelial, fibroblast, and immune cells as well as the different types of tumours [173, 174]. The configuration of ECM around the tumour site and the expression profile of integrin molecules on tumour cells, play a critical role in cancer development, metastasis and treatment difficulties [173, 175]. Tumour cells express many different types of integrins, but αVβ3 and αVβ5 are specifically over-expressed on angiogenic epithelium and in some primary and metastatic tumours [176]. Integrins are targeted by RGD, the short peptide motif consists of three amino acids: arginine (Arg), glycine (Gly) and aspartic acid (Asp) [97, 177]. RGD is one of the most attractive ligands for delivery purposes due to its better cellular uptake and ease of synthesis [95]. It is also sufficiently small with lower immunogenicity and higher stability [178]. As a result, αVβ3 and αVβ5 are considered as the crucial therapeutic targets in integrin targeted cancer therapy [174, 175, 179].

Several studies have investigated a variety of nanosystems containing chemotherapeutic drugs, imaging compounds, chemicals and gene motifs targeting integrins [180, 181] . These nanosystems have shown promising clinical responses in cell association, proliferation and also the circulation time of the designed nanoconjugates in cancer treatments [182, 183] (Table 6). Despite these results, there are some limitations which can restrict using RGD or other oligopeptides in targeting systems. The first issue is that integrins are not cancer specific, being expressed on almost all epithelial cells increases their probable side effects [184]. Since efficient receptor binding depends on the structural features of the targeted ligand [70], even nanoscale spacing alterations through mimicking the native peptide ligand can cause conflict [185, 186] . Further, the RGD density needs to be considered as an important parameter which strongly affects the biological responses, such as binding to the receptor, focal adhesion assembly, migration, and cell proliferation/ differentiation [186, 187]. Nevertheless, there are some recent studies that select intense peptide sequences as targeting molecules with higher affinity to cancer-specific over-expressed classes [184]. Other methods were developed in peptide synthesis to mimic native configurations to overcome the usual small differences which cause cell response variations [186]. Integrin-targeted nanocarriers have recently proven more attractive in

tumour vasculature-targeted therapy, another promising approach to cancer therapy [188].

Table 6. Summary of various treatments using RGD as a targeting ligand.

Delivery strategy	Type of carrier	Treatment method	Therapeutic agent	Reference
Dendrimer	Polyamidoamine	Photothermal therapy	Gold	[189]
	Polyamidoamine	Gene therapy	Plasmid DNA	[190]
	PEGylated polyamide amine	NDT	Doxorubicin	[191]
Liposome	Cationic liposome	Gene therapy	DNA	[192]
	distearoylphosphatldylethanolamine (DSPE), distearoylphosphatidylcholine (DSPC), cholesterol and PEG	NDT	Fluorouracil	[193]
Micelle	Tetra-tail amphiphilic peptide	Photodynamic therapy	Porphyrin	[194]
	Polyethylene glycol-poly lactic acid	Nanoparticle-drug therapy	Antagonists to MDM2 and MDMX	[195]
Non-polymer nanoparticles	Gold	Nanoparticle-drug / Photothermal therapy	Methotrexate	[196]

1.4 Cancer Therapies and Their Challenges

In general, there are two important aspects, which must be considered in cancer therapy: targeted destruction of tumour cells with less impact on non-tumour cells, and more operative retention time in the blood circulation while a reticulo-endothelial system (RES) response is limited [73, 197]. The EPR effect and blocked lymphatic draining in tumour tissues both play a critical role in tumour cell devastation [84, 106, 198]. The multi- functionalized Nano systems showed high delivery efficiency into tumour cells [199]. However, molecules larger than 100 nm cannot access the centre of

a cancer or the inside of tumour cells [198, 200]. The circulation retention time, kidney clearance threshold and RES responsible range all need to be considered when nanoparticles are being designed. Plasma proteins (≥10 nm) usually do not pass the kidney filtration barriers, except in the presence of nephritic disease or other kidney defects [201]. Therefore, chemical conjugations or drugs smaller than the clearance threshold can pass the glomerular filtration barrier and leave the blood stream [202, 203].

RES, on the other hand, recognises any particular system regardless of its size, except for molecules covered with biodegradable shields to disguise them as native macromolecules [204]. Consequently, the appropriate size of the conjugates needs to be considered for delivery purposes [82]. Designed conjugates should be small enough to get through tumour cells without being recognised by the RES [205], but still are sufficiently large to remain in the blood circulation with minimal impact on non-tumour cells [197].

Hydrophilic biodegradable polymers are especially valuable in addressing these issues with passive targeting. Passive targeting takes advantage of the unique pathophysiological characteristics of tumour (EPR effect), assisting nanosystems to accumulate in tumour tissues [206]. For example, polyethene glycol (PEG) is commonly used in DDS due to the wide range of available molecular weights and its hydrophilicity [68, 207]. This biopolymer entraps the conjugation as a hydrophilic cloud repelling the plasma proteins in blood and evading the RES. As a result, the circulation time increases and these particles have the opportunity to slowly accumulate in targeted tissues [68, 208]. Furthermore, PEG is an exceptional linker between the ligand and therapeutic drug (inactive targeting) reducing the stereo-physical inhibition in ligand-receptor association [36, 123, 134, 140, 209-212].

Synthesising appropriate nano-conjugates, based on their size and efficient activity, is the most complex part of DDS design. This requires a high degree of understanding of the physiological and pathological aspects of cancer [95]. To obtain an effective delivery system in cancer therapy, unique combinations of targeting ligands [70, 213, 214] and appropriate polymeric formulations must be considered for each individual type of tumour [71].

1.5 Graphene, a Multi-Disciplinary Polymer

Graphene polymer consists of layers of hexagonal rings in a honeycombed network making up a planar macromolecule [215]. The particular chemical structure of this polymer allows it to be used as a basic building block for other types of carbon molecules from 0D fullerenes, and 1D carbon nanotubes, to 3D graphite (Figure 1-2).

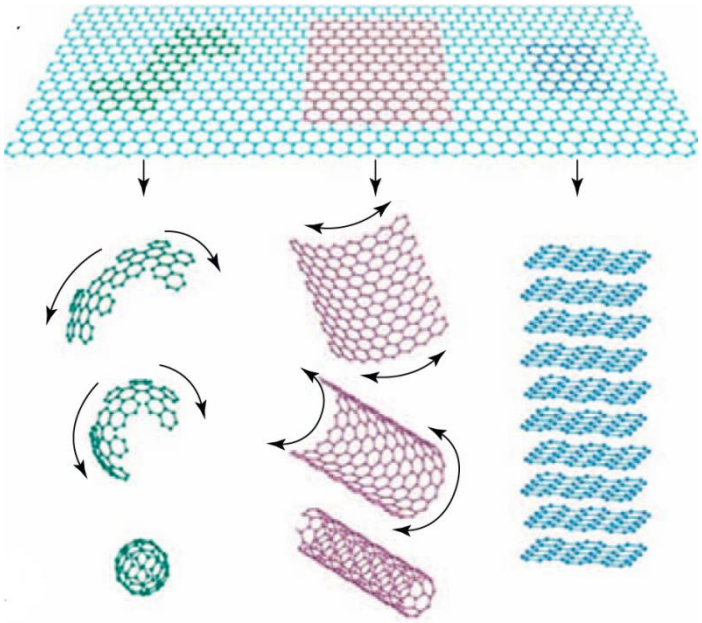

Figure 1-2. Graphene is a 2D molecule for carbon materials that

can be wrapped up into 0D buckminsterfullerene, rolled into 1D nanotubes, or stacked into 3D molecules [216].

Graphene was first prepared in 2004, by peeling a single layer of graphene using sticky tape and a pencil [217]. Over several years, a number of physical and chemical methods have been developed to produce graphene and its derivatised molecules, including exfoliation and chemical synthesis [216, 218].

Chemical modification improves graphene biocompatibility, solubility and selectivity [219]. Graphene Oxide (GO) is a two-dimensional, hydrophilic network made of oxygenated graphene. The wide range of functional groups present allows the surface chemistry to be modified for a number of potential applications in drug delivery and cellular and/or organ targeting [220-223] (Figure 1-3). The combination of the wide range of multifunctional groups with the auto-fluorescence exhibited by this polymer

makes GO attractive for theranostic (combining diagnostic and therapeutic capabilities into a single agent) delivery systems and signalling materials [222, 224, 225]. Hence, a vast amount of research has been directed towards exploring the chemical and physical properties of this unique material for optoelectronic and biomedical applications [226-229].

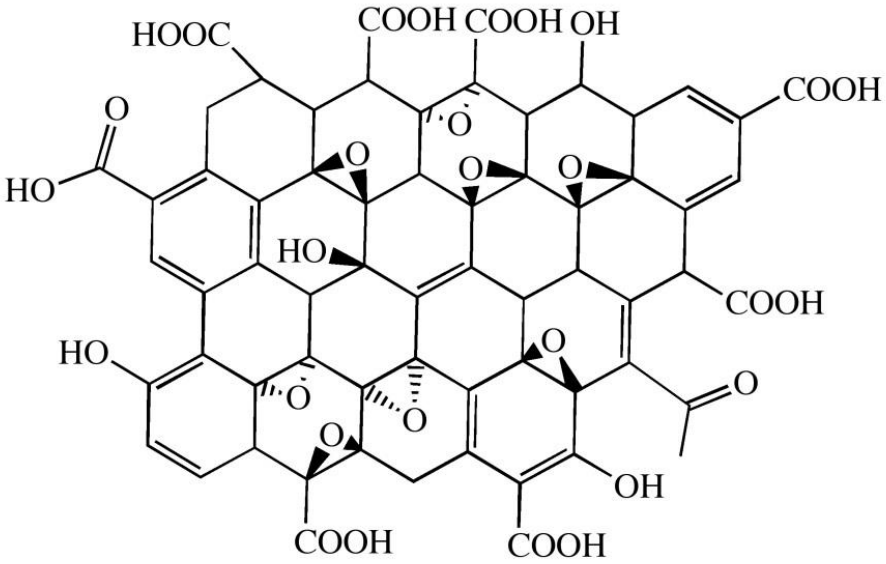

Figure 1-3. The chemical structure of GO exhibiting a variety of functional groups [230] .

1.5.1 GO, an ideal nanomaterial for biological application

The efficacy of existing drug carriers is largely inhibited by their inability to reach appropriate accumulation concentrations in a tumour which is mainly due to partial loading valency and low level of functionalisation [231]. GO is considered a favourable polymer in biomedical studies due to its amphiphilicity, large surface area, an enormous array of functional groups giving a higher degree of functionalisation (through physical adsorption or chemical bonding) and photoluminescence properties [216, 232]. The large 2D aromatic surface of this polymeric network makes it a suitable substrate for adsorption of particular biomolecules [216].

As a result of GO surface functional groups and its secondary structure, GO has also been tethered with various proteins, peptides and enzymes, particularly as biosensors [233]. In 2008 and 2009, DNA-bio components utilising graphene

derivatives was demonstrated. Single-strand DNA (ssDNA) can strongly interface onto both sides of graphene and particularly wrinkled surfaces of chemically modified graphene through a self-assembly process by π–π stacking [234, 235].

As mentioned, the unique abilities of GO (the large planar surface and multifunctional groups), makes it an ideal nanomaterial in biotechnology [216], and a novel candidate to be utilised in biomedical investigations such as in vivo targeting, drug delivery purposes, and cell imaging [236] (Figure 1-4).

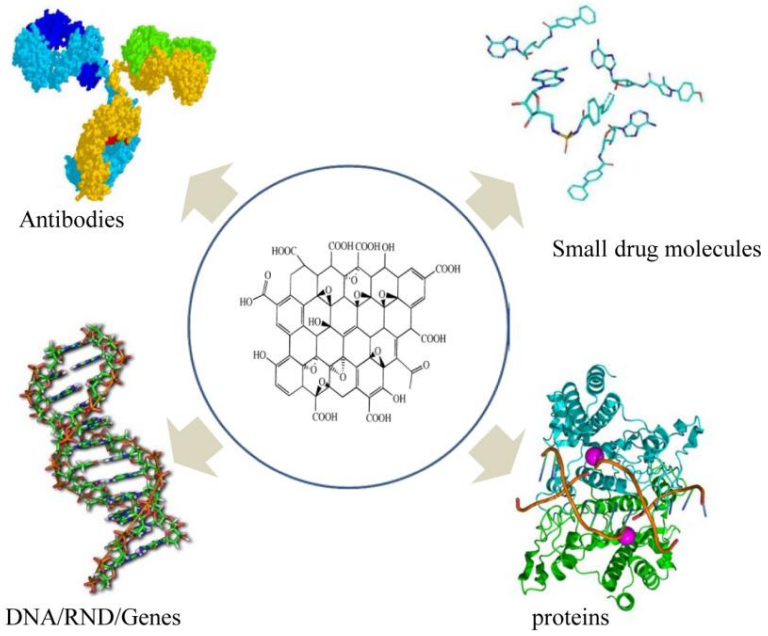

Figure 1-4. GO can be a carrier for various therapeutic conjugates in drug delivery systems [216].

1.5.2 GO, a Potential Carrier in Cancer Therapy

Over the past decade, GO has been also widely applied as a valuable drug nanocarrier for various compounds, including anti-cancer drugs and imaging compounds [231, 237, 238].

Application of GO in targeting DDSs was first demonstrated by Sun et al. who demonstrated doxorubicin conjugated GO for *in vitro* selective drug delivery [239]. Then, it was shown that GO can also be used for loading (via π- π stacking) and delivery of two anti-cancer drugs [240]. Zhang et al. modified GO with sulfonic acid groups rendering it stable in physiological solution. This modification was followed by

using FA to specifically target tumour cells overexpressing FR (Figure 1-5). Doxorubicin (DOX) and camptothecin (CPT) were two chemotherapeutic drugs that were loaded onto the folate-conjugated GO sheets, which showed promising results compared to non-targeted GO-DOX/CPT [241].

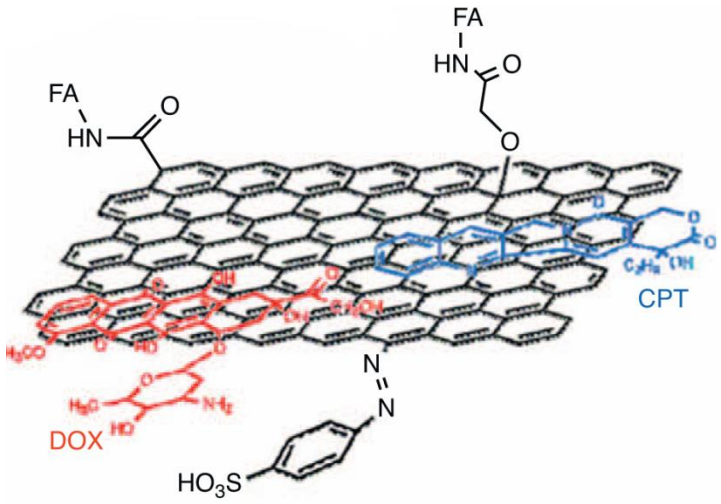

Figure 1-5. Modified GO with sulfonic acid and FA.

Schematic image showing the loading of doxorubicin (DOX) and camptothecin (CPT) onto FA-modified GO which is functionalized with sulfonic acid groups increasing its stability in physiological solution [216].

Moreover, modifying GO with PEG (denoted GO-PEG) enabled higher solubility and stability in biological solutions, resulting in higher cellular uptake and therapeutic efficacy in cancer studies [240, 242, 243]. In 2010, Liu et al. examined *in vivo* tumour uptake of PEGylated GO in mouse model tumours for the first time. Their results showed high tumour uptake of the PEG-modified GO due to efficient tumour passive targeting of GO caused by EPR effect. GO-PEG also reduced RES recognition and remarkably increased tumour targeting in *in vivo* studies [242].

In this study, we used GO-polymer as an appropriate carrier to develop a selectively cytotoxic therapeutic system utilising over-expressed receptor blockage. The introduced GO sheet modified with PEG and suitable targeting ligands can form an impermeable shield around the targeted tumour cells to block endocytosis, resulting from metabolic deprivation (Figure 1-6).

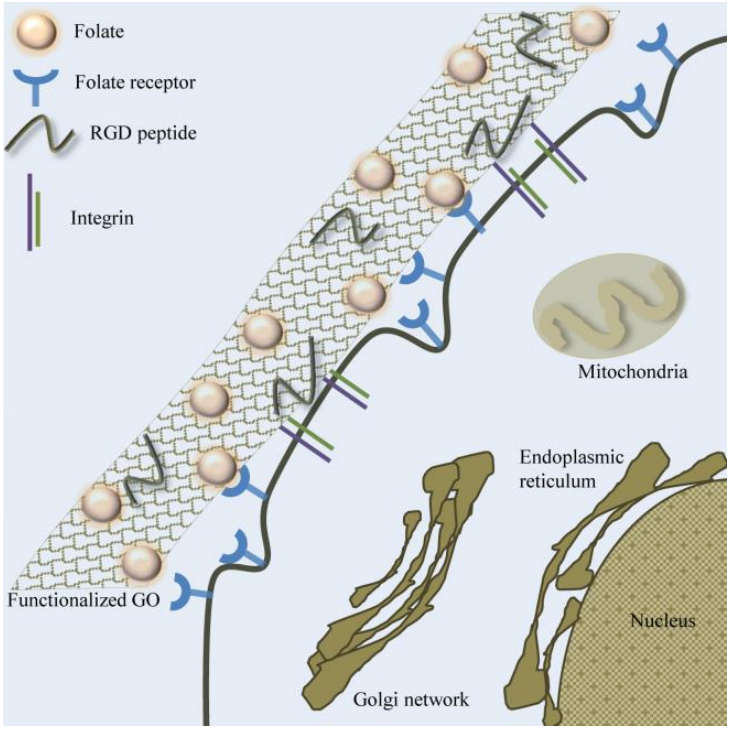

Figure 1-6. Modified GO network for over-expressed receptor blockage.

The GO network binds to the number of receptors (FR and integrins) from a number of rafts to inactivate endocytosis.

1.6 Scope of the Thesis

This thesis focuses on the evaluation and determination of strategies to synthesise engineered polymeric GO networks able to block over-expressed receptors on tumour cells for treatment purposes in a selectively toxic way.

Over-expressed receptors in targeting cancer therapy have been thoroughly studied over past decades to increase the efficiency of cancer treatments and reduce unwanted side effects. This has led to some receptors being considered as potential candidates for targeting drug delivery, particularly cancer targeting therapy. The work presented in this thesis studied the efficiency of two common targeting receptors (FR and integrin) for advanced cancer therapy to decrease cytotoxic and other adverse effects on non-tumour cells.

Overview of chapters 2 to 6:

- Chapter 2 explains the various techniques and methods used in this thesis.
- Chapter 3 describes the separation and fractionation of the GO sheets and its macromolecular functionalisation. This modification is based on the covalent attachment of PEG-amine on the GO surface via amide bonds to form GO-PEG.
- Chapter 4 describes the fluorescence properties of the modified GO sheets. The effect of various factors on the observed fluorescence emission is also discussed.
- Chapter 5 discusses the potential of ligand-modified GO sheets (GO-PEGFA and GO-PEGRGD) for cancer therapy. The cytotoxicity effects of single ligand (FA or RGD) or dual ligand (FARGD) modified GO are discussed. The interaction of modified GO sheets with selected tumour cells is also studied. Synergistic/additive effects of the GO networks with methotrexate (MTX) and doxorubicin (DOX) are also examined.
- Chapter 6 concludes the thesis findings and discusses the possible future aspects of the proposed therapeutic system.

Chapter 2

Instrumentation

2 Instrumentation

2.1 Introduction

This chapter describes the techniques employed throughout this thesis to produce and investigate the experimental data. The techniques including spectroscopy and microscopy were fundamental in chemical and biological studies. The details of each technique along with its theory and applications are discussed.

2.2 Spectroscopy Techniques

Spectroscopy, in general, is the study of the interaction of light with a material [244]. Depending on the wavelengths of light employed, different types of spectroscopy are possible, including ultraviolet–visible spectroscopy [245] (ultraviolet and visible ranges of light), fluorescence spectroscopy [246] (particular emission and excitation wavelengths in the UV and visible range), infrared spectroscopy [247] (infrared light) and nuclear magnetic resonance spectroscopy [245, 248] (light of radio frequencies).

2.2.1 Ultraviolet–Visible (UV-Vis) Spectroscopy

Ultraviolet–visible spectroscopy is absorption spectrophotometry commonly applied to measure the absorbance of particular chemicals in the UV-Vis spectral region [249]. Functional groups, chemical double and triple bonds, and even π electrons in aromatic structures (chromophores) allow molecules to absorb UV-visible light [250]. Such absorption enables structural and dynamical studies of compounds using UV-Vis spectroscopy.

While light passes through a solution of the sample, a certain amount of that will be absorbed by structural chromophores in the solution. The absorbed radiation is proportional to the sample concentration. This phenomenon is stated by the Beer-Lambert law [250] written as Eq1;

$$A=\varepsilon lc \qquad (1)$$

where A is absorption, ε is the molar absorptivity (L $mol^{-1}cm^{-1}$), l is the path length through the solution (cm), and c is the molar concentration of the solution.

Through the use of Eq1, a UV-Vis spectroscopy is a convenient technique to investigate the chemical and/or physical characteristics of chemicals [250]. However, this method does not precisely identify unknown samples. In this case, the measured absorbance is compared to a reference spectrum as a standard to identify the substrate [250].

In this study, a Varian Cary 3E UV-Vis spectrophotometer was used to determine the chemical structure of graphene oxide (GO) and its modified derivatives. UV-Vis spectroscopy was also used to determine the concentration of modified GO samples using a standard curve. The absorbance of GO over the range of 200 nm to 600 nm peaked at 230 nm and 250 nm, while the modified GO showed different absorption spectra. Specific details of each experiment and set-up are described in chapters 4 and 5.

2.2.2 Fluorescence Spectroscopy

Fluorescence is the emission of light at a higher level of energy by a substrate as a result of absorbing light at a different wavelength of a lower level of energy [246]. The presence of a fluorophore, an atomic group with an excited molecule that emits photons giving rise to fluorescence, makes some compounds fluorescent [251]. This property is measurable with a fluorescence spectrophotometer to study photoluminescent characteristics of macromolecules [252]. Through excitation, an electron in the fluorophore will be excited from the ground state to a higher energy level. The excited electron returns to a lower state due to vibrational reduction which produces heat. This electron then returns to the basic state giving rise to a fluorescence emission [251, 253]. This emission can also be measured with a fluorescence spectrophotometer to study the photoluminescence of macromolecules [252].

In this study a Varian Cary Eclipse fluorescence spectrophotometer was used to study the fluorescence properties of GO and its modified derivatives. This instrument was set to scan mode for data collection of the excitation or emission (*Ex/Em*) spectra over the range of *Ex/Em* wavelengths. Scan mode permits the desired wavelength to be set at any particular value. Details of the experimental conditions are described in chapters 3 and 4.

2.2.3 Fourier Transform Infrared (FTIR) Spectroscopy

Fourier transform infrared spectroscopy is one of the primary analytical methods to study molecular structures, particularly in polymer science [254]. FTIR is mostly available for any kind of sample, including solutions, powders and even gases [255, 256]. Infrared (IR) radiation energy is lower than visible and ultraviolet radiations. Absorption of IR radiation produces a small energy variance between the rotational and vibrational states for each individual molecule [254]. IR spectroscopy is one the fastest and most sensitive techniques to determine the molecular structure of a sample based on the relationship between the structural molecules and detected IR spectra. Each observed absorbance peak corresponds to one specific functional group or chemical bond within a molecule [254].

In this study a Varian 7000 FTIR Spectrophotometer was used to determine whether chemical reactions of GO went to completion through the modification process. This instrument was set to scan mode for data collection of the IR absorbance spectrum over the range of 4000-400 cm^{-1}. For each spectrum, 32 scans were obtained.

2.2.4 Nuclear Magnetic Resonance (NMR) Spectroscopy

Similar to other types of spectroscopy, NMR also uses light to make a transition between molecular energy levels [248]. This technique uses the NMR of the nuclei of specific atoms to determine their chemical, physical and even biological characteristics. The most commonly used nuclei in NMR are carbon-13 (^{13}C) and hydrogen-1 (^{1}H) [257]. NMR spectroscopy is one of the most important techniques used in chemical studies to investigate the chemical structure and dynamics of molecules [258, 259].

In this study a Varian NMR300 was used to determine the structural foundation of the prepared PEGylated molecules. The instrument was set at resonance frequencies of 75 MHz for ^{13}C and 300 MHz for ^{1}H. ^{13}C NMR spectra were observed under cross-polarisation and magic angle spinning.

2.3 Microscopy Techniques

Microscopy describes the operation of a microscope providing a magnified image of a specimen [260]. Apart from objective classification, there are different types of microscopes based on their application, e.g. bright field and fluorescence microscopy, or the source of energy that illuminates the specimen with either photons or electrons, e.g. optical and electron microscopy, respectively.

2.3.1 Optical Microscopy

Optical microscopes utilise light, either visible (e.g. bright field microscopy) or ultraviolet (e.g. fluorescence and confocal laser scanning microscopy), to magnify the examined samples [261]. Schematics of typical fluorescence and confocal microscopes are shown in Figure 2-1.

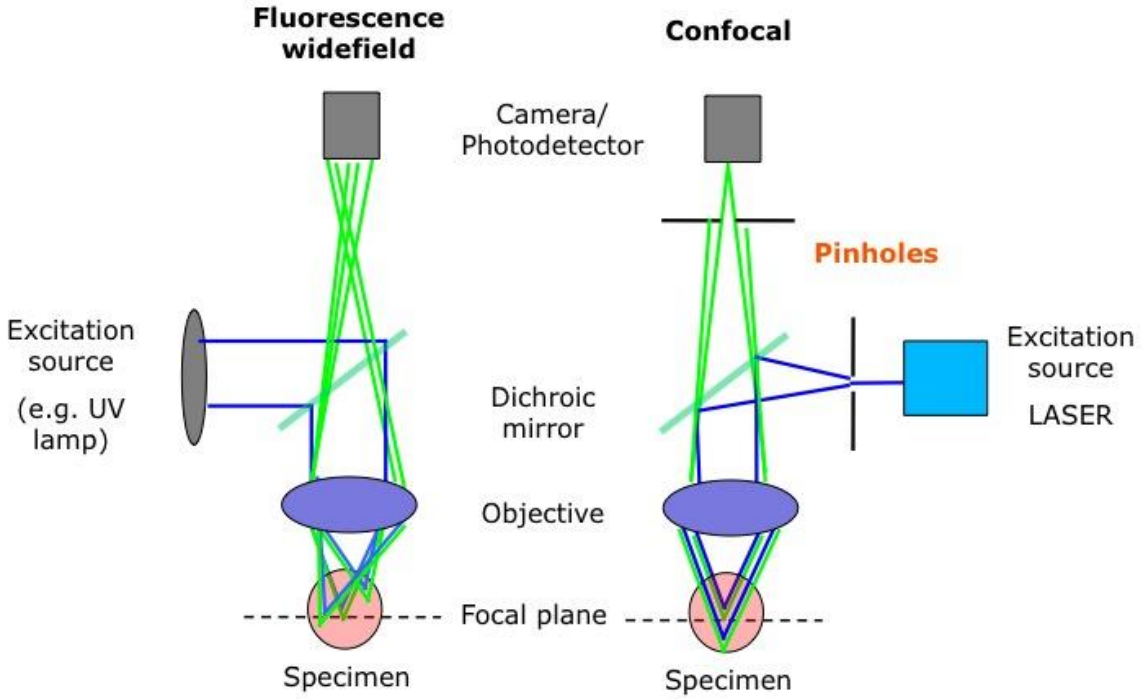

Figure 2-1. Schematic diagrams of fluorescence and confocal optical microscopes [262].

The use of a pinhole is the main difference between these two microscopes and allows the confocal microscope to focus on a single plane (so called Z stack) as discussed later.

2.3.1.1 Fluorescence Microscopy

Fluorescence microscopy is an important technique in biomedical studies to observe living biological specimens or chemical samples [263, 264]. This technique is particularly valuable to detect the subcellular location of fluorescently labelled special proteins and other cellular components as they travel through a cell [264].

In this study a Leica STP6000 fluorescence microscope was used to study the auto-photoluminescence of GO and its functionalised derivatives, particularly in cell media. Details are discussed in the chapters 3 and 4.

2.3.1.2 Confocal Laser Scanning Microscopy (CLSM)

Confocal microscopy is another type of optical microscopy that increases the resolution and contrast of the magnified bio-images by applying a special pinhole [265] (Figure 2-1). The pinhole excludes all out-of-focus light to generate only one single spot of focused light [266]. This technique is used to study samples in depth by taking a series of slices (known as Z-stacks) through the varying focus levels, which generates either 2D or 3D images [266, 267]. Confocal microscopy is also valuable in the life and material sciences to study molecular structures, interactions and behaviours [268]. In this study, a TCS SP5 from Leica Microsystems was used for live cell imaging and taking Z-stacks of associated GO sheets with treated tumour cells in *in-vitro* experiments.

2.3.2 Electron Microscopy

Electron microscopes are the most complex and innovative instruments in modern science. They utilise a beam of electrons as an alternative to light and an electromagnetic field as a replacement for glass lenses to magnify the specimen [269]. These microscopes have much higher magnifications than optical microscopes, which are limited by the wavelength of light, and so are suitable for studying much smaller entities [270]. Based on the type of detected electrons (primary or secondary electrons), electron microscopy is sub-divided into two main classes: transmission electron microscopy (TEM) and scanning electron microscopy (SEM) [271], with instruments

for each class having a different setup (Figure 2-2). TEM and SEM are described in the following sections.

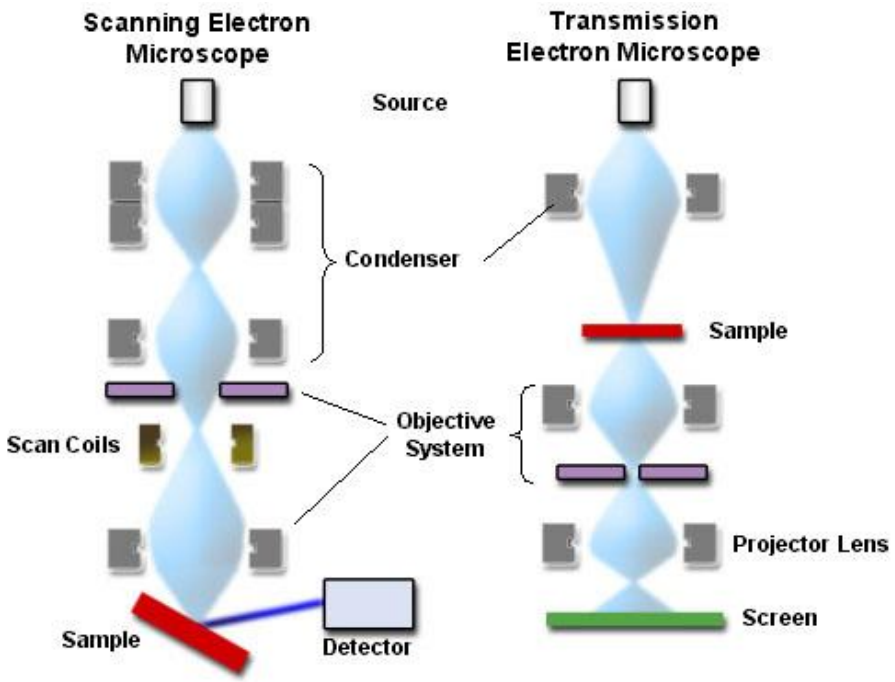

Figure 2-2. Schematic diagrams of SEM and TEM instruments [272].

In comparison with TEM, SEM has a lower magnification and provides a 3D image of the surface morphology.

2.3.2.1 Transmission Electron Microscopy (TEM)

TEM is the original form of electron microscopy in which the primary electron beams were emitted by a cathode in a magnetic field, and transmitted through tiny slices of the sample. The sample is pre-stained with palladium or gold and placed onto a specific TEM grid [270]. Acceleration of electrons under vacuum consequently produces higher energy, which enhances the resolution of TEM images [269](down to 0.2 nm, which is smaller than many atoms). Therefore, TEM is a good technique to investigate the structural arrangement of atoms in a sample.

In this work, GO sheets and derivatives were dried onto coated TEM grids and viewed in an FEI Tecnai Spirit transmission electron microscope at 120 kV to study

their physical structures. Images were captured with a Gatan Eagle digital camera at a resolution of 2048 × 2048 pixels.

2.3.2.2 Scanning Electron Microscopy (SEM)

SEM detects the secondary electrons emitted by the surface of a sample, which was previously excited by the primary electrons [273, 274]. The interaction of primary electrons with the sample produces signals, including secondary electrons, back-scattered electrons, photons, visible light, and heat [275]. The signals correlated to the secondary electrons are collected by an appropriate detector to map the morphological surface of the examined sample. In comparison with TEM, SEM has a lower magnification and provides a 3D image of the surface morphology [270].

In this study GO samples were coated with gold using a Xenosput sputter coater (Dynavac) and imaged with a Philips XL30 field-emission SEM at a voltage of 2.0 kV and spot size of 2. The morphological appearance of the modified GO sheets and their cellular interactions were then studied.

2.4 Atomic Force Microscopy (AFM)

AFM, or scanning force microscopy as it is also known, is a type of scanning probe microscopy that utilises electrical flow to construct a very high resolution image of the sample surface [276]. This type of microscope is designed to measure the superficial properties of the sample using a small and sharp probe that scans a small area of the sample.

AFM is a useful technique to study the morphological properties, nanomechanical characterisation, surface roughness [277, 278], and even thermal conductivity of samples [279]. During this project an Asylum Cypher AFM was used in contact mode with a drive frequency of 75-80 kHz, and a typical scan rate of 1.00 Hz. This technique was used to study the morphological and physical features, and thickness of GO and its modified derivatives.

2.5 Thermal Gravimetric Analysis (TGA)

TGA is one of several thermal analysis methods for material characterisation. TGA monitors the mass changes of materials as a function of time (at constant temperature) or temperature (at constant heating rate), while the atmosphere is controlled [280]. By increasing the temperature, many components of a sample are decomposed and the percentage of mass change is measured [281]. In this study TGA was used to determine the physical stability of the GO sheets and its modified derivatives. This technique was also used to investigate the yield of GO functionalisation. The measurements were conducted on a Mettler Toledo TGA/SDTA851e thermogravimetric analyser with a heating ramp of 10°C/min under an oxygen or nitrogen flow of 30 ml/min. Samples were heated up to 800°C.

Chapter 3

Separation and Macromolecular Functionalisation of Graphene Oxide Networks

3 Separation and Macromolecular Functionalisation of Graphene Oxide Networks

3.1. Introduction

Graphene Oxide (GO) is a two dimensional hydrophilic network made of oxygenated graphene [220]. GO nano-sheets accept a wide range of functional groups that allow the surface chemistry to be modified for a number of potential applications in drug delivery and cellular/organ targeting [221-223]. The combination of these properties with the observed auto-fluorescence makes GO sheets attractive for theranostic delivery systems and signalling materials [222, 224, 225]. A major body of related literature has been directed towards exploring the chemical and physical properties of this unique material for optoelectronic and biomedical applications [226-229].

A mixture of sheets with different morphologies, sizes and thicknesses are produced when GO is fabricated by a defined chemical oxidation procedure [282, 283]. The chemical modification of pure graphene (source material of GO) introduces a number of oxygenated functional groups to render the graphene surface hydrophilic [284] and also makes the GO more chemically reactive [285-287]. The GO is then a two dimensional (2D) structure with hydrophilic edges and both hydrophobic and hydrophilic regions on the faces due to the presence of carboxylic acid groups on the edges and hydroxyl and graphene groups on the surface [288].

For a given chemical modification, the proportion of hydrophilic functional groups to hydrophobic regions of the GO structure varies with the sheet size [288, 289]. The effective “amphiphilicity” of the GO sheets and interfacial activity is found to be a function of the sheet size. Smaller GO sheets possess higher so called “edge-to-centre” ratios which result in more stable colloidal dispersions due to higher hydrophilicity [290]. However, the interfacial functional groups in the interstitial spaces between GO layers are less accessible for chemical interactions due to steric inhibition [291]. As a result, graphene oxide single sheets with thicknesses of ~1 nm are more reactive to compounds such as polyethylene glycol (PEG), a FDA-approved vehicle, which functionalises GO into a material that is potentially suitable candidate for clinical applications [292-294].

Different methods have been introduced to fractionate GO single sheets such as sonication for mechanical exfoliation [295], dispersion in organic solvents as a liquid exfoliation, organic solvent or surfactant assisted sonication [296], thermal exfoliation [297], and exfoliation by polymer/dye functionalisation [298]. These methods are based on mechanically separating the sheets by overcoming the van der Waals interactions and inter-sheet π-π stacking to enable solubilisation [299]. Mechanical methods have been shown to have detrimental and varied effects on the sizes of the GO sheets and furthermore on the physical and chemical characteristics of the sheets produced [300, 301]. These effects change the interaction of GO and its functional derivatives in important size-dependent applications, such as the interactions with cells in clinical studies [302, 303].

The strong inter-sheet π-π stacking of GO sheets also decreases the solubility leading to aggregation in solution. Therefore, the proper selection of solvent with suitable repulsive solvation force is required, as many solvents are difficult to remove in the post-processing stage due to their high boiling points (>150 °C) [304]. Association of GO sheets with surfactants, polymers or organic molecules has been used as strategies for the dispersion of GO sheets. These methods rely on induced repulsive electric double layers and/or repulsive steric forces between exfoliated GO sheets to render the sheets soluble [296]. However, removing the associated molecules of surfactants/solvent from GO sheets for biological applications remains problematic.

The first density gradient separation of functionalised GO nano-sheets using sucrose density gradient and an centrifugal (50k rpm) was reported in 2008 [243]. This method was later applied to the separation of pure GO [305]. The gradient density separation method uses a solution containing solvents of different density over a range of compositions to generate the density gradient [306]. The sample solution is placed on the top of the tube and then centrifuged in order to separate the nano-particles by density once the height is equilibrated. The gradient media in this method must be a solvent for the particles to be separated [307]. As a result, the fractionated particles are immersed in a solution in which the gradient molecules are adsorbed to the GO sheets and must be removed prior to further modification using another solvent. This clean-up stage is crucial for GO preparation, as the presence of adsorbed molecules on the separated sheets can render a number of sites inactive for further chemical modification.

In the previously reported separation method however, there has not been a clear strategy of purification to remove the adsorbed solvent from the fractionated GO sheets [308].

Another size separation method was introduced in 2011 by Xiluan Wang et al. based on the pH-dependent amphiphilicity of GO molecule [309]. GO has the capacity to buffer the solution due to the structural acid and base groups rendering the pH adjustment difficult [310]. Recently, a polar solvent-selective sedimentation method has been reported [311]. This technique is challenging due to the narrow size distribution, the use of large volumes of organic solvent, and a long standing fractionation time [310]. More recently, Wang et al. presented an alternative size-fractionation method based on filtration [312]. This technique avoids some of the complexities of the previous methods. However, it is both time consuming and not readily applicable in the nanometer size range.

In the current work, a simple and robust gradient centrifugation method is proposed for the separation and fractionisation of GO single nano-sheets using water-glycerol media (Figure 3-1). This procedure eliminates the use of sonication and ultracentrifugation making the separation more controlled and simple. Furthermore, the adsorbed gradient molecules are more readily removed from the separated fractions using dimethylformamide (DMF). Here we report the chemical, optical, auto-fluorescence and cytotoxic properties of the fractionised GO nano-sheets using the water-glycerol gradient method.

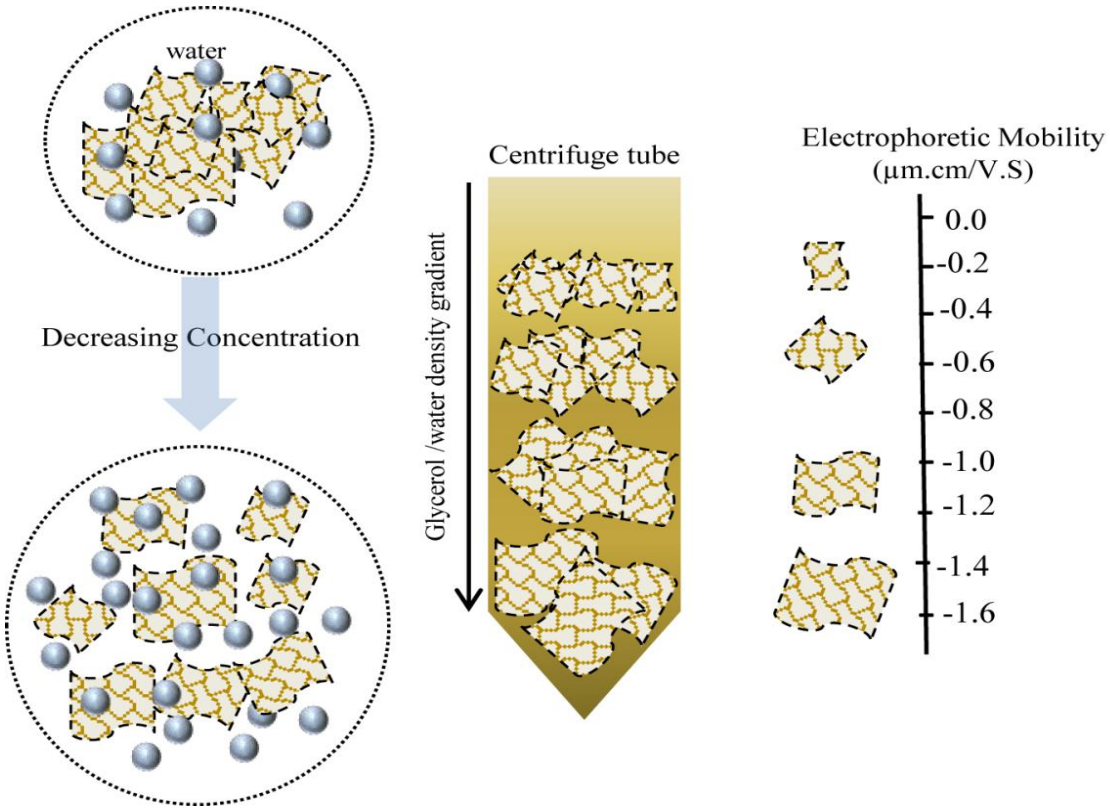

Figure 3-1. Schematic representation of GO fractionation in water-glycerol solutions using gradient centrifugation.

The GO solution contains multiple GO sheets were diluted several times to get the GO sheets entirely exfoliated in water at concentrations below ~10^{-2} mg.ml^{-1}. Water-glycerol mixtures were used to fractionate the GO single sheets in a centrifugation process separating different fractions from smaller to larger sizes of GO sheets. Mobility measurements were then carried out for the fractionated layers to determine the effective surface charge of the GO nano-sheets.

3.2. Materials and methods

3.2.1. Separation procedure

GO (4 $mg.ml^{-1}$) (777676-50 ml) and all other chemical reagents were purchased from Sigma-Aldrich, Australia. Glycerol was mixed with water to obtain the density gradient (5-50%). Each density fraction (2 ml) was transferred to a 50-ml centrifuge tube respectively with the higher density portion (50%) at the bottom and the least dense one (5%) on the top. 500 µl of GO solution (0.01 $mg.ml^{-1}$) was distilled onto the multilayer gradient. The resultant solution was centrifuged for 3 hours at 8,000 g using a Beckman Avanti 30 centrifuge. Each fraction (GOF_1-GOF_4) was removed using a 1000 µl pipette. The GO fractions were then washed with DMF followed by dialysis against distilled water for 72 hours removing glycerol and DMF from the separated sheets. The final solutions were collected and concentrated by a 10 kDa molecular weight cut-off (MWCO) Amicon filter at 5,000 g. This was followed by a dry freezing process to obtain each fraction in a lyophilised powder.

3.2.2. GO Characterisation

Dynamic Light Scattering (DLS) was measured by a Zeta Sizer Nano ZS Malvern, in customised 1 cm Zeta Sizer cuvette at room temperature. Glycerol was chosen as the solvent with a viscosity of 1.261 m^2/s and Refraction Index (RI) of 1.4746 containing GO with RI of 2.44. The average conductivity of the solutions was 0.03 mS/cm. Zeta potential was also determined by the same device for GO with RI of 2.44 in water. Atomic force microscopy (Asylum Research Cypher AFM) was used to determine the size and thickness of GO sheets. A proper size of mica (1 cm^2) was prepared and washed with ethanol and water, then dried under a laminar flow to minimise contamination. The mica surface was pre-coated with the positively charged Polyethyleneimine (PEI) for 30 minutes. After rinsing with distilled water and drying under laminar flow, the product was polished by nitrogen gas before adding 10 µl of each GO fraction. Further, the morphology of the different concentrations of GO sheets was investigated using a transmission electron microscope (TEM), FEI Tecnai Spirit, with an accelerating voltage of 120 kV. The oxidation of the oxygen-containing groups in GO was confirmed by UV-Vis spectroscopy (UV-visible spectrophotometer/Varian 3E) and Fourier transform infrared spectroscopy (Fourier

transform infrared spectroscopy (FTIR) Spectrometer/Varian 7000). Spectra were obtained in an optical range of 500–5000cm^{-1} by averaging 32 scans at a resolution of 2cm^{-1} with one min interval to minimise the effects of dynamic scanning. The optical properties of GO and its derivatives were characterised using a UV-Vis spectrophotometer (UV-visible Varian 3E), a fluorescence spectrophotometer (Fluorescence Varian) at an excitation wavelength of 200 nm and Leica fluorescence microscopy (Leica STP6000).

3.2.3. Cell experiments

MDA-MB-231 and KB cells were cultured at a density of 5×10^4 /ml (13×10^3 cells/cm^2) in 75-cm^2 culture flasks containing 20 ml Dulbecco's Modified Eagle's Medium (DMEM) (supplemented with 10% heat-inactivated fetal calf serum, L-glutamine and antibiotics) at 37ºC in a humidified atmosphere (contains 5% CO_2). Cells were incubated for 24 hours and were then seeded into 96 well plates (10×10^3 cells/cm^2) to form sub-confluent monolayers overnight. Then they were serum-deprived for another 24 hours prior to treatment. Each experimental condition was carried out in triplicate and each treatment was repeated on three separate occasions.

3.2.4. Fluorescence microscopy imaging

Cells were seeded at a density of 5×10^4 /ml (13×10^3 cells/cm^2) in 96 well plates containing 100 µl DMEM media (supplemented with 10% heat-inactivated fetal calf serum, L-glutamine and antibiotics). Plates were incubated at 37 ºC in a humidified atmosphere (contains 5% CO_2) to form sub-confluent monolayers overnight. After serum-deprivation for another 24 hours, cells were incubated with the PEGylated GO sheets (260 µg.ml^{-1}) for 48 hours. Cells were imaged using fluorescence microscopy under bright field and fluorescence mode; L5 red- excitation filter band pass (BP) 564/12- emission filter BP 600/40, A4 blue-excitation filter BP 360/40- emission filter BP 470/40 and N3 green-excitation filter band pass (BP) 480/40- emission filter BP 527/30.

3.2.5. Confocal microscopy imaging

Cells were plated at a density of 3×10^4 /ml at 37 ºC into the "8-well Nunc™ Lab-Tek™ II chambered cover glass slides" (Thermo Fisher Scientific) to form sub-confluent monolayers overnight. After serum-deprivation for 24 hours, cells were incubated with the GO-PEG material overnight and fixed with 3% paraformaldehyde in Phosphate-buffered saline (PBS). Cells were then incubated for 20 min with cell mask deep red to stain cell membrane and then examined using a Leica SP2 Confocal Laser Scanning Microscope.

3.3. Results and discussion

3.3.1. Fractionisation and separation of GO nano-sheets

In aqueous solution the state of aggregation of GO is determined by the concentration [313]. Hydrogenated functional groups present on the GO sheet surface give the GO charge in solution rendering it soluble in aqueous media. In the presence of charge, the water molecules can cover both sides of the GO sheets. The reason for the concentration dependent aggregation of the nano-sheets is not fully understood [314]. The measured sedimentation rates of graphene and GO flakes depend on their thicknesses and 2D sizes [315]. Thin flakes are found to have lower densities than the aggregated stacks of sheets [316]. We found that the GO sheets were entirely exfoliated in water at concentrations below ~10^{-2} mg.ml^{-1} (Figure 3-2). For low concentrations single sheets are the dominant form and the gradient separation is governed by the two dimensional sizes of the dispersed nano-sheets [317].

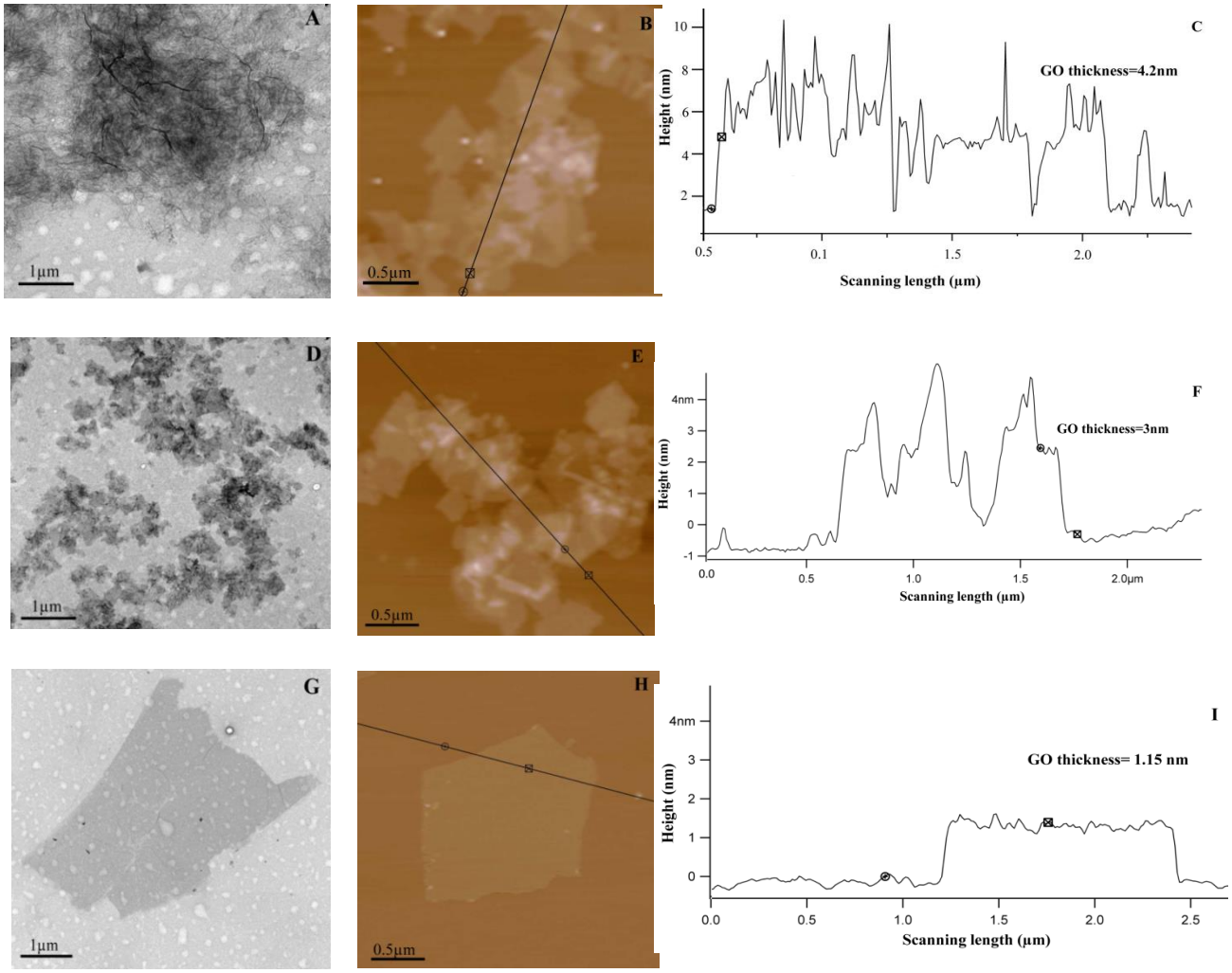

Figure 3-2. GO sheets are entirely exfoliated in water at concentrations below ~10^{-2} mg.ml^{-1}

TEM images (left column), contact mode AFM images (center column) and height profiles along the indicated lines (right column) for GO nano-sheets at concentrations of A-C) 0.1, D-F) 0.01 and G-I) 0.001 mg.ml^{-1}.

In the present study, water-glycerol mixtures (5-50%) were used to fractionate the GO sheets in a centrifugation process using a fixed angle- rotor. Sucrose is a common medium for fractionation with ultracentrifugation, and is generally used for isopycnic mixtures (with uniform sample and density gradient [48]). Glycerol however, is widely used for the separation of components by rate-zonal sedimentation, which is the main focus in this research [49, 50]. Figure 3-3A shows the GO sheets mixed in a water-glycerol media in a centrifuge falcon tube before the separation process. The dark brown layer on top of the tube shows the GO solution (10^{-2} mg.ml^{-1}) to be separated. By using a fixed angle rotor system (Figure 3-3B), a few light brown layers of GO nano-

sheets (diluted solution compares to the primitive sample) migrated to their respective buoyant densities (Figure 3-3C).

Figure 3-3. Separation of GO nano sheets using glycerol density gradient

A) The appearance of the "loaded" centrifuge tube before the separation process, B) The applied fixed angle rotor as a part of the Beckman Avanti centrifuge, and C) the centrifuge tube showing the fractionated layers of GO nano-sheets after glycerol gradient centrifugation for 3 hours at 8,000 × g.

In this figure, GOF_1-GOF_4 represents different fraction zones from smaller to larger sizes of GO nano-sheets. These fractions (GOF_1-GOF_4) were then washed with DMF to remove any adsorbed glycerol molecules attached to the GO sheets via the hydrogenated functional groups. The washed fractions were dialysed against distilled water for 72 hours (water was changed each 12 hours) to remove DMF and glycerol.

To determine the concentration of the separated fractions, a GO standard curve was used (Figure 3-4), for which an equation relating absorbance and the known concentrations of GO standard solutions was derived. The correlation coefficient (R^2) was 0.9878. The unknown concentrations were determined by reference to the absorbance of GO solutions at 230 nm.

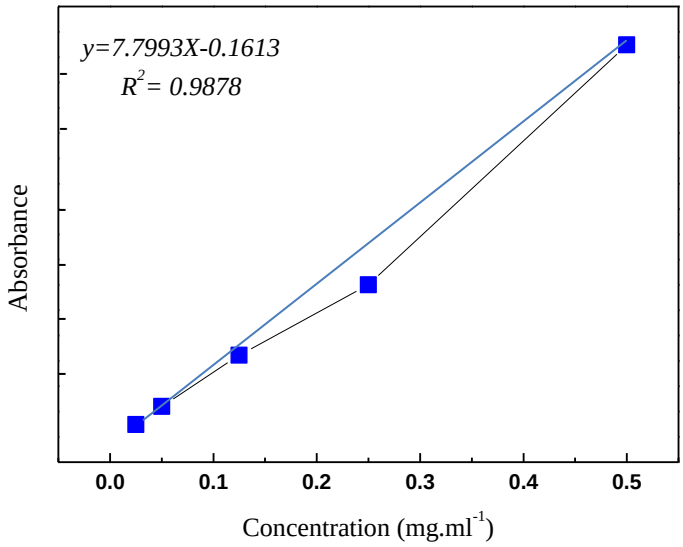

Figure 3-4. Standard curve of GO solutions at 230 nm.

Absorbance versus concentration curve showing a linear relationship between Abs and concentration over the ranged measured.

3.3.2. Size distribution analysis of the fractionated GO sheets

The separated GO sheets were then imaged using AFM. A sample of each fraction was placed on a freshly cleaved mica surface and dried under laminar flow to minimise contamination. The average thickness of the single sheets was measured to be ~1.1 ± 0.2 nm on average (Figure 3-5).

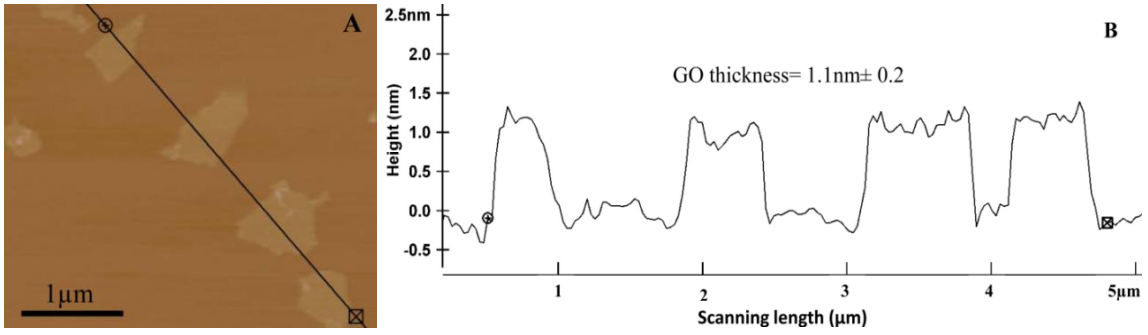

Figure 3-5. AFM image of GO single sheet.

A) Contact mode AFM image of GO single sheets on an atomically flat mica substrate, B) Height profile of the individual GO sheet calculated by AFM device. The Go sheet thickness is found to be 1.1 ± 0.2 nm in accord with previous reports [318].

DLS measures the hydrodynamic diameter of GO sheets in solution. The lateral dimension of the sheets absorbed on mica measured by AFM would be expected to be larger than the hydrodynamic size.

Lotya et al. reported that the hydrodynamic radius in non-spherical particles is often approximated as the radius of a sphere with the same volume as the particle [51]. Other researchers have also measured a correlation between the hydrodynamic DLS radius and measured AFM sizes [52]. Models for interpreting the correlation between actual size and hydrodynamic diameter in irregular and platelet-like particles have been developed [53, 54]. Our experimental results show a linear correlation between the measured hydrodynamic radii measured using DLS and the AFM flat sheet sizes as shown in Figure 3-6 in which the reported hydrodynamic diameter represents the average size of GO sheets [55] in the range of 150 to 850 nm diameter.

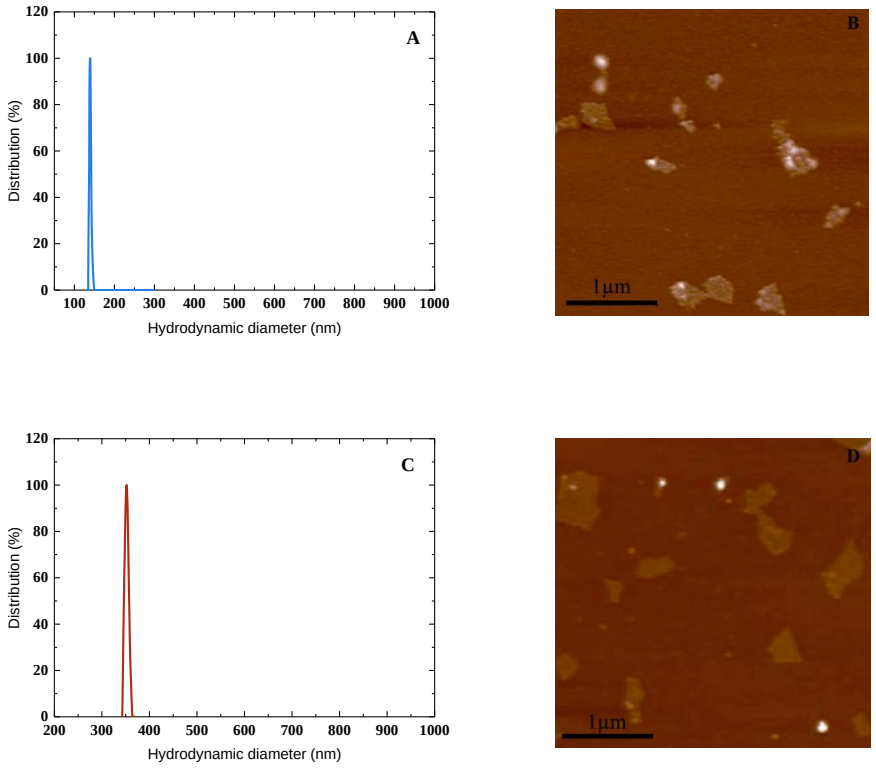

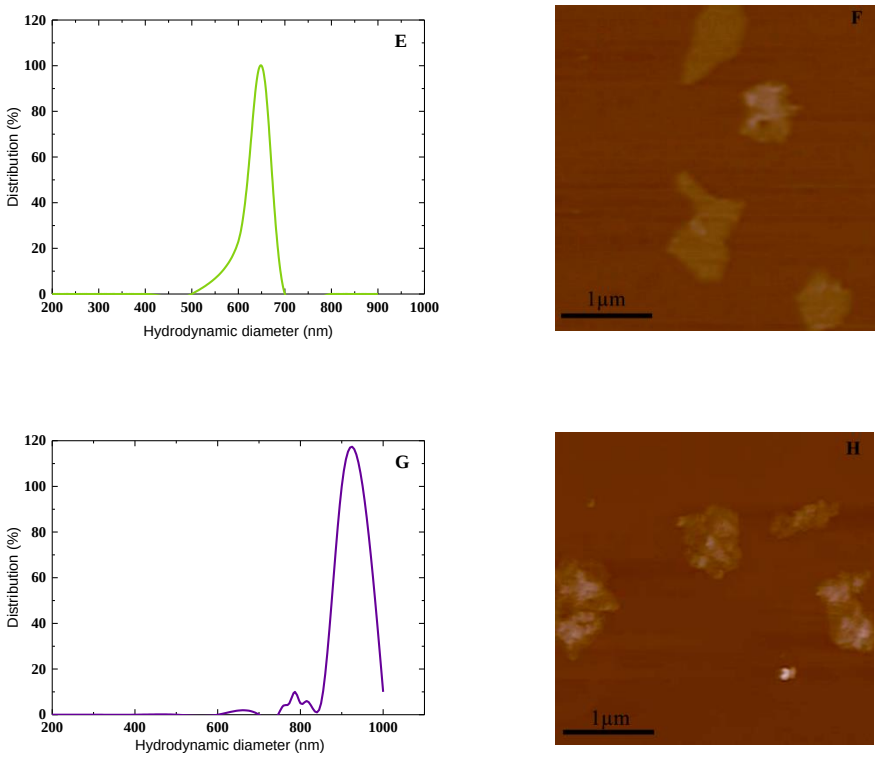

Figure 3-6. DLS measurements and AFM imaging of separated GO sheets.

A, C, E, G) show the hydrodynamic size distribution of the fractionated GO nano-sheets (GOF_1-GOF_4) using DLS (Polydispersity index: 0.33 ± 0.18). B, D, F, H) Contact mode AFM images of GOF_1-GOF_4. A, B) GOF_1-150 nm, C, D) GOF_2-350 nm, E, F) GOF_3-600 nm, and G, H) GOF_4-850 nm. The size obtained from DLS are in agreement with the sizes found using AFM (see text for discussion).

3.3.3. Electrokinetic measurements on GO sheets

The DLS measurements of the hydrodynamic radii were very close to the average radii measured for the flat sheets using AFM. Some orientation of the sheets in the electric field of the mobility measurements was expected depending on the charge distribution. In the experimental conditions used (very small velocities compared to Brownian effects), the drag force on the non-spherical particles can be expressed as an effective hydrodynamic size and the drag calculated using Stokes's law [56]. The electrophoresis measurements were performed in distilled water of pH 6.5 and conductivity of 0.03 mS/cm. We assume that the electrolyte is therefore provided by CO_2 to form bi-carbonate at 0.5×10^{-6} M. The Debye length in solution is therefore 420 nm. Assuming that the discs move in electrophoretic motion as flat discs drawn along

their edges, and therefore for these conditions the dimensionless parameter, ka, is likely far less than one (ka << 1). Henry Theory has been shown to be applicable for species with a curvature radius that is less the thickness (k-1) of the electric double-layer (EDL) [319-321]. The electrokinetic potential, ζ, is calculated from the measured mobility using Eq. 1 which represents the steady state force balance where the electric force equals the hydrodynamic force;

$$U_E = {}^{v}/_{E} = {}^{q}/_{6\pi\eta r} \quad (1)$$

where U_E is the electrophoretic mobility (μmcm/V·sec, V is voltage), q the total charge on the particle, E the electric field, η is the liquid viscosity and r is the effective hydrodynamic radius of the particle.

The GO negative charge arises from COO^- and other functional groups distributed non-homogeneously on the GO surface as well as COO^- groups around the edges [59]. The total charge "q" arises from both edges and charges on the flat surfaces. Quantitatively, our observations show that the electrophoretic mobility of GO sheets is linearly dependent on the radius of sheets. Thus the use of $q \sim \pi r^2$ which fits the measured data indicates that the dominant charge is located on the flat surfaces of the sheets. Substituting into equation one yield:

$$U_E \sim \frac{1}{6} r\eta^{-1} \quad (2)$$

Equation two suggests that the measured mobility should be a linear function of the GO radius. Mobility measurements were carried out for the aqueous solution of the separated fractions (GOF_1-GOF_4) to determine the effective surface charge of the GO nano-sheets (Figure 3-7A). Results show that the negative charge of the GO fractions ranges from -3 mV to -17 mV ,giving rise to the electrophoretic mobilities that range from -0.2 to -1.4 μmcm/V·sec as the size of GO sheets increases. Figure 3-7A also compares the separated GO fractions (GOF_1-GOF_4) with functionalised GO sheets using carboxylic acid and PEG. GO surface charge is decreased to -36 mV after GO carboxylation (GO-COOH) due to the new superficial carboxylic groups. The surface charge of GO PEGylated sheets (GO-PEG) however, increased to 11 mV as PEG molecules are attached to the exposed negative carboxylic

groups. Figure 3-7B shows that the electrophoretic mobility is linearly proportional to the GO radius.

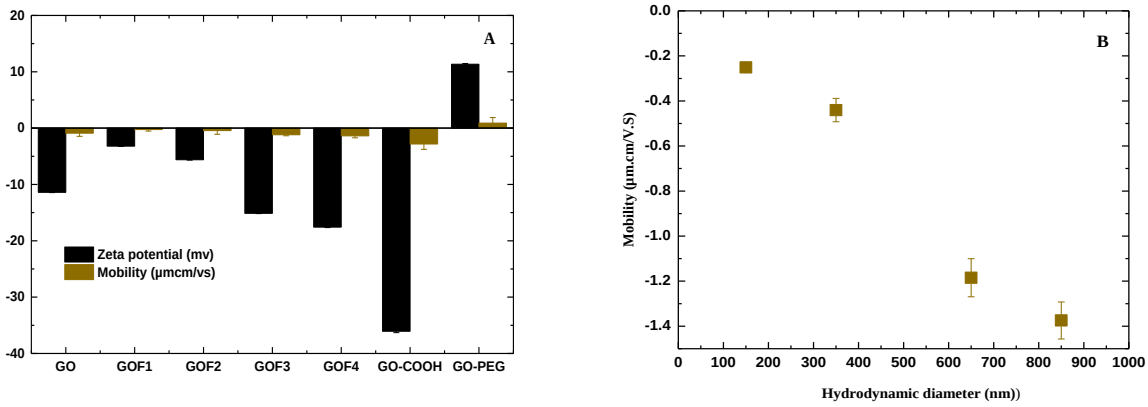

Figure 3-7. Electro-mobility measurements of separated GO sheets

A) Zeta potential and electrical mobility of as-separated GO fractions (GOF_1-GOF_4) compared to GO, GO PEGylated sheets (GO-PEG) and GO carboxylated sheets (GO-COOH) as two common functionalized GO derivatives. B) The electrophoretic mobility of GO fractions (GOF_1-GOF_4) which are linearly proportional to the GO dimensional sizes (see section 3.1.3 for detailed discussion).

3.1.4 Modification of GO

3.1.4.1 Carboxylation of GO

To modify the GO sheets with PEG, plentiful carboxylic acid groups are first required to be present on the GO so as to make a proper attachment (i.e. an amide bond) between the polymer and PEG-amine. In addition to the carboxylic acids decorating the edges of the GO nano-sheets, the platelets contain chemically reactive epoxy groups on their basal planes. These epoxy groups can be easily modified to COOH groups through ring-opening reactions under various conditions (Figure 3-8).

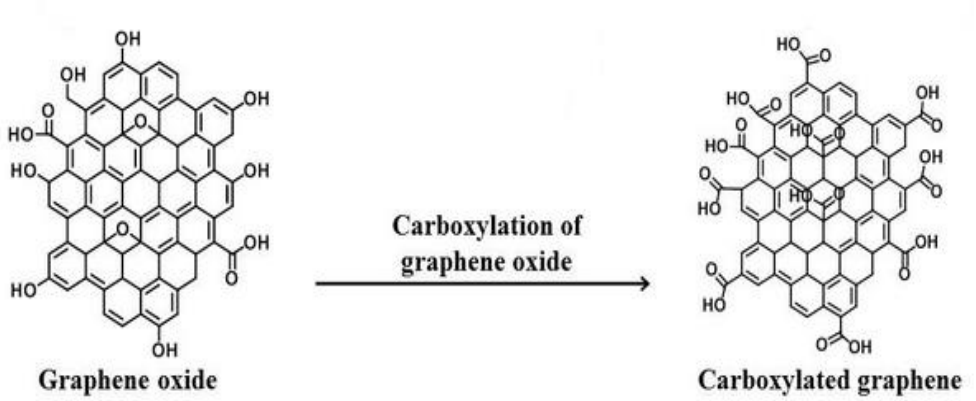

Figure 3-8. GO activation.

The OH and epoxy groups present on GO is converted to COOH groups via conjugation of acetic acid moieties. This reaction is done in strong basic condition (see text).

For GO carboxylation, chloroacetic acid was used under strong basic conditions (1M NaOH). The GO solution was sonicated for 1-3 h to convert the OH and epoxy groups present to COOH groups via conjugation of acetic acid moieties. The resulting GO-COOH solution was then neutralised and purified by repeated rinsing.

The UV-Vis absorption spectrum of GO shows a peak at approximately 230 nm due to the π–π^* of the C = C plasmon, and a shoulder around 298 nm that is often attributed to n–π^* transitions of carbonyl groups (Figure 3-9) [322, 323]. Activation of GO led to a shift to 250 nm and a reduction in UV-Vis absorbance. This decrease was due to the reduction of free electrons in carbonyl, hydroxyl and epoxide groups, which are now involved in converted carboxylic bonds.

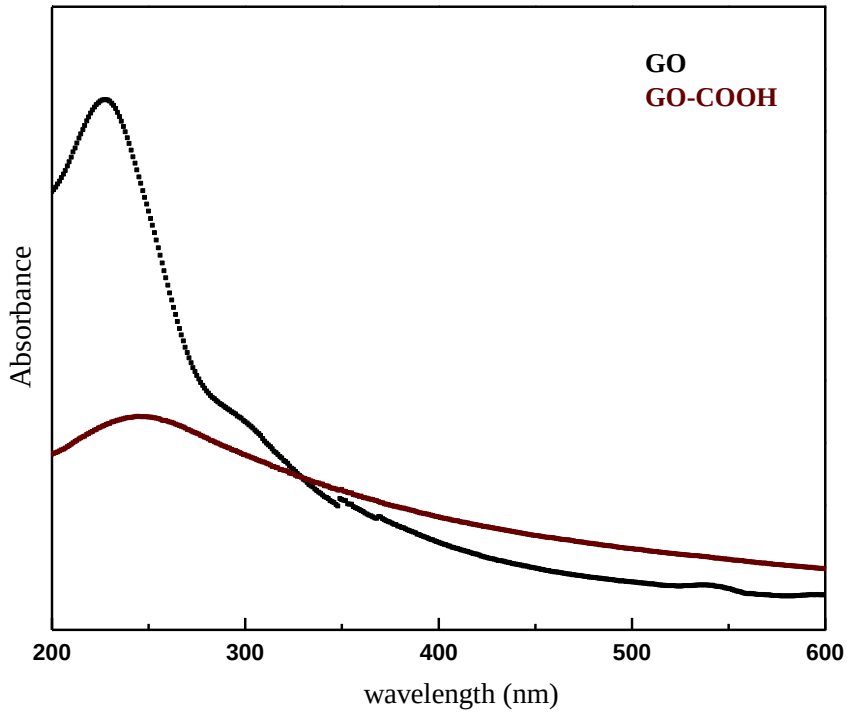

Figure 3-9. UV-Vis absorbance spectra of GO and GO-COOH.

Activation of GO lead to a shift to 250 nm and a reduction in the absorbance due to the reduction of free electrons in the functional groups, which are now involved in converted carboxylic bonds (see section 3.1.4).

Typical FTIR spectra of GO and GO-COOH are shown in Figure 3-10. GO had a broad peak over the range of 2200-3600 cm^{-1}, which corresponded to O–H stretching, and a peak at 1610 cm^{-1} that was attributed to skeletal vibrations due to planar aromatic C=C bonds and absorbed H_2O [324, 325]. Although the same peaks were found in the GO-COOH spectrum, a new peak at 1395-1440 cm^{-1} indicated the combination of C-O stretching, O-H deformation, and C=O stretching, while a second new peak at 480-680 cm^{-1} corresponded to C-O out of plane deformation. As a result of carboxylation, the carboxylic acid C=O stretching at 1690-1760 cm^{-1} had predictably increased [326]. Moreover, the two small peaks at 2925 and 2855 cm^{-1} were assigned to methylene stretching and represented the existence of CH_2 or CH groups in the GO-COOH structure [327]. Based on the identified peaks and relevant increase in intensity that the GO sheets were heavily carboxylated while the fraction of other oxygen functional groups was greatly reduced. Therefore, GO-COOH was successfully prepared.

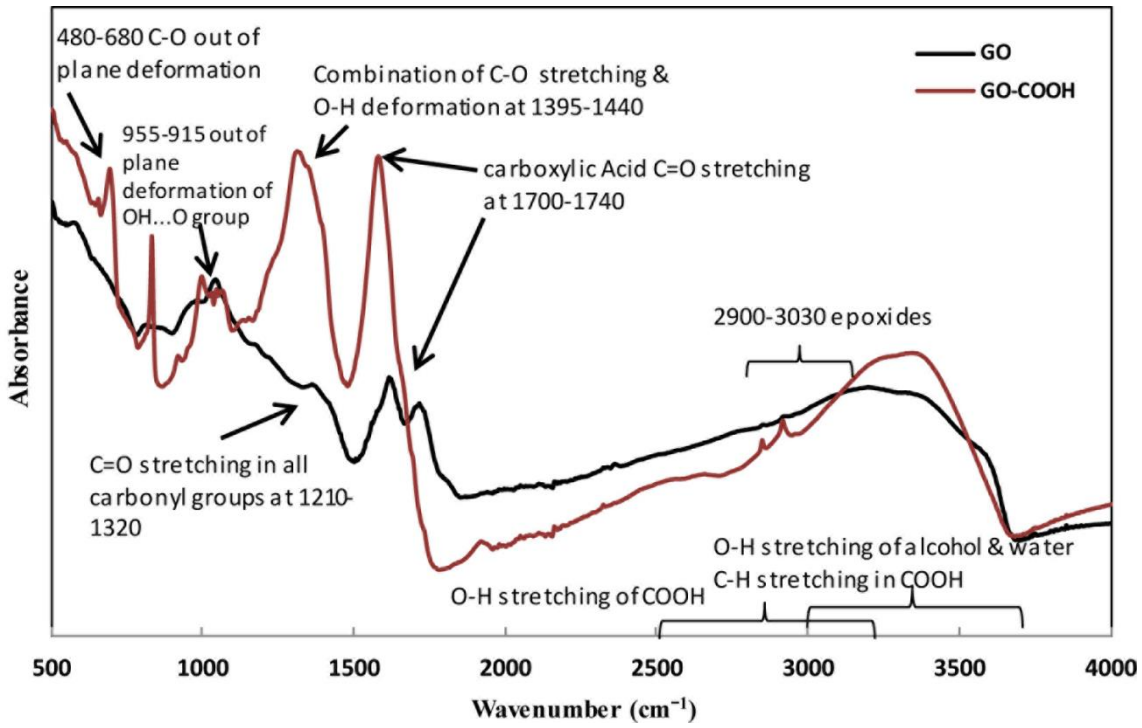

Figure 3-10. FTIR spectra of GO and GO-COOH. The IR absorption bands are labelled.

Thermogravimetric analysis (TGA) was applied to investigate the difference in physical stability of GO and GO-COOH at elevated temperatures (Figure 3-11). This data was based on the degradation of superficial oxygen functional groups (e.g. hydroxide, epoxide and carboxyl).

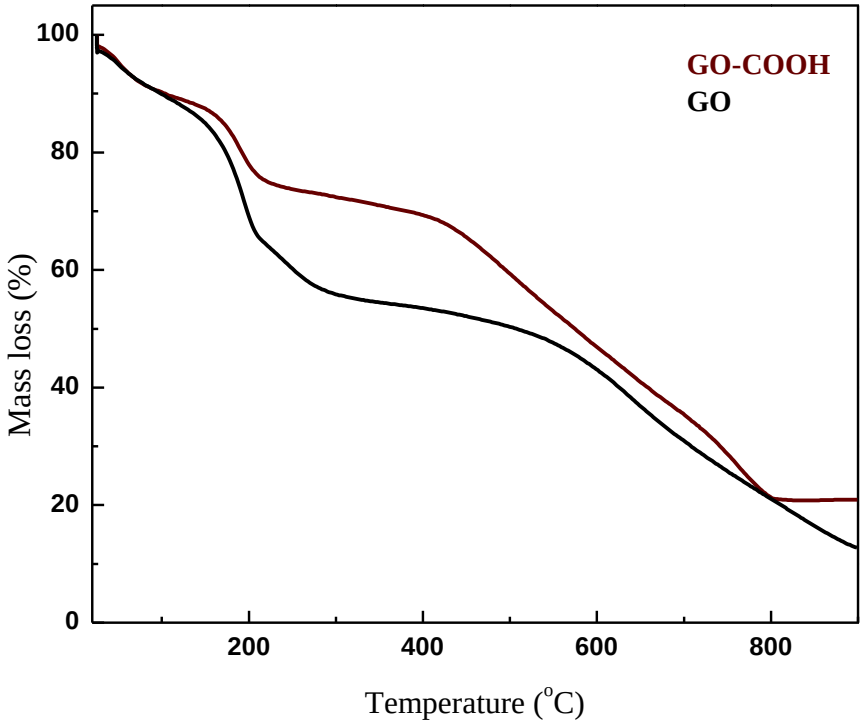

Figure 3-11. TGA curves of GO and GO-COOH networks showing that the GO begins to decompose at 200 ºC.

The residual 20% mass of GO-COOH is thermally stable compared to GO which is completely decomposed at 800 °C.

From the TGA results in figure 3-11, the initial approximately 10% mass loss from both GO and GO-COOH to 120 ºC could be due to evaporation of water molecules trapped between sample layers [328]. Nearing 200 ºC, GO-COOH lost a further 10% mass, whereas GO had around a 20% reduction. From 210 ºC to around 400 ºC GO-COOH was relatively stable, which contrasted with GO that slowly lost another 20% mass. The stability of GO-COOH followed by significant decomposition over the range of 420 ºC to 800 ºC was due to the loss of 'oxygen functional' species [329]. At 800 °C, GO was completely decomposed, while the residual 20% mass of GO-COOH was thermally stable.

3.1.4.2 PEGylation of GO

To prepare GO-PEG, a solution of PEG-amine was added to the GO-COOH polymer suspension and mixed with 3-(ethyliminomethyleneamino)-*N*,*N*-dimethylpropan-1-amine for 2 h. The mixture was then sonicated and allowed to react

overnight. The final product, GO-PEG, was dialysed against distilled water for 72 h to stop the reaction and remove all unreacted molecules. A likely mechanism for this reaction involves nucleophilic attack by the amine group on the α-carbon of GO. UV-Vis spectra of GO and GO-PEG is shown in Figure 3-12. The absorbance spectrum of GO was discussed in section 3.4.1. By contrast, GO-PEG features a broad new peak at around 280 nm indicating the successful amidation process. A small shift also occurred from 230 nm in the GO to 210 nm in the PEGylated GO.

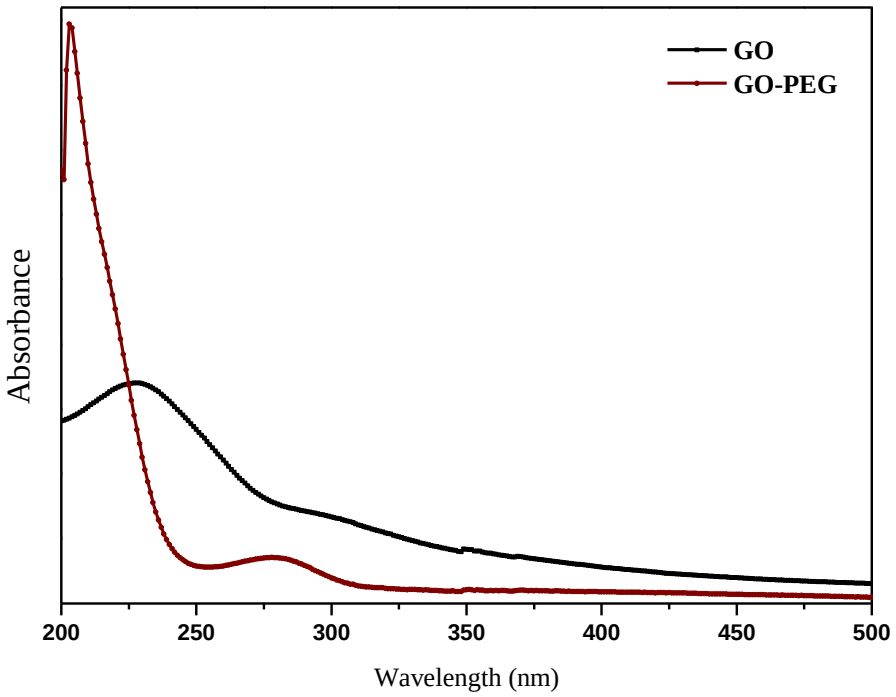

Figure 3-12. UV-Vis absorbance spectra of GO and GO-PEG.

GO-PEG features a broad new peak at around 280 nm indicating the successful amidation process [243]. See text for discussion.

As seen in Figure 3-12, GO-PEG had a higher UV-Vis absorption than GO, despite the polymers having the same concentration of 0.5 $mg.ml^{-1}$. The increased absorbance may be credited to opening of the epoxide group rings and hydrolysis of esters on GO under the basic conditions used during PEGylation [243]. The presence of functional groups in the GO-PEG nano-sheets was further investigated by FTIR spectrophotometry (Figure 3-13). The IR spectrum of GO was previously discussed in section 3.4.1.

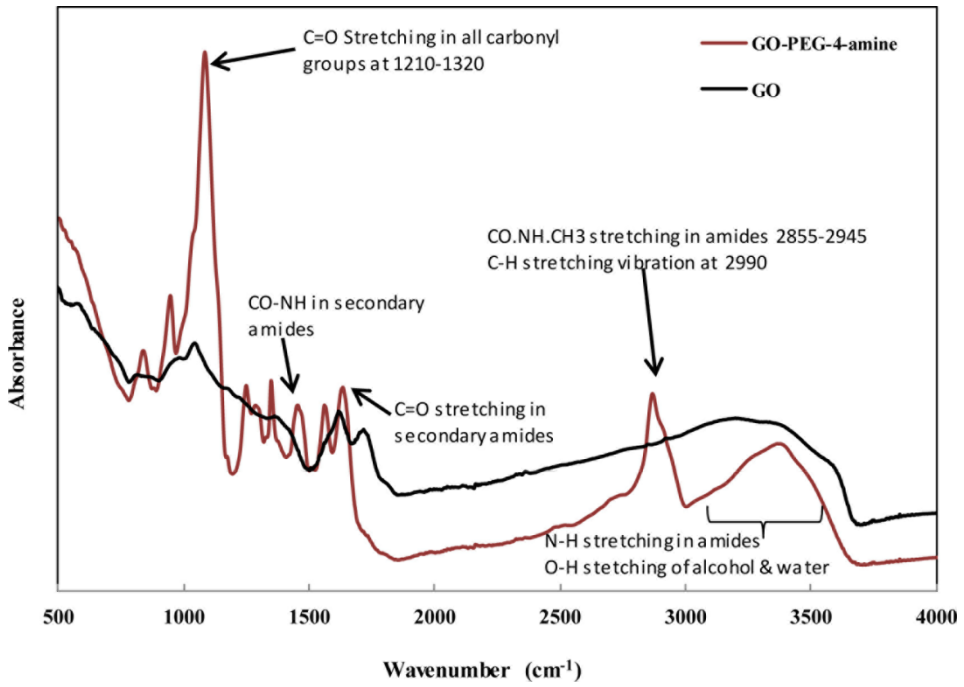

Figure 3-13. FTIR spectra of GO and GO-PEG. The IR absorption bands are labelled.

The spectra for the PEG shows the peaks at 2990 cm^{-1} corresponded to the C-H stretching vibration.

The IR spectrum of GO-PEG supported the existence of an amide bond in the polymer by the C-H stretching vibration at 2990 cm^{-1} that was due to PEG molecules. The strong C=O peaks of carbonyl groups at 1210-1320 cm^{-1}, the characteristic C=O stretching vibration around 1640 cm^{-1}, and the $CO.NH.CH_3$ stretching at 2855-2945 cm^{-1} are all representative of amide bonds between GO-COOH and PEG [330].

3.1.5 Optical properties of the fractionated GO sheets

GO is a two dimensional network of benzene rings which consists of a large number of π- electrons [290, 331]. These localised sp^2 clusters within an sp^3 matrix can lead to an internment of π- electrons in the structure of GO giving rise to fluorescent properties [332]. Smaller sp^2 clusters in GO molecules possess larger gaps and, therefore, have fluorescence properties in the ultraviolet–visible region. In contrast, auto-fluorescence in the near infrared (NIR) is displayed with the larger sp^2 clusters which hold a smaller energy gaps [285]. The photoluminescence of GO and its application in photodynamic therapy has been reported [62, 63]. The quenching effect of GO on absorbed fluorescent molecules, such as dyes has also been studied [64-67].

To the best of our knowledge, the auto-photoluminescence of individual GO sheets has not been previously reported nor has the ability of the derivatised GO to emit in three main fluorescence regions (blue, green and red) been shown. In addition, we used this unique spectral property as one of the applied methods to confirm the effectiveness of the separation and purification steps of individual layers. The authors have shown that GO sheets typically have several fluorescence emissions (350-750 nm) peaking at 480 nm, 540 nm, and exhibiting a broad peak at 580 to 640 nm, depending on the applied excitation wavelength over the range of 200-650 nm [333]. The typical patterns of the emission for each particular excitation wavelength can be used to confirm the effectiveness of the separation, and determine the efficiency of the glycerol clean-up step (using DMF) [334]. The typical emission spectra of the separated fractions (GOF_1 to GOF_4) at an excitation wavelength of 200 nm is exhibited in Figure 3-14. The microscopic fluorescence images inside the graph, exhibit the "auto-fluorescence" of the GO sheets in three different sets of *Ex/Em* conditions (as described above).

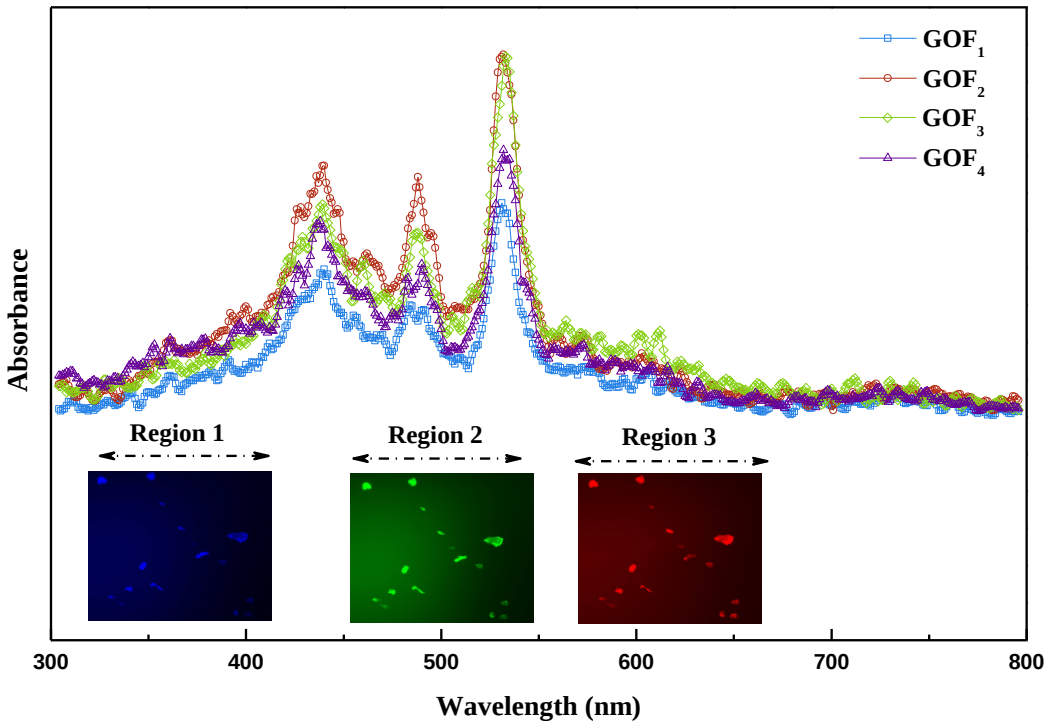

Figure 3-14. The emission spectra of the separated GO sheets (GOF1-GOF4) at 200 nm.

The wide emission spectrum of the fractionated GO nano-sheets (GOF_1-GOF_4) excited at a wavelength of 200 nm. The depictions inside the graph exhibit "auto-fluorescence" of the GO sheets in three main emission filters based on the normal fluorescence microscopy (Scale bar: 200 µm).

3.1.5.1 Fluorescence property of functionalised GO sheets in cell media

The efficiency and brightness of fluorescence of GO-PEG was examined using two different tumour cell lines; KB (cervix carcinoma cell line) and MDA-MB-231 (breast cancer cell line). When cells are exposed to GO-PEG (260 µg.ml^{-1}) for 48 hours, they were visualised under two different sets of *Ex/Em* conditions (Figure 3-15).

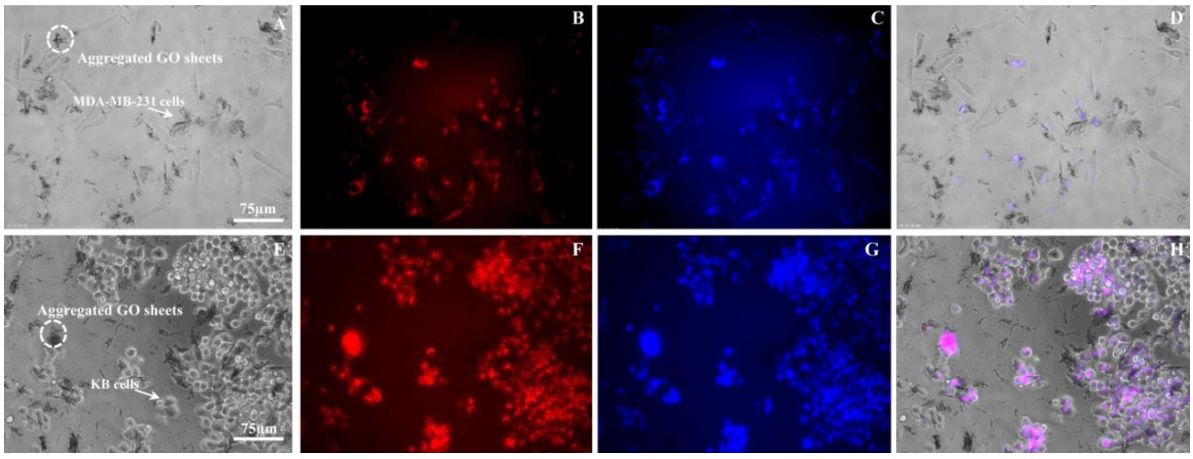

Figure 3-15. Fluorescence microscopy images of incubated tumor cells with PEGylated GO.

A-D) MDA-MB-231 and E-H) KB cells were incubated with GO PEGylated sheets (260 µg.ml^{-1}) for 48 hours and imaged using fluorescence microscopy. Cells were imaged under bright field (A, E) and fluorescence mode (B,C, F,G). B,F: Filter cube L5 red, excitation filter band pass (BP) 564/12, emission filter BP 600/40. C,G: Filter cube A4 blue, excitation filter BP 360/40, emission filter BP 470/40 - D and H represents a merge of two different channels. Arrows indicate cells and circles show non-fluoresce aggregated GO sheets.

Using a fluorescence microscope equipped with an N3 filter cube (green), emission in the green region was only observed for GO-PEG sheets associated with the cell surface (Figure 3-16); internalised sheets did not fluoresce (using higher magnification images can show this in detail). This difference in fluorescence might be due to the effect of membrane association or the particular pH in the local area (outside versus inside the cell). It seems that the observed auto-fluorescence in the intracellular compartment was quenched. The factors that moderate this quenching require further investigation.

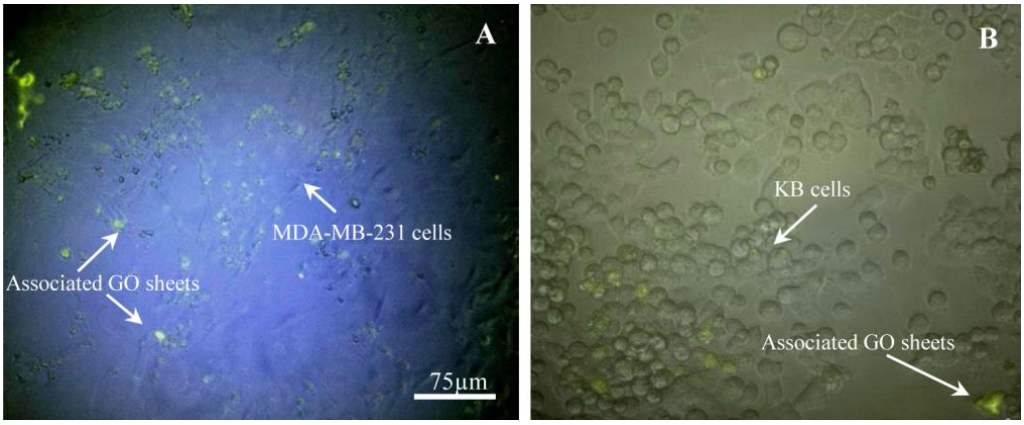

Figure 3-16. Fluorescence microscopy images of incubated tumor cells with PEGylated GO.

A) MDA-MB-231 and B) KB cells when incubated with GO-PEG (260 µg.ml^{-1}) for 48 h and imaged using a green N3 filter cube N3. Arrows indicate cells and fluorescence-associated GO sheets. The images show that the GO sheets are associated with both types of cells.

3.1.5.2 Confocal microscopy studies

The cellular uptake of the GO-PEG with a concentration of 260 µg.ml^{-1} was imaged using confocal microscopy. The series of different focal planes (Figure 3-17) acquired through the sample (Z-stack) shows that the GO-PEG sheets were taken up by the KB cells. This confirms the fluorescence data (Figure 3-16) shown above. Cell membrane excited at 564 nm and measured at 600 nm shows a deep red fluorescence. The GO-PEG when excited at 480 nm and measured at 527 nm shows a bright green fluorescence. As mentioned earlier, green fluorescence was quenched in 48 h (toxicity) studies, while it is detectable in 12h confocal imaging. This probably shows the importance of incubation time in observed optical properties. It seems by the passage of time the intracellular particles' fluorescence is quenched possibly due to some intracellular functions. More investigation is required to study this assumption.

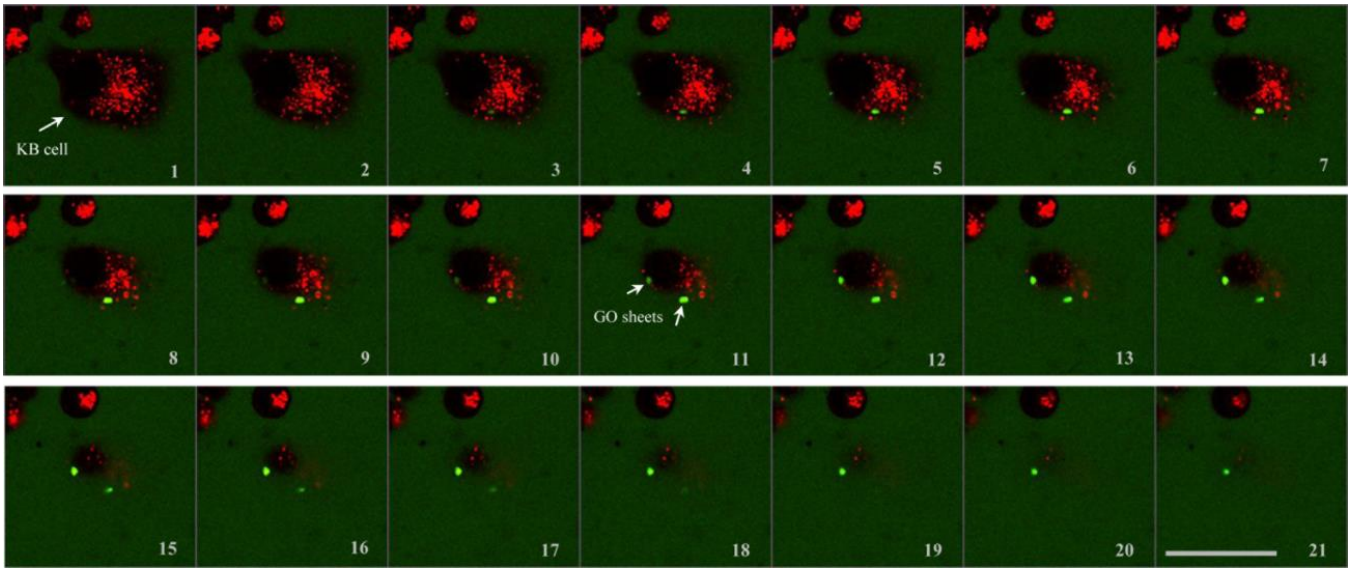

Figure 3-17. Confocal images of the KB cell incubated with the GO-PEG for 12 hours (Overnight).

The series of different focal planes (1-21) acquired through the sample (Z-stack) shows that the GO sheets (green spots/white arrows) are internalized into the KB cell (deep red staining). White scale bar is 125 µm.

3.1.6 Cytoxicity assay of the single GO nano-sheets

Looking at literature, there are inconsistent observations for graphene oxide cytotoxicity [70, 71]; there are several studies reported GO as non-toxic carbon polymer and totally safe for clinical application [72], while others have reported the opposite [52, 73-75]. Further, based on previous studies, the toxicity of the GO and even the GO-PEG is concentration dependent [52, 71, 75-77].

Cytotoxicity of the GO-PEG in this study was determined by utilising the highly water-soluble WST-8 tetrazolium (CCK-8, sigma) and the MTS tetrazolium (CellTiter 96 aqueous one solution assay, Promega) for KB and MDA-MB-231 (tumour) cells (Figure 3-19).

WST-8 and MTS are two enzyme-based methods, which rely on the dehydrogenases in a viable cell. They receive the necessary electrons to generate the coloured formazan compounds from viable cells utilising NADP (H) and NAD (H) [78].

WST-8 reagent is not cell permeable, and must receive the required electron(s) for the reductive process at the level of the cell membrane. The colour change reflects cell mitochondrial activity and membrane integrity due to transferred electrons via plasma/membrane electron transporter. This reduction is also inhibited by low levels of superoxide, which indirectly shows the produced levels of superoxide inside the cell

[78]. MTS as a weakly permeable molecule however, reduces intra-cellularly. This reduction process involves several dehydrogenases providing more direct information on the cellular metabolic activity [78].

Cytotoxicity study of GO-PEG on tumour cells would be the first step. The result (toxic or nontoxic effects) determines the subsequent steps:

- Toxicity of PEG-GO: Studying the non-tumour cells is required. Non-toxicity in non-tumour cells, confirms the effectiveness of PEG-GO in cancer treatment.

- Non-toxicity of PEG-GO: Cytotoxicity study on tumour cells after more modification (attaching ligands), confirms the toxic effects of GO-PEG-ligand and the result should compare to non-tumour cells.

To determine cell viability with a colorimetric method cells were treated with different concentrations of GO-PEG (0-260 $\mu g.ml^{-1}$) for 48 hours (Figure 3-18). Functionalised GO sheets have no detectable impact on cell viability at concentrations up to 90 $\mu g.ml^{-1}$ for both assays. The cell viability was 97±2 % (A) and 99±1 % (B) at 30 µg/ml, 95±2% (A) and 98±2% (B) at 90 $\mu g.ml^{-1}$ and decreased marginally to 88±3% (A) and 88±2% (B) at 260 $\mu g.ml^{-1}$. This lack of cytotoxicity is an important observation as GO sheets are being developed for drug delivery for cancer treatments, where size scale plays a critical role in the distribution and selectivity of these engineered materials.

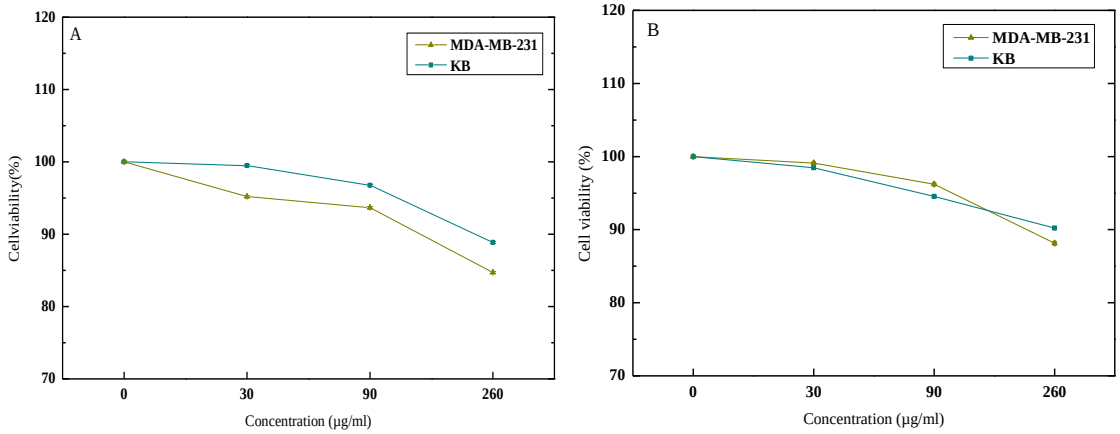

Figure 3-18. Effect of GO-PEG on viability of KB and MDA-MB-231 cells

Cells were treated with increasing concentrations of GO PEGylated sheets for 48 hours; A) Cell viability was determined using WST cell toxicity reagent. B) Cell viability was determined using MTS reagent. All data is expressed as mean ± SD (*n*=3).

3.4 Conclusions

This paper presents a water-glycerol gradient centrifugation method for the separation and fractionation of GO single sheets in the size range of 150 to 850 nm. As the sheet size increases, the measured electrophoretic mobility of the separated sheets increases from -0.2 to -1.4 μm.cm/V·sec where the interpreted zeta potentials range from -3 mV to -17 mV. Spectroscopic measurements on the single sheets indicate the same pattern of auto-fluorescence in 200 nm excitation wavelength for all the separated fractions (GOF_1-GOF_4), suggesting that the emission intensity is size independent. The observed auto-fluorescence of GO PEGylated sheets (GO-PEG) is shown to be evidently bright and strongly affected by some undetermined environmental factors, which are under investigation. Furthermore, GO-PEG is shown to be non-cytotoxic at increasing concentrations up to 90 $\mu g.ml^{-1}$. Small reduced cell viability is observed at the concentration of 260 $\mu g.ml^{-1}$. It is concluded that the GO PEGylated sheets have potential applications in cell signalling and tracking in clinical studies. The proposed separation and fractionation method is relatively simple and easy to use in biomedical studies where the proper nano-sizes of GO is desired (from 100 nm to less than 800 nm), depends on the intended application. Furthermore, the solvents used are not cytotoxic rendering the GO sheets less cytotoxic.

Chapter 4

Graphene Oxide as a Photoluminated Carrier

4 Graphene Oxide as a Photoluminated Carrier

4.1 Introduction

The photoluminescence of carbon polymers is a consequence of the recombination of localised π electrons in sp^2 clusters, which basically behave as chromophores [335]. The photoluminescent transition depends on the size, symmetry and shape of the involved sp^2 sites, as well as the topology of other sp^2 domains and the surrounding sp^3 matrix. Therefore, controlling the size of sp^2 clusters and superficially oxidised carbons can directly affect the observed photoluminescence [335, 336]. The optoelectrical property of graphene oxide (GO) as a carbon polymer is always determined by the π states of these sp^2 clusters. The π and π* electronic states of the sp^2 sites are situated within the levels of the σ and σ* gaps in the sp^3 matrix [336]. The fundamental electronic transition in GO sheets during fluorescence phenomena is shown in Figure 4-1 [336]. The size of sp^2 clusters defines the local energy slit and hence the wavelength of the observed emission [95]. The combined emission structure has no signature feature, due to the presence of different sizes of sp^2 clusters in GO. Emission in the ultraviolet–visible region mostly occurs from the smallest sp^2 clusters (from as few as 20 aromatic rings, but less than 1 nm). On the other hand, the larger sp^2 domains (more than 2 nm) hold smaller gaps which result in emissions in the red to near-infrared (NIR) regions.

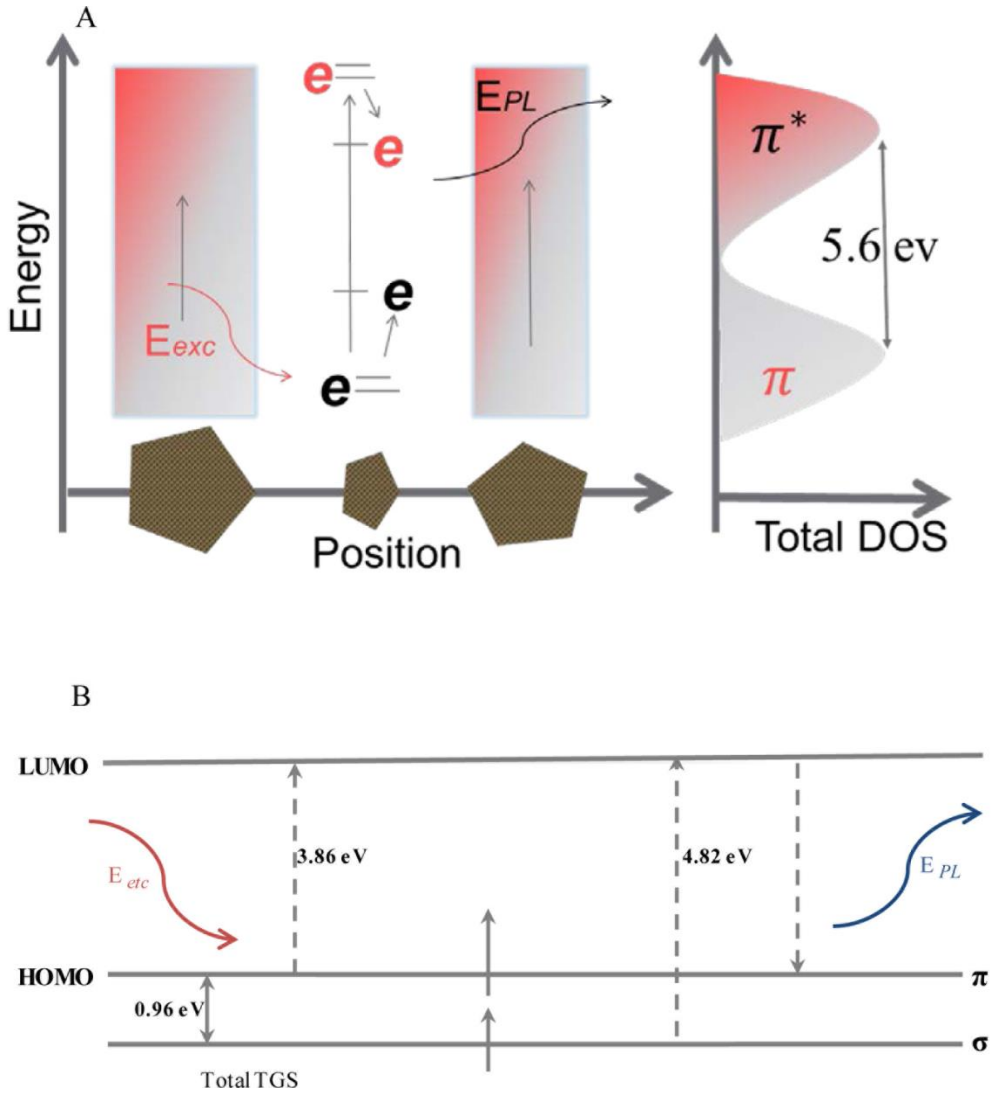

Figure 4-1. The schematic band structure of GO.

A) The energy levels are quantised with small fragments showing large energy gaps due to confinement (red and grey represent transmission and valence bands, respectively). Smaller sp^2 domains have a larger energy slit (grey arrows) due to a stronger internment effect. Photo-generation of an electron–hole pair on the absorption of light (E_{etc}) is followed by non-radiative relaxation and radiative recombination, resulting in fluorescence (E_{PL}). DOS represents the total electronic density of transmitted states. B) Typical electronic transitions of triple carbenes at zigzag sites observed in the optical spectrum showing the difference at energy gaps assigned to the size of sp^2 clusters represented in part A. The triplet ground state (TGS) is related to the energy difference between the σ and π molecular orbitals.

In fact, the transitions from the highest occupied molecular orbitals (HOMOs) for σ and π states to the lowest unoccupied molecular orbitals (LUMOs) resulted in fluorescence as presented in figure 4-2 [337]. Note, the photoluminescence of GO originates from the recombination of electronic transitions between the non-oxidised carbons (i.e. C=C) and oxidised regions, rather than just band-edge transitions as in typical semiconductors [336, 338].

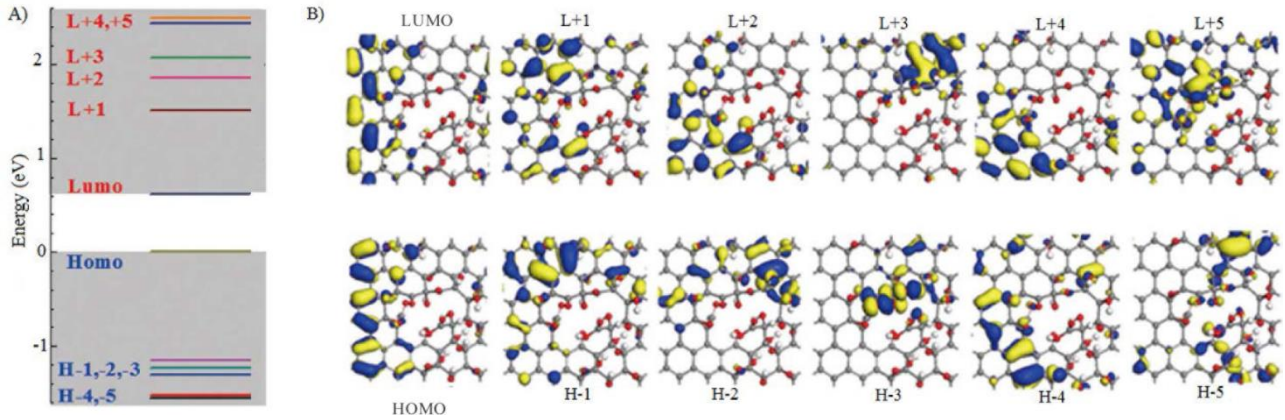

Figure 4-2. Orbital energies of GO

A) The molecular orbital energy levels of GO. B) The structurally related orbitals of GO [338].

The photoluminescence of GO and its fluorescence quenching effect on various attached fluorescents has been widely studied [336, 339, 340]. It has been shown that the quenching effect arises from either fluorescence energy transmission from sp^2 domains to the attached fluorescent molecules or non-fluorescent dipole–dipole coupling between the fluorescent reagent and GO [243, 336, 338, 341]. There currently exist no reports of research into the auto-fluorescence of individual GO sheets using fluorescence microscopy. In this chapter, the wide spectrum of fluorescence emission (400-700 nm) of GO single sheets was studied using excitation in the range of 200 nm to 600 nm. GO shows the ability to emit in almost three main fluorescence regions (blue, green and red). Furthermore, the impacts of various factors on the observed emission spectra and the measured intensity were also investigated. As a result, GO sheets have the potential to be used as a carrier for drug delivery purposes [216, 240, 342]. They also have their own fluorescence making them visible in *in vivo* experiments, which could be very valuable in biomedical studies.

4.2 Materials and Methods

4.2.1 Materials

GO solution (4 $mg.ml^{-1}$) and Dulbecco's Modified Eagle's Medium (DMEM) were purchased from Sigma-Aldrich. For this study a diluted aqueous solution of GO (0.2 $mg.ml^{-1}$) was prepared. Hydrochloric acid (HCl) 37% was purchased from Merck. Sodium hydroxide (NaOH), chloroacetic acid ($ClCH_2CO_2H$) and salts to prepare phosphate buffered saline (PBS), including sodium chloride (NaCl), potassium chloride (KCl), sodium hydrogen phosphate (Na_2HPO_4) and potassium dihydrogen phosphate (KH_2PO_4) were purchased from Chem-Supply.

The optical properties of GO were characterised by UV-Vis spectroscopy (Varian 3E UV-visible spectrophotometer) and fluorescence spectrophotometry (Varian fluorescence spectrophotometer) in which excitation occurred over the range of different wavelengths. A fluorescence microscope (Leica DMI 6000 B) was used to observe the auto-fluorescence of GO sheets using three filters: FITC (green), DAPI (blue) and N3 (red). These are the most common excitation filter cubes in biological studies.

4.2.2 Methods

PBS buffer was made by dissolving 8 g of NaCl, 0.2 g of KCl, 1.44 g of Na_2HPO_4 and 0.24 g of KH_2PO_4 in 800 ml distilled water. The pH was first adjusted to 7.4 with HCl, followed by the addition of distilled water to adjust the volume to 1 L. The solution was finally sterilised using an autoclave.

Cell imaging study was performed using KB and MDA-MB231 cell lines, which were previously described in chapter 3. Each cell line was grown to confluence in 80 cm flasks in DMEM medium (supplemented with 10% foetal bovine serum (FBS), 1% L-glutamine and 1% penicillin-streptomycin (Pen-Strep); all from Sigma) at 37 °C in a 5% CO_2 atmosphere with 95-100% humidity. On the day of the experiment, cells were trypsinised off the T-flask using 0.05% Trypsin-EDTA (Sigma). The trypsinated cells were counted manually using trypan blue as the live/dead stain (Sigma). The cells were then diluted with fresh medium to reach a density of 5×10^4/ml in 96 well plates (NUNC) at a seeding volume of 100 µl/well. 6 wells were left unseeded to serve as cell-blank controls.

After 24 h of incubation, the cells were starved by replacing the complete media containing FBS by incomplete media (media without serum) for another 24 h. The polymer test solution, which consisted of PEGylated GO solution sterilised by UV for 10 min and then diluted to 10 $mg.ml^{-1}$ using PBS, was then added as a 10 µl aliquot to each of three wells in the 96 well plate, and gently mixed by orbital movement of the plates. The plates were then returned to the incubator for a further 48 h.

4.3 Results and Discussion

4.3.1 UV-Visible Absorbance Study

The optical properties of GO single sheets were monitored using UV-Vis spectrophotometry (Figure 4-3). The UV-Vis spectrum of the GO solution showed two absorption peaks: one at 230 nm, which corresponds to the $\pi \rightarrow \pi^*$ transition of aromatic C=C bonds, and a second small shoulder at around 298 nm that was attributed to the $\sigma \rightarrow \pi^*$ transition (the excitation of an electron from one of the non-bonding pairs to the π^* orbital) of C=O bonds in the carboxylic groups [343, 344].

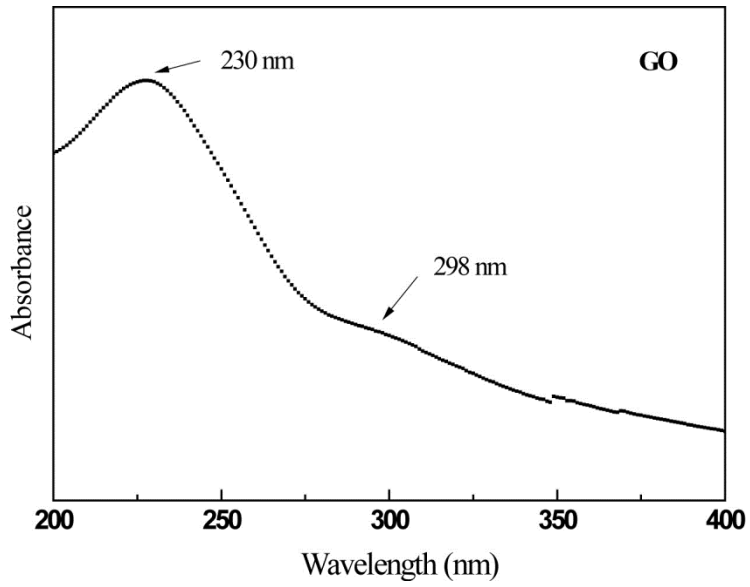

Figure 4-3. UV-Vis absorbance spectrum of dilute aqueous GO.

This figure show two absorption peaks: one at 230 nm corresponded to the $\pi \rightarrow \pi^*$ transition of aromatic C=C bonds, and a second small shoulder at 298 nm attributed to the $\sigma \rightarrow \pi^*$ transition.

Carboxylated GO (GO-COOH) and PEGylated GO (GO-PEG, where PEG is polyethylene glycol) showed slightly different absorbance spectra, as discussed in chapter 3 (Figure 3-9 and Figure 3-13, respectively).

4.3.2 Fluorescence Absorbance Study

The fluorescence emission (400-700 nm) when dilute aqueous GO was excited at three different excitation wavelengths of 200, 230 and 250 nm is shown in Figure 4-4. The observed spectra reveal the interesting photophysics of GO. The emission magnitude, however, does not follow the excitation trend observed in the UV-Vis absorbance spectrum, and this should be further investigated. The fluorescence spectra indicate the capability of GO to emit in a wide range of wavelengths including the three main fluorescence regions of blue, green and red. The observed emission intensity was higher in the blue and green regions.

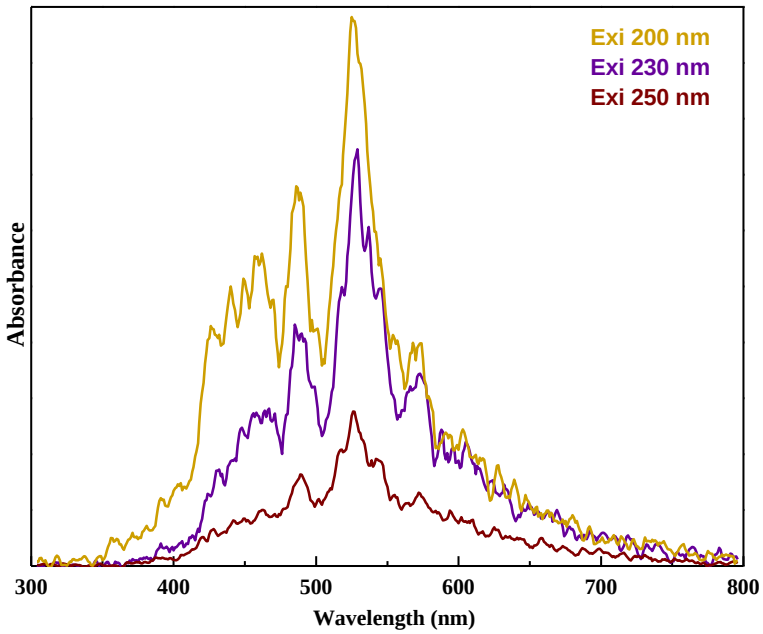

Figure 4-4. Emission spectra of GO at 200, 230 and 250 nm excitation wavelengths.

The inset shows the 230 nm and 250 nm excitation peaks in the same position as the 200 nm excitation. The observed intensities are not proportional to the measured absorbance intensities.

Evidently, there is a distinguishable pattern of fluorescence emission in all three excitation wavelengths; however, the emission pattern appeared to be independent of the excitation wavelength. Interesting emission patterns can also be observed at longer wavelengths. The spectrum of the fluorescence emission (400-700 nm) of solutions of GO is shown in Figure 4-5, when excitation occurs over the visible range of 400 to 600 nm. This figure shows the reflection of the excitation wavelengths. However, there are some emission peaks at 480 and 540 nm, and broad peaks between 580 and 640 nm. The observed spectrum varies widely and shows the capability of GO to emit in the three main fluorescence regions of blue, green and red, depending on the excitation wavelengths. Excitation at 400 nm showed a wide emission pattern that almost covers the three main fluorescence regions. The emission peaks over the range of 500 nm to 550 nm wavelengths (green region) were observed when GO was excited at 400 nm to 500 nm. An excitation wavelength of 550 nm produced less intense green fluorescence than 500 nm. Emission at only red region was observed when the excitation occurred at 600 nm. In general, the features of the observed spectra were mostly the observed reflections of the applied excitation wavelengths in some regions.

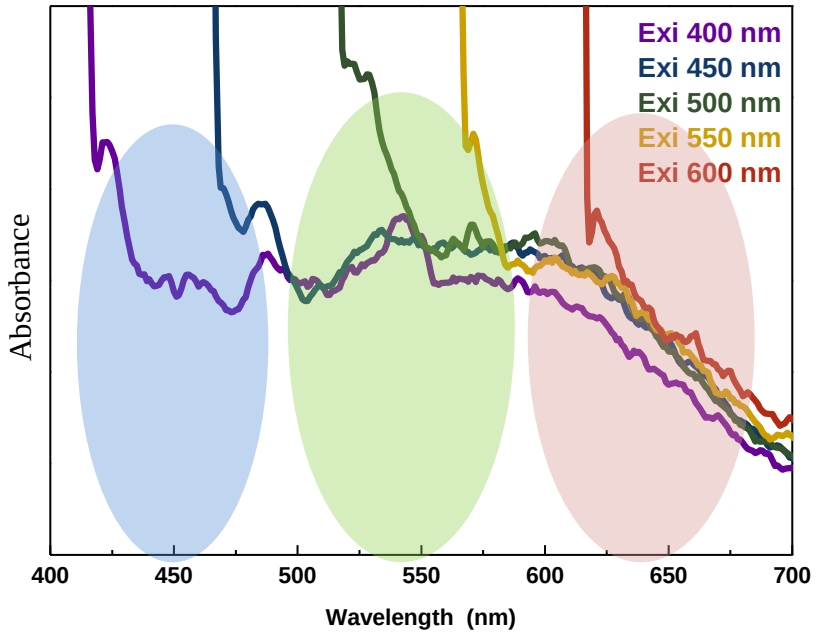

Figure 4-5. Fluorescence emission spectra of dilute aqueous GO over the range of 400 nm to 600 nm excitation wavelengths.

This figure shows the reflection of the excitation wavelengths. However, there are some emission peaks at 480 and 540 nm, and broad peaks between 580 and 640 nm.

The following sections discuss the photoluminescence of GO and its functionalised derivatives at different conditions in order to better understand this phenomenon. Unless stated otherwise, the aqueous GO solutions were excited at 200 nm.

4.3.2.1 The effects of chemical functionalisation on fluorescence spectra

Remarkably, GO and its functionalised derivatives, e.g. GO-COOH, GO-PEG and folic acid-PEGylated GO (GO-PEG-FA) have significantly different emission spectra at 200 nm excitation wavelength. The surface chemical structure can have a large effect on the observed emission patterns, particularly when GO was functionalised, probably because of the role of oxidised regions in the origin of fluorescence (Figure 4-6). This result demonstrated that the functionalised groups and/or oxidised carbons, along with non-oxidised domains, were absolutely involved in causing the observed emission spectra of GO [338]. Apart from the intensity, which was increased by PEGylation, the spectral patterns were also slightly different for the various GO derivatives. The common emission in all types of GO materials peaked at around 430, 490 and 530 nm, which corresponded to blue and green emission regions. Emission in the red fluorescent region was not as intense as the green or blue bands; however, with chemical modification, i.e. PEGylation, it became more intense.

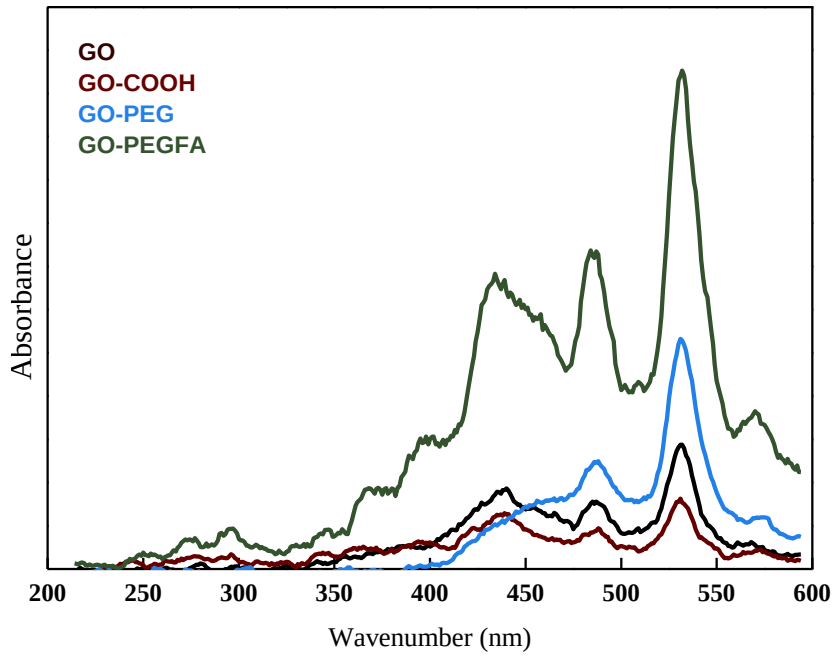

Figure 4-6. Fluorescence emission spectra of GO and functionalised derivatives at 200 nm excitation wavelength.

The common emission in all types of GO materials peaked at around 430, 490 and 530 nm, which corresponded to blue and green emission regions. Emission in the red fluorescent region is not as intense as the green or blue bands.

4.3.2.2 The influence of solution pH on fluorescence intensity

One major difference between many tumours and surrounding non-tumour tissues is the metabolic environment. The vasculature of tumours is often inadequate to supply the nutritional needs of tumour cells. Production of lactic acid under these anaerobic conditions contributes to the acidic microenvironment as an inherent property in many types of tumour [13, 14]. This needs to be considered when designing therapeutical conjugates for imaging or tracking purposes, either inside of the cells as endosomes or outside in the tumour area.

The fluorescence intensity of GO sheets is pH-dependent. This fluorescence was studied at three different pH conditions, moderately acidic (pH=4), physiological (pH=7.4) and basic (pH=10), at 200 nm excitation wavelength (Figure 4-7). The intensity of the observed emission appeared to be higher at basic and natural conditions, while it decreased in the acidic solution. This change in intensity was fundamentally related to electron transitions at the GO planar surface, with a corresponding transfer of

protons (H^+) between GO sheets and the surrounding solution. This phenomenon is presented schematically in Figure 4-8 [345].

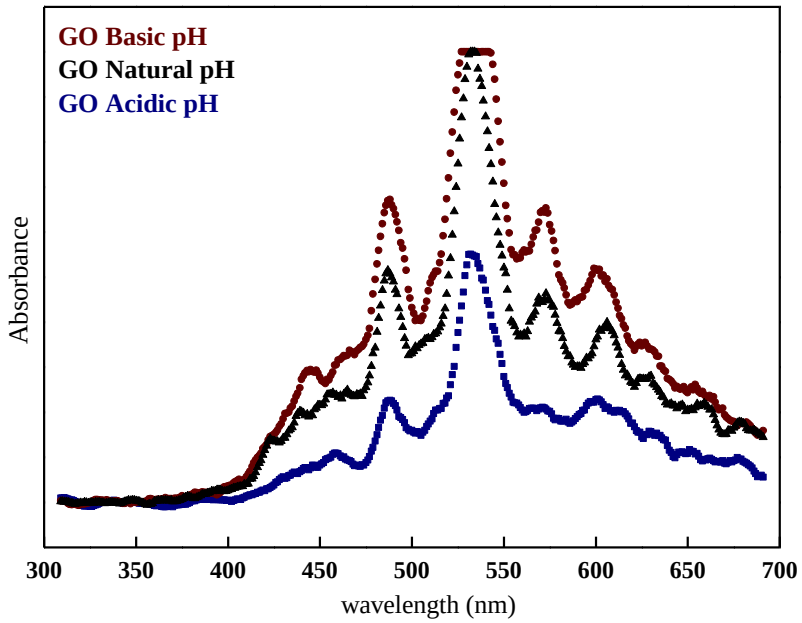

Figure 4-7. Fluorescence emission spectra of GO excited at 200nm wavelength.

Under acidic, natural and basic pH conditions, which were pH 4, 7.4 and 10, respectively.

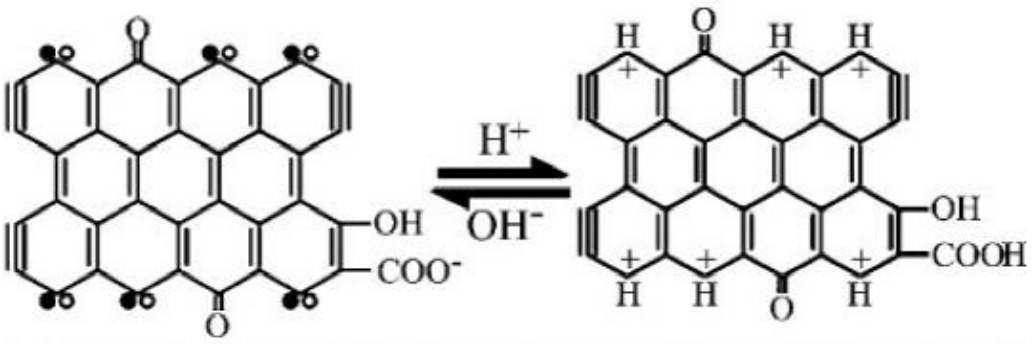

Figure 4-8.Schematic representation of GO sheets.

In basic (left) and acidic (right) solutions. The filled circles represent σ electrons and the empty circles correspond to π electrons [337, 345].

The literature suggests that the photoluminescence of GO-polymer may initiate from its free zigzag domains and the triplet ground state (TGS). This mechanism, based on the emissive free zigzag spots, is supported by the observed pH-dependent fluorescence in Figure 7. Additionally, the intensity of fluorescence should vary

reversibly based on the proposed model in Figure 4-8 [345]. Thus, in acidic conditions, the free zigzag domains of GO will be protonated, forming a reversible compound between the free and protonated zigzags. Therefore, the TGS will be broken and becomes inactive, resulting in less fluorescence. On the other hand, under basic conditions, the free zigzag sites will be restored, leading to the restoration of fluorescence and giving rise to higher intensities. This also might be due to the protonation and deprotonation effects in acidic and basic conditions, respectively, depending on the chemistry of the molecules (i.e. oxidised groups and the adjacent sp^2 domains) [338, 346].

Interestingly, the same effect was observed for functionalised GO, as shown in Figure 4-9. PEGylated GO (i.e. GO-PEG) exhibited more intense emission at basic conditions, while acidic pH reduced the intensity. This phenomenon may partially explain the reduction in fluorescence of GO sheets in the acidic environment around tumour cells. The observed fluorescence in cellular imaging will be discussed in chapter 5.

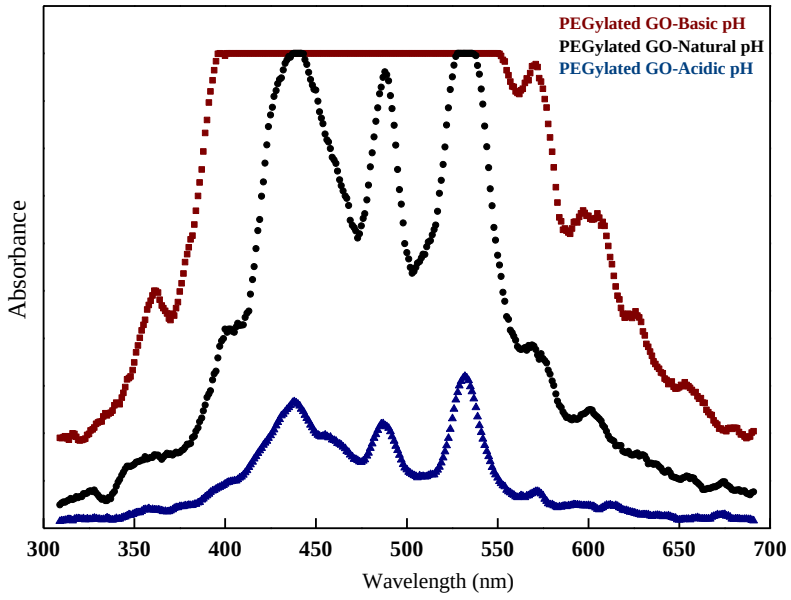

Figure 4-9. Fluorescence emission spectra of GO-PEG excited at 200 nm wavelength.

Under acidic, natural and basic pH conditions, which were pH 4, 7.4 and 10, respectively.

4.3.2.3 The influence of concentration on fluorescence intensity

Finding non-fluorescent, aggregated GO sheets around tumour cells prompted a study of the effect of concentration on the observed fluorescence, which revealed that the photoluminescence of GO was concentration dependent, consistent with previous reports [335]. Therefore, GO solutions were prepared at different concentrations of 0.2, 0.5 and 1.0 $mg.ml^{-1}$ to study the effect of GO aggregation on the observed emission spectra at 200 nm excitation wavelength. As is shown in Figure 4-10 with increasing GO concentration the fluorescence, intensity of the sheets significantly decreases, while the intensity of the most concentrated solution being just 1/5 of the dilute solution. This explains the observation of non-fluorescent aggregated sheets in cell media during cellular imaging which will be discussed in the following sections.

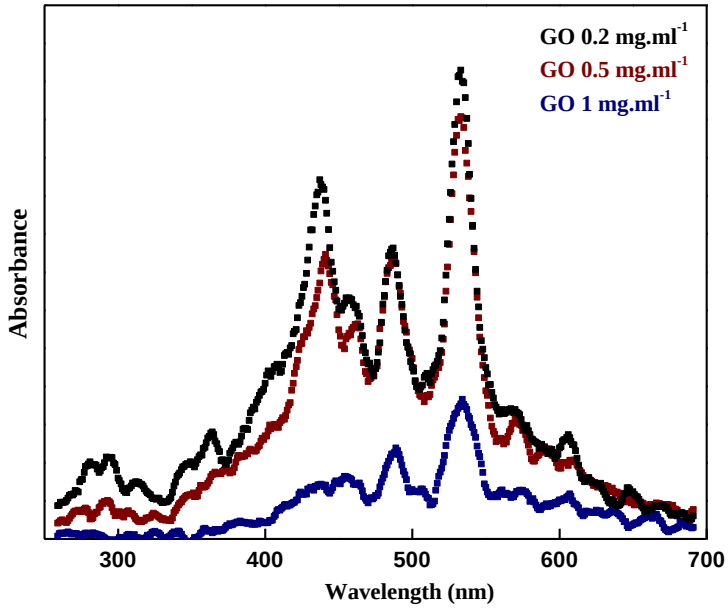

Figure 4-10. Fluorescence emission spectra of GO sheets at different concentrations.

The fluorescence intensity of the sheets significantly decreases with increasing GO concentration.

4.3.2.4 The effect of media on fluorescence property

GO, and particularly derivatised GO, must be dissolved in PBS (a common biological buffer) or cell media for biomedical applications. Therefore, the emission spectra of GO sheets were obtained in two different physiological Solutions: PBS and cell media (DMEM). This study showed the effect of the underlying media on the measured intensity and pattern of the observed fluorescence.

Figure 4-11 presents the emission patterns of GO at four different excitation wavelengths in each solution. Evidently, the medium has an impact on both the spectral features and the intensity of fluorescence at the four examined excitation wavelengths. In addition, the emissions patterns for GO in PBS and DMEM were quite different from each other, as well as in aqueous solution (Figure 4-4). Apart from the different spectra of GO in PBS and DMEM when excited at 200 nm, there was no measurable emission intensity for 350 nm excitation wavelength when GO was dissolved in PBS. However, at this wavelength moderate peaks in the blue and green regions were detected. At 400 nm excitation, the pattern was almost the same as at 350 nm, apart from a small difference in the observed intensity, which can be ignored. The emission pattern at 488 nm showed much more variance in the measured intensity. Significantly, GO emits more intensely at around 530 nm in PBS, compared to the excitation at 488 nm for DMEM.

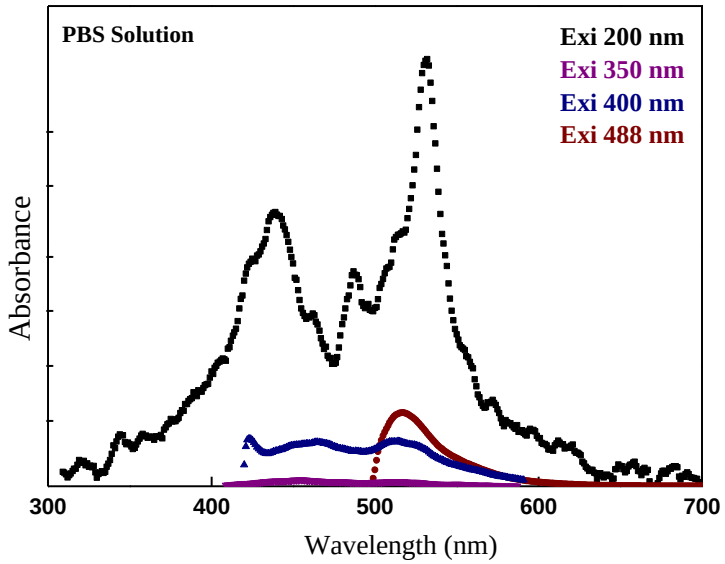

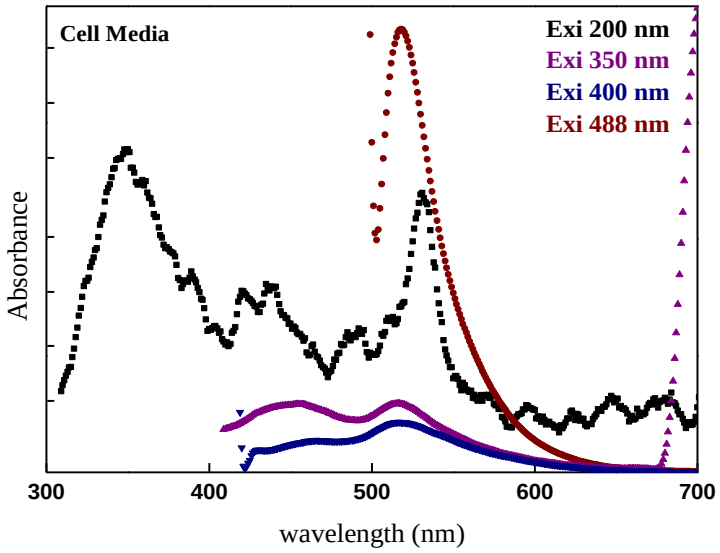

Figure 4-11. Fluorescence emission spectra of GO in PBS and DMEM cell media.

The medium has an impact on both the spectral features and the intensity of fluorescence at the four examined excitation wavelengths.

4.3.3 Fluorescence Microscopy of the Individual GO Sheets

Fluorescence microscopy also confirmed the photoluminescence of individual GO sheets in the blue, green and red bands. In Figure 4-12, the same sample of GO sheets suspended in PBS can be seen fluorescing under different filter cubes, including DAPI for blue, FITC for green and N3 for red fluorescence.

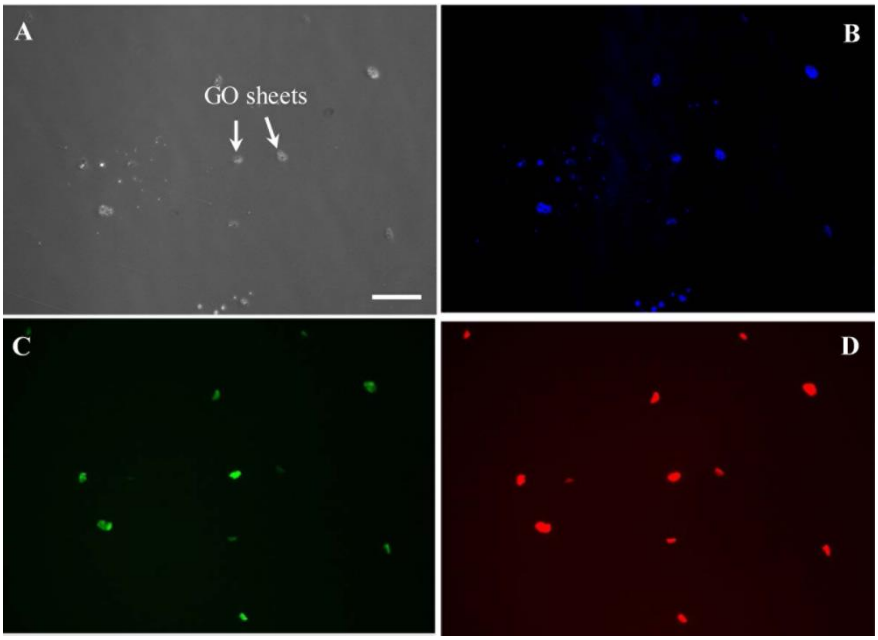

Figure 4-12. Fluorescence microscopy photographs of the same sample of GO dissolved in PBS using different excitation filters.

A) Bright field. B) Blue auto-fluorescence using DAPI filter. C) Green auto-fluorescence using FITC filter. D) Red fluorescence using N3 filter. (Scale bar: 100 µm.) In A) the white arrows indicate the GO sheets.

The same sample of GO was also examined *in vitro* in DMEM media. As shown in Figure 4-13, GO sheets showed the fluorescent property at all three previously observed regions while they were floating on top of cells. In Figure 4-13A cells can be seen on the bottom of the well.

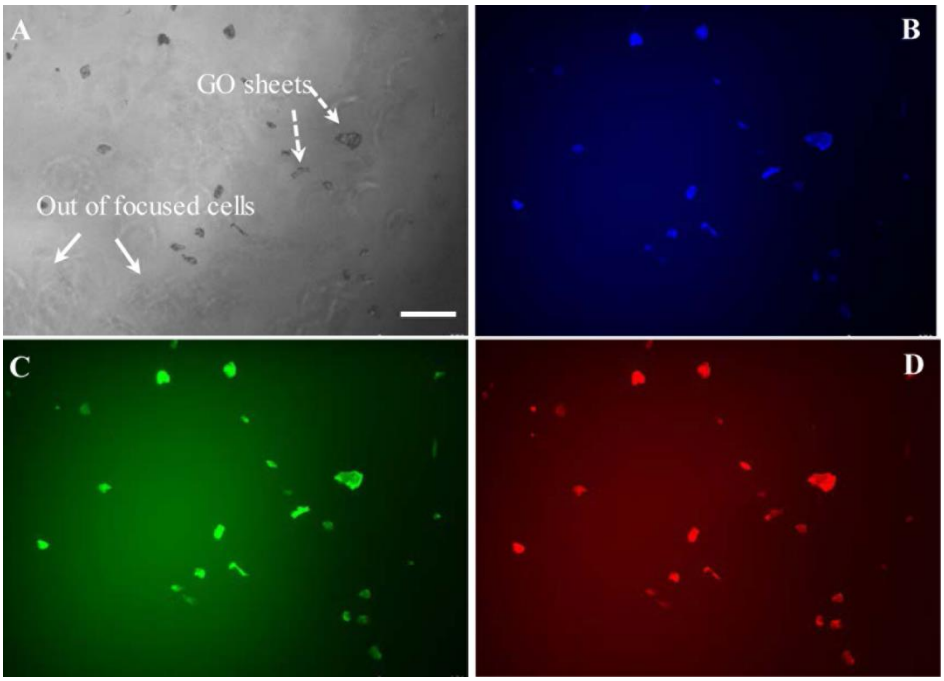

Figure 4-13. Fluorescence microscopy photographs of the same sample of GO dissolved in cell media using different excitation filters.

A) Bright field. B) Blue auto-fluorescence using DAPI filter. C) Green auto-fluorescence using FITC filter. D) Red fluorescence of GO using N3 filter. (Scale bar: 100 µm.) In A) the solid white arrows indicate the cells on the bottom of well (out of focus), and the dashed arrows show the GO sheets.

4.3.4 PEGylated GO Sheets for Cell Imaging

The KB and MDA-MB231 cells treated with modified GO-PEG networks were imaged using fluorescence microscopy, as shown in Figure 4-14. Red and blue auto-fluorescence of internalised GO-PEG sheets was observed after 48 h of incubation,

while green fluorescence was not detected using an FITC filter cube. This might be due to the quenching effect of the acidic environment around the cells (Section 4.3.2.2), as individual sheets were observed to fluoresce brightly green when GO was dissolved in PBS or DMEM media (Section 4.3.3). Notably, the aggregated GO sheets (Figure 14a and d) did not show any fluorescence, as explained in section 4.3.3. Although the details of the chemical and physical aspects of the observed fluorescence phenomenon need more investigation, these results suggest GO may have potential in imaging applications.

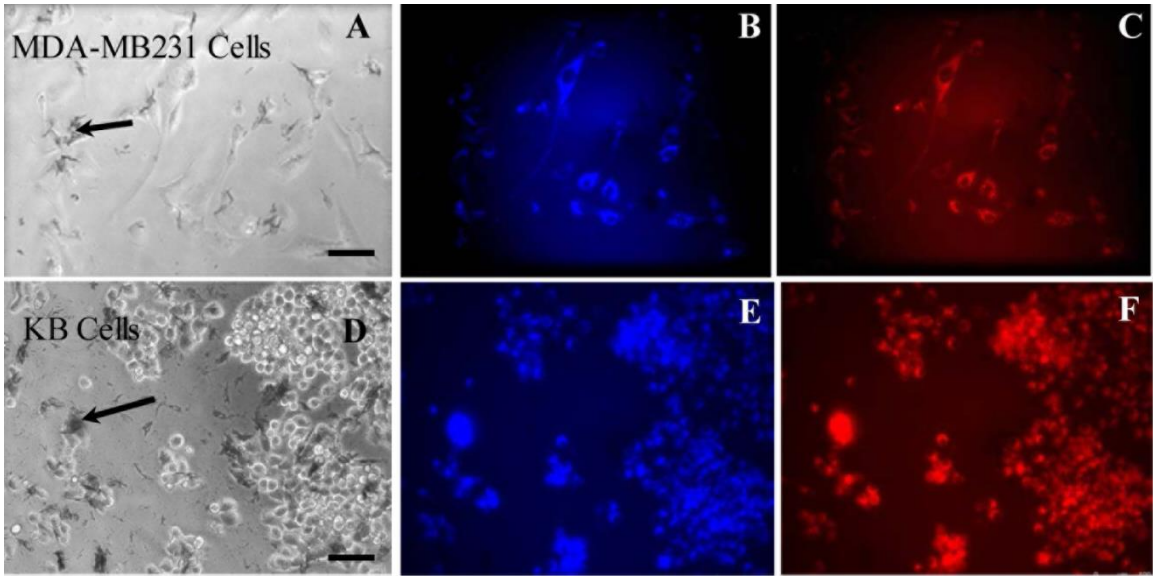

Figure 4-14. Fluorescence microscopy photographs of incubated tumor cells with PEGylated GO.

A-C) MDA-MB231 cells, and D-F) KB cells when incubated with GO-PEG sheets for 48 h. (Scale bar: 100 µm.) The black arrows in a) and d) indicate non-fluorescing aggregated GO sheets.

4.4 Conclusions

The fluorescence of GO in water, PBS and cell media was studied under various conditions. Spectroscopic measurements showed that single GO sheets can auto-fluoresce over the range of 400 nm to 700 nm when excitement occurs at the range of 200 nm to 250 nm. The wide emission spectrum covers the main fluorescence regions. However, emission spectra of GO in other ranges of excitation wavelengths (400 nm to 600 nm) indicated that GO was possibly reflecting the excitation wavelengths. Furthermore, there were detected emission peaks at 480 and 540 nm, and broad peaks over 580 nm to 640 nm. This fluorescence could also be used to trace GO sheets in solution. GO and derivatised GO have stronger fluorescence at higher pH, while lowering the pH reduces the measured intensity. This might be due to the protonation and deprotonation effects in acidic and basic conditions, respectively, depending on the chemistry of the molecules (i.e. oxidised groups and the adjacent sp^2 domains). The data also indicated that functionalised groups make an important contribution to the fluorescence. Fluorescence microscopy demonstrated the photoluminescence of individual GO sheets in the blue, green and red regions. The lack of fluorescence of some GO sheets in cell media might be due to aggregation of the sheets. Based on the observations in this chapter, GO auto-fluorescence seems to be complicated and is dependent on various chemical and physical factors, and further work will be required to understand the influence of the environmental and aggregation effects on the fluorescence of GO. Nevertheless, GO sheets have the potential to act as tracers in biological systems, and may also be used as a carrier in drug delivery applications.

Chapter 5

Targeted graphene oxide based nanoparticles:

cytotoxicity and synergy with anticancer agents

5 Functionalised GO Networks as a Potential Nano-Carrier/Treatment for Cancer

5.1 Introduction

Tumour cells often over-express certain receptors concerned with nutrient uptake to support the metabolic demands of rapid growth [347, 348]. For example, folate receptors are found on the surface of tumour cells, while they are not generally expressed on non-tumour cells [71, 122, 349-353]. This receptor has been considered as one of the best candidates for selective targeting by a variety of folate receptor binding therapeutic conjugates [70, 354], some of which have shown positive results in clinical cancer studies [355, 356]. This receptor not only assists ligand association of the therapeutic conjugates on the cell surface, but also acts as a carrier for transferring extracellular drugs/nanocarriers inside of the cells [123, 157].

To date, the folate receptor has been mostly utilised as a targeting molecule to deliver drugs or diagnostic compounds to tumour cells [123, 161, 162]. In 2015, however, Wen et al. examined the ability of monoclonal antibodies to target and block folate receptors. This approach showed detectable antitumor activity in ovarian cancer models (in which there is known to be a high level of folate receptor expression on tumour cells) [357].

The tripeptide Arg-Gly-Asp (RGD) is also one of the most attractive ligands for delivery purposes due to its better cellular uptake and ease of synthesis [95]. It is sufficiently small with lower immunogenicity and higher stability [178]. RGD targets a number of different integrins, the essential heterodimer membrane receptors that are required for cell adhesion to the extra cellular matrix (ECM) [358]. Certain types of these integrin receptors are upregulated in tumour cells, and play key roles in initiation and evolution of tumour angiogenesis and metastasis [173, 175, 358]. RGD as a targeting agent has improved the capacity to deliver anti-cancer or imaging molecules in different tumour models [71, 358]. This targeting ligand can be also used to inhibit tumour cell spread and migration [173]. However, this ligand can also bind to non-tumour classes of integrin ($\alpha5\beta1$ and $\alpha4\beta1$) causing adverse effects [71] and therefore is not specific for tumour cell targeting.

Despite remarkable successes in experimental targeted drug delivery systems, few strategies are available for clinical use and cancer therapy is still limited by adverse effects and resistance to chemotherapeutic drugs [71, 359]. Therefore, the combination of two distinct ligands enhances the efficacy and the safety of the applied conjugates [213, 214].

In the present study, the PEG molecule was employed to modify the GO polymer to provide a bifunctional polymeric linker [240, 242, 243], introducing two different GO conjugates (FA or RGD-PEGylated GO as a single ligand and FARGD-PEGylated GO as dual ligand GO) to develop a simple surface functionalisation. It was proposed that the folate receptors and integrins can be blocked by these derivatised PEG-GO sheets. Blocking these receptors may prevent endocytosis of FA/FR complexes and clustering of integrins thereby rendering the tumour cells incapable of replication [136, 360, 361] and proper adhesion [362-364] (Figure 5-1). The cytotoxicity of the modified GO networks on three different cell lines, tumour (KB) and non-tumour cells (BEAS-2B, fibroblast), was examined using the well-established WST toxicity/proliferation assay. The combination of the modified polymeric networks with two common anti-cancer drugs, methotrexate (MTX) and doxorubicin (DOX) was investigated to establish the potential for synergistic effects. To understand the impact of the modified GO on cellular function, confocal live imaging was performed utilising the fluorescence properties of GO and its derivatives.

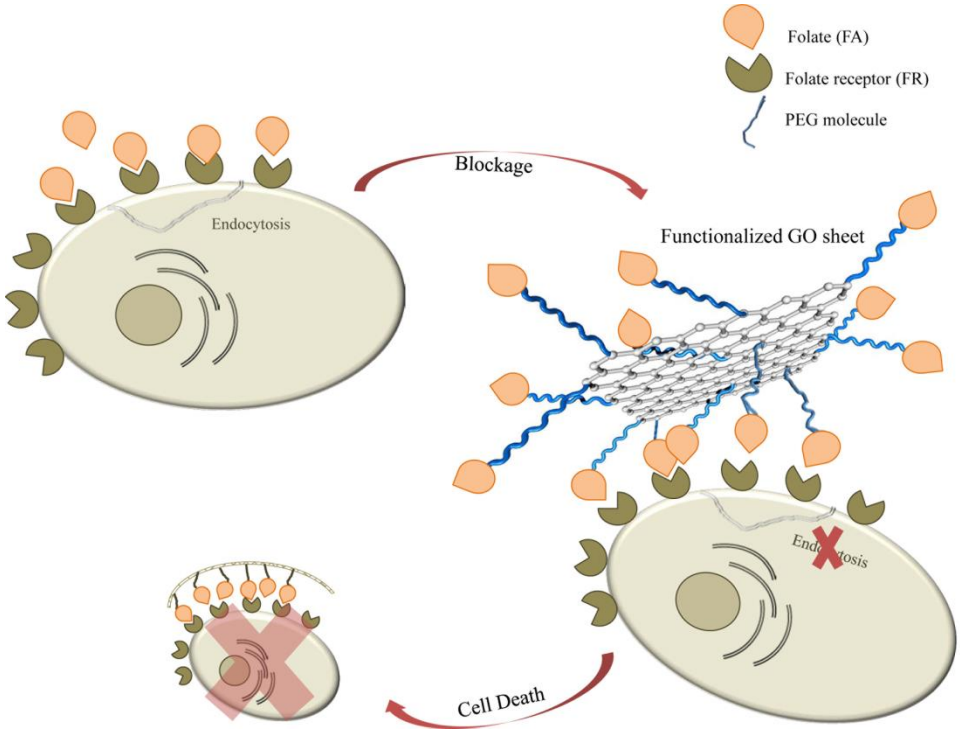

Figure 5-1. Blocking endocytosis on tumour cells by modified GO.

A novel engineered therapeutic system utilizing over-expressed receptors and net-like GO molecule is able to block endocytosis on a tumor cell resulting in metabolic deprivation and death. Individual folate molecules are internalized to the cells while those attached to the GO sheet are blocked by the multiple connections of FR rafts.

5.2 Materials and methods

5.2.1 Materials

GO (4 mg.ml^{-1}), FA, 1-ethyl-3-(3-dimethylaminopropyl) carbodiimide (EDC), 4-Dimethylaminopyridine (DMAP), sodium hydroxide (NaOH), N-hydroxysuccinimide (NHS) and Tris (2-carboxyethyl) phosphine hydrochloride (TCEP) were purchased from Sigma Aldrich. Polyethylene glycol-amine (PEG-amine 5000), and maleimide-polyethylene glycol-amine (Mal-PEG-amine 5000) were purchased from Nanocs. Cyclic RGD was purchased from Peptides International Inc. Fetal calf serum (FCS), 1% L-glutamine, and 1% Penicillin-Streptomycin (Pen-Strep), 1X PBS, Cell Mask Deep red, DMEM (Dulbecco's Modified Eagle Medium) and LHC-9 (Light Hydrocarbon 9) media were purchased from Life Technologies Australia. RPMI-1640 medium, cell counting Kit-8 (WST-8), methotrexate (MTX) and doxorubicin (DOX) were purchased from Sigma Aldrich. PBS solution was used as a vehicle for the materials.

5.2.2 Methods

5.2.2.1 Activation of GO

Specific ligands were covalently coupled to GO polymer via heterobifunctional polyethylene glycol (PEG) linkers using the amine-carboxyl coupling protocol [365]. This linker reduces the steric hindrance between the ligand and receptor [366], and so allows the attached ligand greater freedom of movement and improves the hydrophobicity of the modified polymeric networks.

The functional groups on the GO surface, particularly epoxides can be easily modified to carboxylic acids through ring-opening reactions under strong basic conditions [243]. The carboxylic acids decorating the edges of GO and those newly formed on the planar surface react with the amine group of PEG molecules through an amidation process [365] (Figure 5-2).

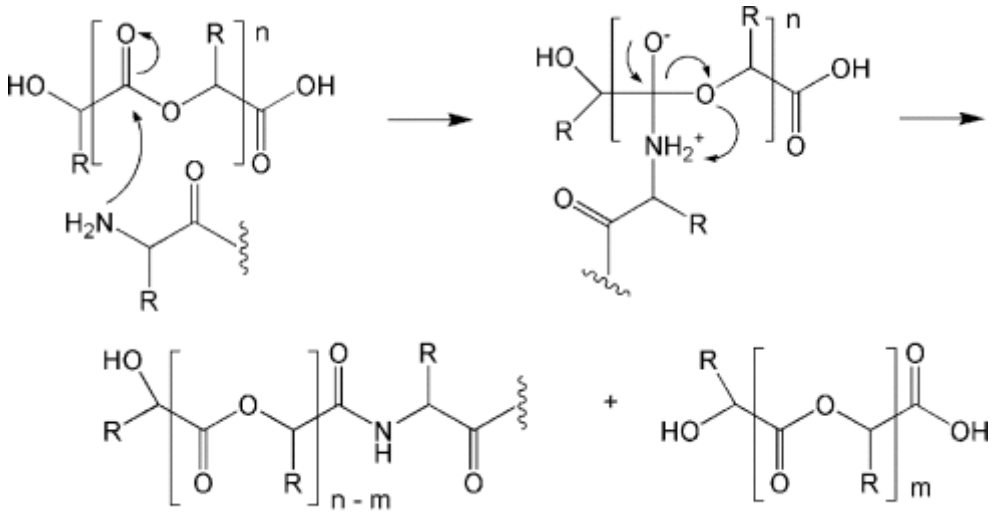

Figure 5-2. Schematic of amidation process.

Amidation involves nucleophilic attack of a primary amine at the α-carbon producing an amide bond.

5.2.2.2 Preparation of PEG-FA

The activated FA (*NHS-FA*) solution [367] was diluted to 5 mg.ml^{-1} in 20 ml water and mixed with an equimolar quantity of PEG-amine (9.06×10^{-4} M; 112.5 mg). Then, equimolar quantities of EDC and 1-2 drops DMAP were added to the mixture of NHS-FA/PEG-amine and was stirred overnight for overnight stirred reaction in the dark. The primary amine group of PEG-amine chemically reacted with the NHS esters (*FA-NHS*) as shown in Figure 5-3.

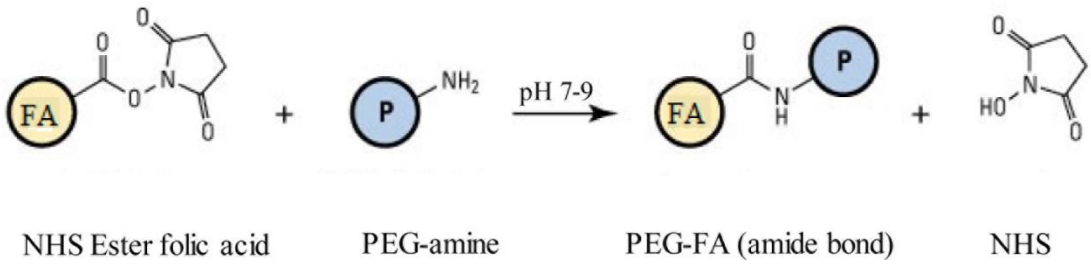

Figure 5-3. . Scheme of NHS reaction with PEG (P)-amine primary amine.

5.2.2.3 Preparation of PEG-RGD

A stock solution of cyclo (Arg-Gly-Asp-D-Phe-Cys) peptide (cyclic RGD) containing Cys amino acid (cRGD-SH) as the reactive functional residue was prepared at 10 mM in PBS. A 0.1 M stock solution of Tris (2-carboxyethyl) phosphine hydrochloride (TCEP, Sigma-Aldrich) was prepared in PBS and neutralised to pH 7.4 with 1M sodium hydroxide. The appropriate amount of this solution (80 nmol) was then mixed with Mal-PEG-amine 5000 using 20 mM TCEP in PBS to reduce any naturally occurring disulphide for 4 hours at 4°C.

UV-visible spectroscopy (UV-Vis) and Fourier transform infrared spectroscopy (FTIR) spectra were used to confirm the accuracy of the chemical reaction by detecting the thioether bond in the prepared RGD-PEG-amine (Figure 5-4).

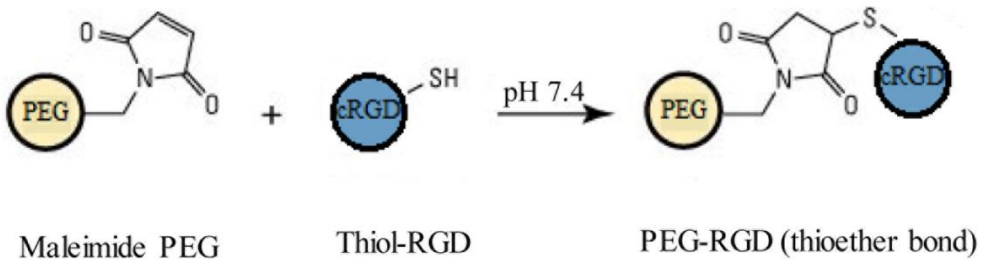

Figure 5-4. Scheme of maleimide reaction with a thiol group producing a thioether bond in the PEG-RGD product.

5.2.2.4 PEGylation and surface functionalisation of GO polymer

To prepare the three GO conjugates, solutions of 2 $mg.ml^{-1}$ FA-PEG-amine (section 5.2.2.2), 2 $mg.ml^{-1}$ RGD-PEG-amine (Section 5.2.2.3), or 1:1 FA-PEG-amine and RGD-PEG-amine (1 $mg.ml^{-1}$ each) were added to separate suspensions of carboxylated GO (GO-COOH, 0.1 $mg.ml^{-1}$; see section 3.4.1 in chapter 3). These mixtures were sonicated for 5 min followed by addition of EDC (0.9 mmol) in the presence of DMAP (0.01 M), sonicated for a further 2 h, then left to react overnight. The final GO networks were denoted as GO-PEGFA, GO-PEGRGD and GO-PEGFARGD. The high concentration of PEG-amine likely increased the degree of PEGylation on the planar GO surface. GO sheets were effectively modified utilising PEG-FA and PEG-RGD to make three different reagents, including two single ligand

(GO-PEGFA, GO-PEGRGD) networks and a dual ligand network (GO-PEGFARGD) (Figure 5-5).

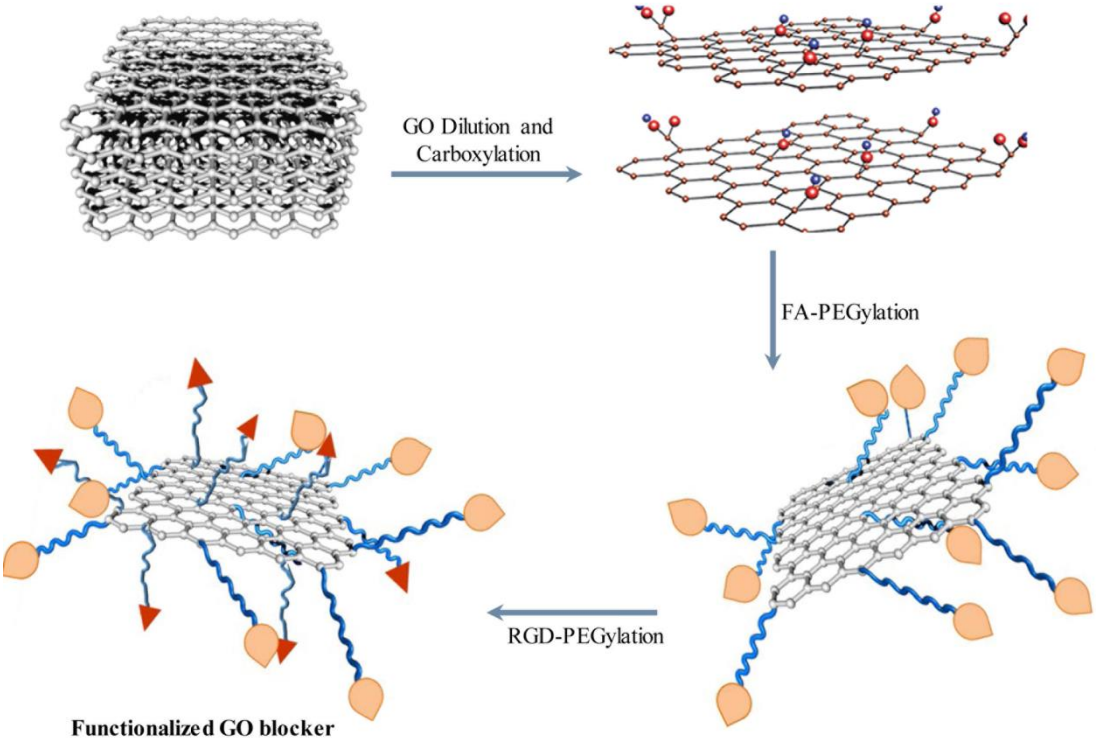

Figure 5-5. Modified GO preparation: GO, GO-COOH, GO-PEGFA and GO-PEGFARGD.

GO sheets were effectively modified utilising PEG-FA and PEG-RGD to make three different reagents, including GO-PEGFA, GO-PEGRGD and GO-PEGFARGD.

The final solutions were then centrifuged using a Beckman Avanti 30 centrifuge at 10,000 g for 30 min to separate the supernatant containing the single PEGylated sheets. The pellet was then suspended in double phosphate buffer saline (PBS; 0.8% NaCl, 0.02% KCl and 0.02 M Na_2HPO_4, pH 7.4) and centrifuged at 10,000 g for 3 h to remove any aggregates or multilayered GO sheets. The resulting supernatants from the two centrifugal steps were then dialyzed against 5 L of distilled water over 72 h to stop the PEGylation reaction and remove unreacted molecules (5 times exchange). The solutions were collected after dialysis, washed several times and filtered each time through a 3 kDa MWCO centrifuge filter (Millipore) at 5000 g for 25

min. The resulting filtrate was lyophilised using freeze dryer (Alpha 1-2 LD plus Freeze Dryer- John Morris) and kept at -20 °C for future use.

PEGylation and surface functionalisation was confirmed by UV-Vis and FTIR (see section 5.3.1) spectra for all three conjugates. The physical and structural properties of the modified GO networks were determined using atomic force microscopy (AFM) and scanning electron microscopy (SEM) imaging, respectively.

5.2.3 Characterization of the modified GO

The modification of the carboxylated GO was confirmed by UV-Vis spectroscopy (UV-visible spectrophotometer/Varian 3E) and Fourier transform infrared spectroscopy (Fourier transform infrared spectroscopy (FTIR) Spectrometer/Varian 7000). Spectra were obtained in an optical range of 400–4000 cm^{-1} by averaging 32 scans at a resolution of $2cm^{-1}$ with one min interval to minimise the effects of dynamic scanning. Atomic force microscopy (Asylum Research Cypher AFM) was used to determine the size and thickness of the modified GO sheets. A proper size of mica (1 cm^2) was prepared and washed with ethanol and water, then dried under a laminar flow to minimise contamination. The mica surface was pre-coated with the positively charged Polyethyleneimine (PEI) for 30 minutes. After rinsing with distilled water and drying under laminar flow, the product was polished by nitrogen gas before adding 10 µl of each sample. Further, to study the morphology of the modified GO sheets dry samples were mounted onto 12mm aluminium stubs with double-sided carbon tabs. The samples were then coated with gold using a Xenosput sputter coater (Dynavac, Wantirna South, Australia) and imaged with the Philips XL30 field-emission scanning electron microscope (Philips, Eindhoven, Netherlands) at a voltage of 2.0 kV and spot size of 2. Thermogravimetric analysis (TGA) measurements were conducted on a Mettler Toledo TGA/SDTA 851e Thermal Gravimetric Analyzer with a heating ramp of 10 °C/min under oxygen and nitrogen flow of 30 mL/min. The interaction of the modified GO sheets with the tumor cells was studied using a TCS SP5 Laser Scanning Microscope (Leica Microsystems) at the Biological Optical Microscopy Platform, University of Melbourne. The microscope imaging chamber was set for standard conditions at 37 °C, 95% humidity and 5% CO_2 for overnight live imaging.

5.2.4 Cell Culture

KB cells (cervix tumour cell line), BEAS-2B cells (transformed epithelial cell line) and human lung fibroblasts were grown to confluence in 75 cm^2 flasks in RPMI-1640, LHC-9 and DMEM media, respectively (each supplemented with 5% FCS, 1% L-glutamine, and 1% Pen-Strep; all from Sigma) at 37 ºC in 5% CO_2 atmosphere at 95-100% humidity. The cells were then plated at a density of $0.5\times10^5 ml^{-1}$ in 96 well plates (NUNC) at a seeding volume of 100 µl/well, whereby some wells were left blank to serve as cell-blank controls. Methotrexate (MTX), a commonly used anti-cancer drug, served as a positive control. After 24 hours of incubation, cells were incubated in incomplete media (media without FCS) for another 24 hours prior to the addition of the GO reagents prepared as described hereafter. The stock solution of modified GO networks was sterilised by UV light exposure for 10 min and diluted to the appropriate concentrations using PBS. Each treatment was added in 10µl to each of triplicate wells in 96 wall plates. After gently mixing the reagent by orbital movement of the plates incubation continued for a further 48 hours.

5.2.4.1 Cytotoxicity studies: the effect of modified GO on various cell lines

Considering the optical properties of GO and its possible light absorption at the same wavelength as the formazan product of the WST reagent (cell counting kit-from Sigma), the toxicity assay was performed by replacing the old media (the cell media that contains the modified GO during 48h incubation) with the fresh media. WST reagent then was added to the plates (10µl/well), with gentle rocking to facilitate mixing followed by a further 3h incubation. The UV-Vis absorbance of the plates was then determined using a microplate reader (Thermo Fisher Scientific). The absorbance of samples was measured at 450 nm (absorbance of the formazan metabolic product of WST produced by viable cells).

5.2.4.2 Synergistic effects

To study the additive/synergistic effects of the modified GO and common chemotherapeutic drugs (MTX and DOX- Figure 5-6), KB cells were incubated with the combination of both modified GO and an anti-cancer drug for 48 h. Toxicity was

assessed using the WST assay. Toxicity was assessed using the WST assay and absorbance measurements as described in section 5.3.4.2.

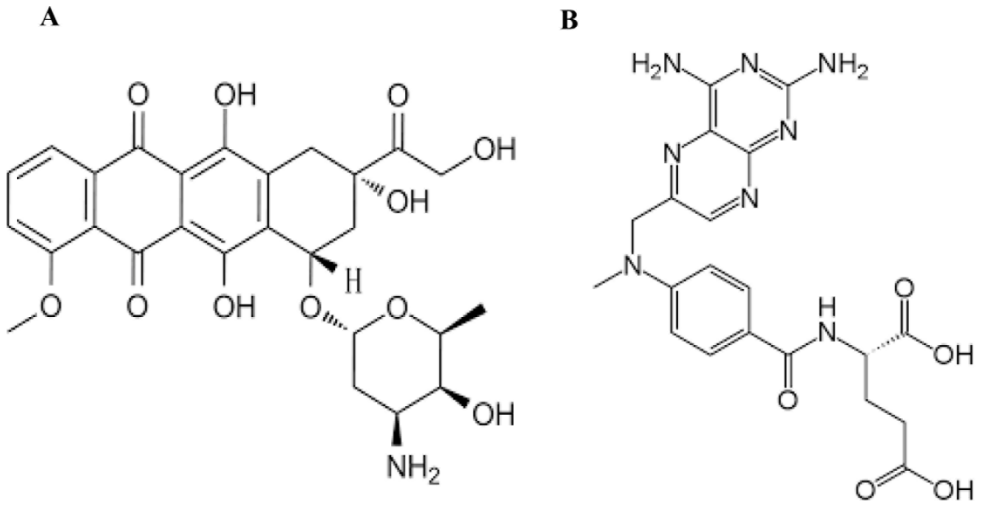

Figure 5-6. Chemical structure of doxorubicin (A) and methotrexate (B).

5.2.4.3 Imaging studies: interactions of modified GO sheets with tumor cells

In order to image cells using confocal microscopy, cells were plated at a density of 3×10^4 ml^{-1} at 37ºC into the "8-well Nunc™ Lab-Tek™ II chambered cover glass slides" (Thermo Fisher Scientific) to form sub-confluent monolayers during an overnight incubation. After serum-deprivation for 24 hours, cells were incubated with the modified GO sheets overnight. The treated cells were then imaged using a TCS SP5 Laser Scanning Microscope (Leica Microsystems, North Ryde, Australia). Fluorescence signals were excited with 488 nm laser and collected between 498 nm - 574 nm using photomuliplier tube (PMT) detector and the transmitted light was simultaneously collected using transmitted PMT. Signals were collected using 40x magnification lens (oil immersion, 1.25 numerical aperture) with digital zoom (2x) and images were taken as 512 x 512 pixels/frame (380nm/pixel). Z-stack images were taken with the same detection settings with higher pixel resolution (108 nm/pixel) and sufficient overlap between frames (690 nm interval) for 3D visualization.

The series of images from sequential focal planes acquired through the samples (Z-stack) were reconstructed as 3D images using Imaris software (Imaris 8.1, Bitplane) [368, 369]. Reconstructing the fluorescence signal to 3 dimensional object is widely

used technique in image quantification [368, 369]. To reconstruct the cells from the background signal, the fluorescence intensity of duplicated channel was inverted and 3D surface was created from inverted channel by automatically thresholding the intensity. 3D surface of sheets were created from the original channel using the intensity threshold and further filtered by volume/intensity.

5.3 Results and Discussion

Modified polymeric networks using GO in a size consistent with diffusion into the tumour, and two different ligands (FA and RGD peptide) have been designed. Upon binding, the reagent would provide a potentially non-permeable shield around the targeted cell by ligand-receptor association with membrane receptors. The resulting large surface area of cellular interaction may also be expected to impede endocytosis and thus limit the availability of the folate and possibly other nutrients to the tumour cells considering the functional role for endocytosis in uptake and rapid translocation of nutrients [370-373].

Indeed, it was investigated whether the combination of the modified GO networks and conventional cytotoxic drugs, such as methotrexate (MTX) and doxorubicin (DOX), shows an additive or synergistic effect [374]. This combination of agents has the potential to reduce the required concentrations of the individual components to achieve the same or higher levels of tumour cell cytotoxicity, thereby reducing the potential for toxic effects related to high doses of the components used individually [375, 376]. Importantly, the combination of various drugs in cancer therapy may delay or prevent the emergence of drug resistance [377]. Using multiple drugs also affects multiple targets and cellular populations, potentially further improving treatment outcomes [374]. Although there are many investigations of polymeric conjugates carrying drugs or previously approved anti-cancer drugs [375, 378-381], to the best knowledge of the thesis author, there is as yet no report on the additive effects of polymeric conjugates with common anti-cancer agents. Study of the application of the modified GO sheets with conventional anti-cancer drugs may reveal new directions for cancer therapy.

5.3.1 Characterization of modified GO

5.3.1.1 Characterisation of GO-PEGFA

5.3.1.1.1 Chemistry

UV-Vis spectroscopy was used to confirm that PEG-FA was conjugated to GO-COOH (Figure 5-7). The peaks at around 280 nm and 350 nm in the spectrum of PEG-FA were attributed to the specific absorbance peak of FA [382]. However, GO-PEG-FA showed a strong peak at 275 nm. This shift for the FA derivatives after GO conjugation may be due to the chemical interaction of the GO and PEG-FA components [383]. Moreover, the observed small shoulder around 225 nm in PEG-FA transferred to around 230 nm after GO conjugation due to the chemical attachment of the two molecules.

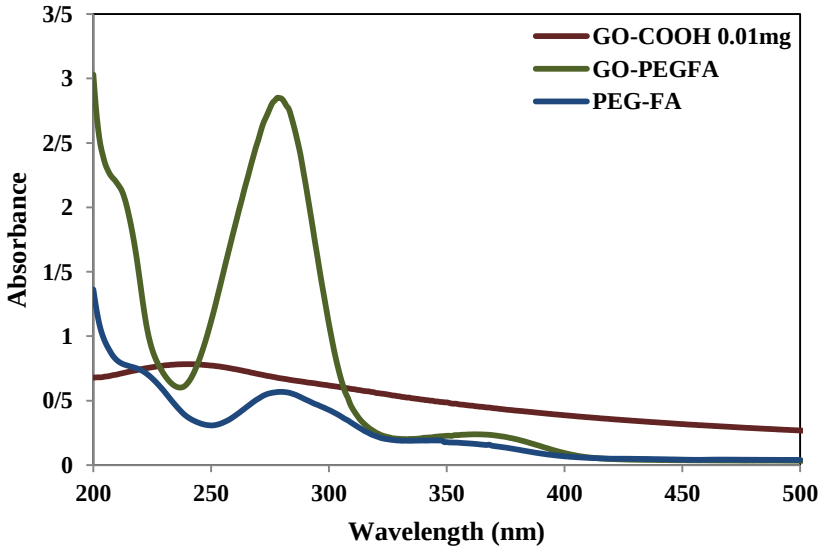

Figure 5-7. UV-Vis spectra of GO-COOH, PEG-FA and GO-PEGFA.

The peaks at around 280 nm and 350 nm in the spectrum of PEG-FA are attributed to the specific absorbance peak of FA. However, GO-PEG-FA showed a strong peak at 275 nm due to the chemical interaction of the GO and PEG-FA components.

The conjugation of PEG-FA on carboxylated GO was further characterised by FTIR spectroscopy (Figure 5-8) The peaks at 1400 to 1700 cm^{-1} corresponded to NH-CO stretching of the amide bonds in PEG-FA and GO-PEGFA [384] , while the region 1100 to 1200 cm^{-1} represented CO stretching in all three structures. The peaks around

2900 and 1100 cm^{-1} corresponded to the C–H out of-plane bending vibrations of PEG [385], whereas the broad peak from 3000cm^{-1} to 3600 cm^{-1} was attributed to O-H stretching in GO polymer [385, 386]. All of the peaks for the C–H of PEG and the characteristic peaks of FA were slightly shifted after the PEG-FA and GO conjugation, which suggested that PEG-FA was successfully conjugated to GO, and agreed with the UV-Vis results.

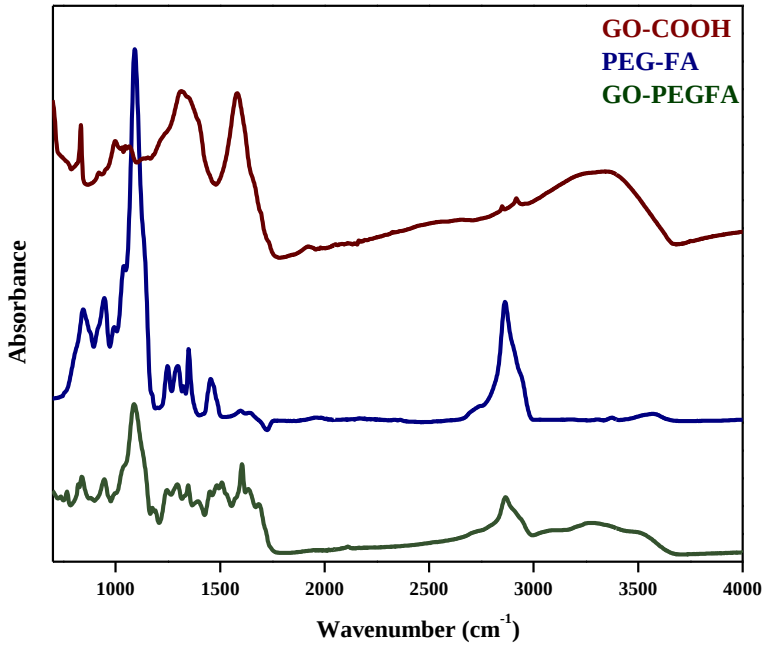

Figure 5-8. FTIR spectra of GO-COOH, PEG-FA and GO-PEG-FA.

All of the peaks for the C–H of PEG and the characteristic peaks of FA are slightly shifted after the PEG-FA and GO conjugation, which suggested that PEG-FA was successfully conjugated to GO.

5.3.1.1.2 Size and thickness

The effective grafting of PEG-FA molecules to GO-COOH was also confirmed by visualising the physical features of the functionalised GO sheets using AFM (Figure 5-9) As shown in this figure, the GO-COOH sheets were approximately 1.2 nm thick (Figure 5-9B), compared to the GO-PEGFA sheets with an average thickness of 5.0 nm after PEG-FA conjugation (Figure 5-9D). Together, the measured thickness and its rough surface confirmed the existence of PEG-FA chains across the GO-COOH sheet [387, 388]. Additionally, the size of GO-PEGFA sheets ranged from

200 to 600 nm (Figure 9C and D). Sheet size could be affected by the chemical functionalisation process and the following sonication steps [389].

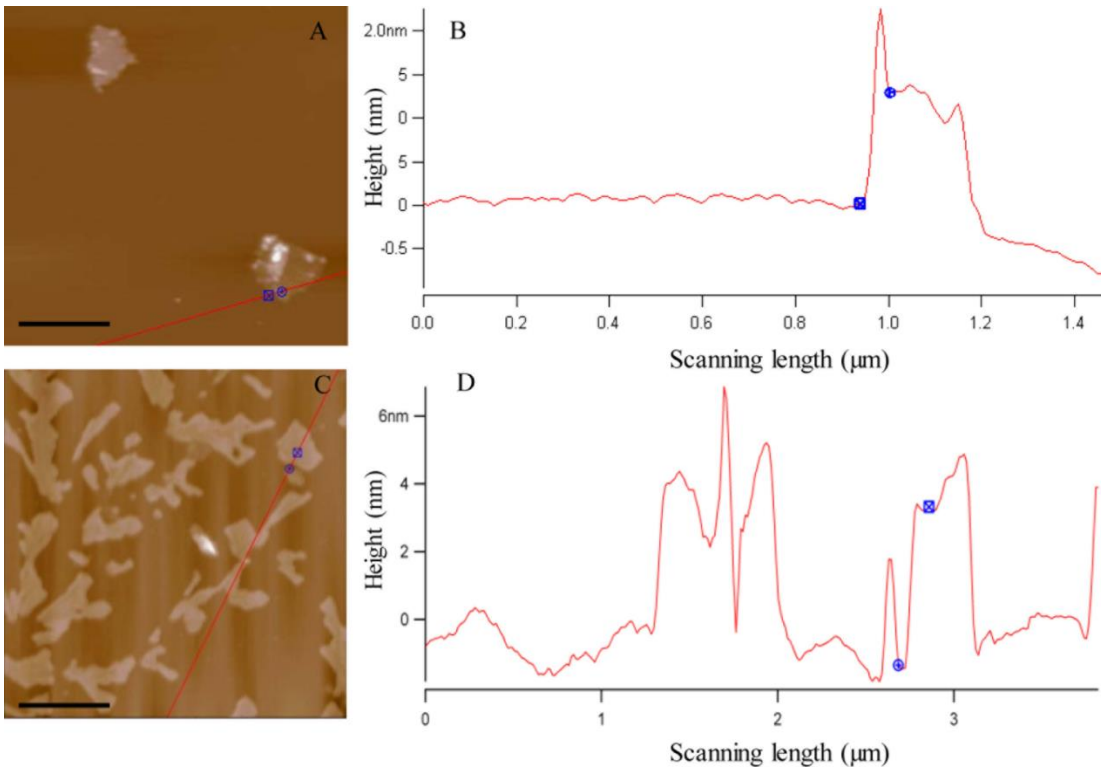

Figure 5-9. AFM images of CO-COOH and GO-PEGFA.

Tapping mode AFM images (left column) with section analysis (right column) of (A, B) GO-COOH and (C, D) GO-PEGFA. GO-COOH sheets are approximately 1.2 nm thick compared to the GO-PEGFA sheets with an average thickness of 5.0 nm after PEG-FA conjugation. (Scale bar: 500 nm)

The functionalised GO sheets were also imaged under SEM to see their 3D physical features (Figure 5-10). The particles had a plate-like shape with a flaky, layered microstructure, which resulted from thick multilayer stacks formed when lyophilised.

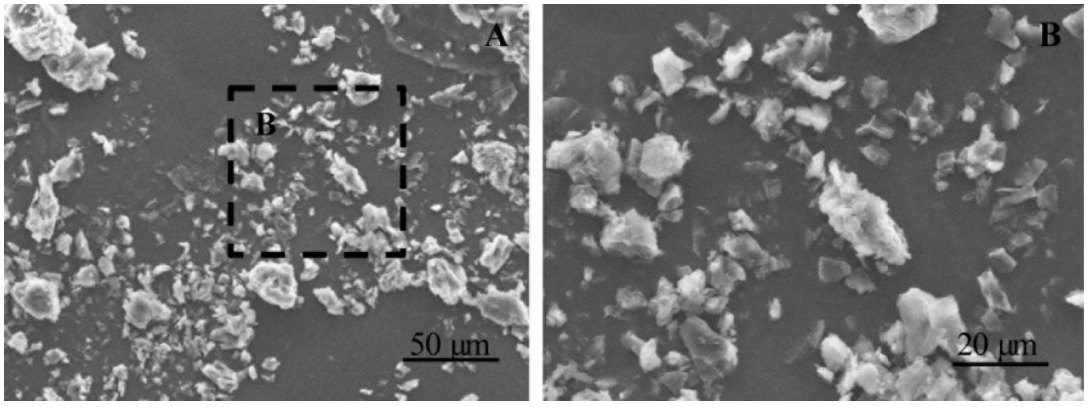

Figure 5-10. SEM images of GO-PEGFA.

(A) Very low and (B) low magnification of the region marked in (A) show a plate-like shape with a flaky, layered microstructure.

5.3.1.1.3 PEGylation yield

The thermal stability of GO-COOH, PEG-FA and GO-PEGFA was analysed by TGA (Figure 5-11). As shown by arrows, three main degradation temperatures were observed for GO-COOH, around 50 °C, 200 °C, and 430 ºC. The approximately 20% loss of mass from ambient temperature to almost 170 ºC could be due to evaporation of trapped water molecules between the carboxylated GO layers [328]. Thereafter, GO-COOH was almost stable to 420 °C and only began to degrade in the range of 420 ºC to 800 ºC with 80 % mass loss [329]. By contrast, the decomposition of PEGylated molecules, i.e. GO-PEGFA and PEG-FA, initiated from 380 ºC (approximately 10% mass loss) and 550 ºC (approximately 30% mass loss), respectively, due to the thermal decomposition of the PEG fragment. PEGylated GO showed more thermal stability without any significant further mass loss. Hence, the thermal stability of GO-COOH was improved with PEGylation. The T10 (as measured at the point of 10% mass loss) has increased from 170 to 380 ºC by PEGylation [390]. According to this result, a 70% increase in thermal stability of GO-COOH by PEGylation indicates a nearly 70% PEGylation yield in the GO-COOH networks.

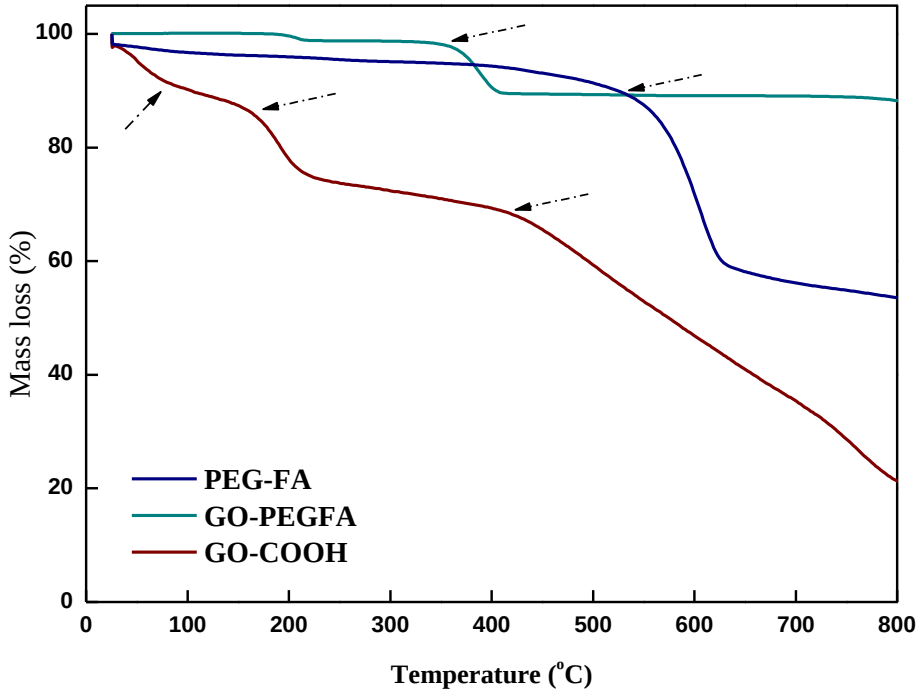

Figure 5-11. TGA curves of GO-COOH, PEG-FA and GO-PEGFA.

Three main degradation temperatures were observed for GO-COOH, around 50 °C, 200 °C, and 430 ºC, while the decomposition of PEGylated molecules, initiated from 380 ºC (approximately 10% mass loss) and 550 ºC (approximately 30% mass loss).

5.3.2 Characterisation of GO-PEGRGD network

5.3.2.1 Chemistry

As in section 5.3.1.1, UV-Vis spectroscopy was used to confirm that PEG-RGD was conjugated to GO-COOH (Figure 5-12). The peaks at around 275 nm in the spectrum of PEG-RGD were attributed to the specific absorbance peak of RGD, which manifested as a strong peak at 280 nm for GO-PEGRGD [391]. This shift may be due to the chemical interaction of GO and PEG-RGD. The observed peak at around 230 nm in GO [392] was also transferred a bit, forming a peak at 225 nm after PEG-RGD conjugation due to the chemical attachment of the two molecules.

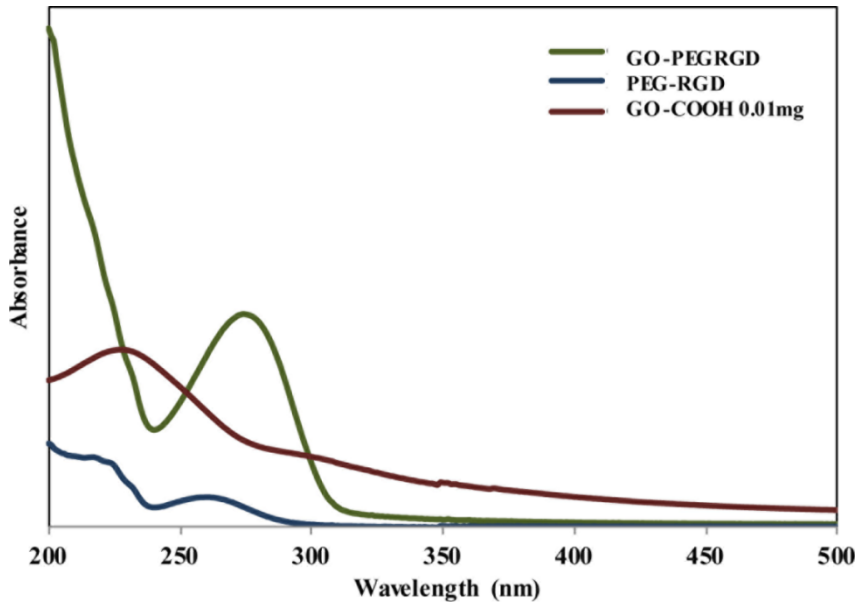

Figure 5-12. UV-Vis spectra of GO-COOH, PEG-RGD and GO-PEGRGD.

The peaks at around 275 nm in the spectrum of PEG-RGD are attributed to the specific absorbance peak of RGD, which manifested as a strong peak at 280 nm for GO-PEGRGD.

The presence of different types of oxygen-containing groups in GO was previously confirmed by FTIR (Figure 3-10), by the broad peak at the range of 3000-3600 cm^{-1} (O-H stretching vibrations), 1750 cm^{-1} (stretching vibrations from C=O), 1250 cm^{-1} (C-OH stretching vibrations) and 1070-1100 cm^{-1} (C-O stretching vibrations), as reported earlier [324, 325]. O-H stretching (2400-3400 cm^{-1}) [393], C=O stretching (1700-1730 cm^{-1}) [394] were assigned to COOH groups, which was further confirmed by the CH_2-stretching vibrations at 2850 and 2920 cm^{-1} (lower peaks) [395]. After functionalisation of GO-COOH by PEG-RGD, the intensities of the absorption peaks corresponding to oxygen functional groups decreased. This clearly confirmed the removal of oxygen-containing groups by formation of amide bonds during the functionalisation [396]. The existence of an amide bond was shown by detecting N-H stretching (2800-3600 cm^{-1}), N-H bending (1500-1650 cm^{-1}), C-N (alkyl) stretching (1025-1200 cm^{-1}), NH-CO stretching (1500-1700 cm^{-1}), and CO-O stretching (1700-1750 cm^{-1}) in the final GO-PEGRGD product [395] (Figure 5-13).

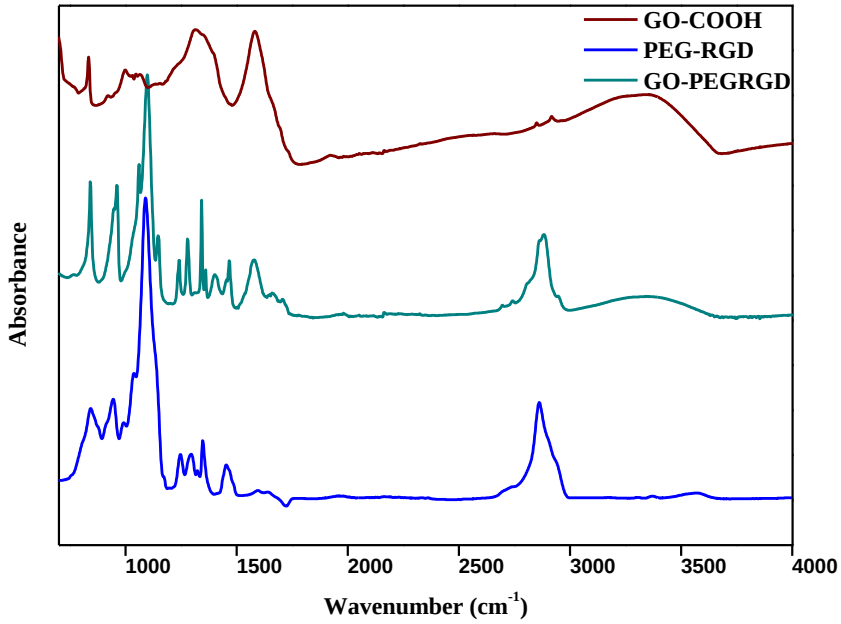

Figure 5-13. FTIR spectra of GO-COOH, PEG-RGD and GO-PEGRGD.

After functionalisation of GO-COOH by PEG-RGD, the intensities of the absorption peaks corresponding to oxygen functional groups decreased. This clearly confirms the removal of oxygen-containing groups by formation of amide bonds during the modification.

5.3.2.2 Size and Thickness

The effective grafting of PEG-RGD molecules on GO-COOH was also confirmed using AFM. Figure 5-14 indicates that the GO-PEGRGD networks had an average thickness of 6.0 nm after PEG-RGD conjugation, which was much higher than for GO-COOH at approximately 1.2 nm (Figure 5-9B). The measured thickness and rough surface confirmed the existence of PEG-RGD chains across the GO-COOH sheets [387, 388], which ranged in size from 200 to 500 nm.

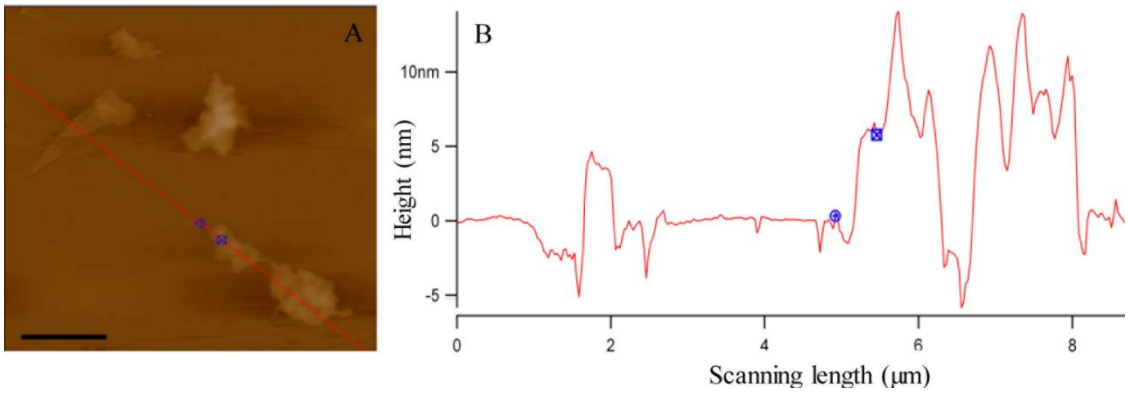

Figure 5-14. AFM image of GO-PEGRGD.

Tapping mode AFM image (A) and section analysis of GO-PEGRGD (B). The GO-PEGRGD networks have an average thickness of 6.0 nm after PEG-RGD conjugation, which is much higher than for GO-COOH at approximately 1.2 nm. (Scale bar: 500 nm.)

SEM observation of GO-PEGRGD showed a flexible, 3D sheet-like structure (Figure 5-15), different to GO-PEGFA (Figure 5-9). SEM also revealed the layered microstructure of the modified GO sheets, which contained dense multilayer stacks produced when the product was freeze-dried as powder.

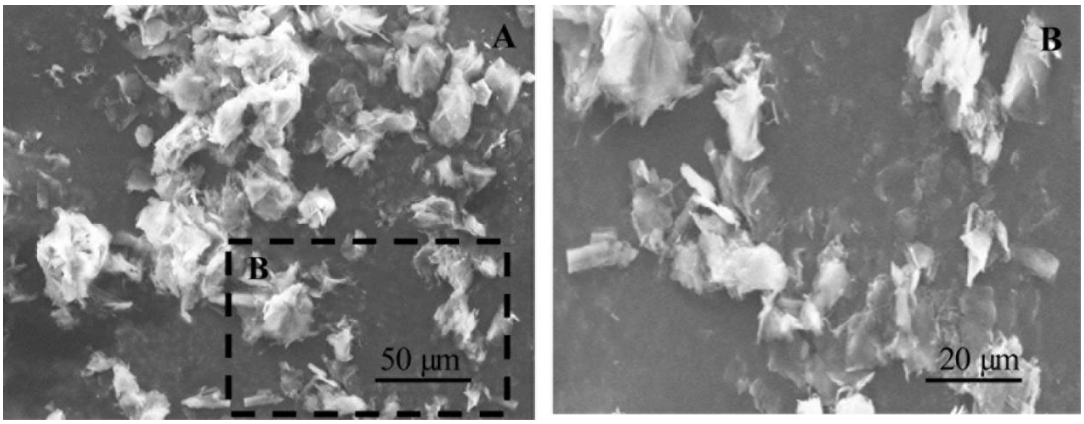

Figure 5-15. SEM images of GO-PEGRGD.

(A) Very low and (B) low magnification of the region marked in (A) show a flexible, 3D sheet-like structure different to GO-PEGFA (Figure 5-9).

5.3.2.3 PEGylation yield

The thermal stability of PEG-RGD and GO-PEGRGD was analysed by TGA technique (Figure 5-16). The decomposition of GO-COOH was explained in section 5.3.1.1.3. In common with PEG-FA, the PEG-RGD molecule seems to be more stable as its decomposition only starts at 380 ºC. It was evident that T10 (as measured at the point of 10% mass loss) of GO-PEGRGD was higher than for GO-COOH but lower compared to PEG-RGD. This may be due to the chemical reduction effect of PEG on the GO-COOH, and the oxidation effect of GO-COOH on RGD-PEG once they are conjugated. The decomposition temperature T50 (as measured at the point of 50% weight loss) was higher in PEG-RGD, which made GO-COOH much more stable after PEGylation, and without any further mass loss when temperature increased to 380 °C. Compared with the thermal decomposition behaviour of neat GO-COOH, GO-PEGRGD had a higher T10 temperature, with the delay in decomposition indicating the higher thermal stability of the PEGylated polymer; T10 was increased from 170 ºC to 380 ºC by PEGylation. According to this result, the 60% increase in thermal stability of the GO-COOH by PEGylation indicates around a 60% PEGylation yield in the GO-COOH networks. The GO-PEGRGD composite was thermally stable below 380 ºC and had only reduced in mass by 30% when heated to 600 ºC.

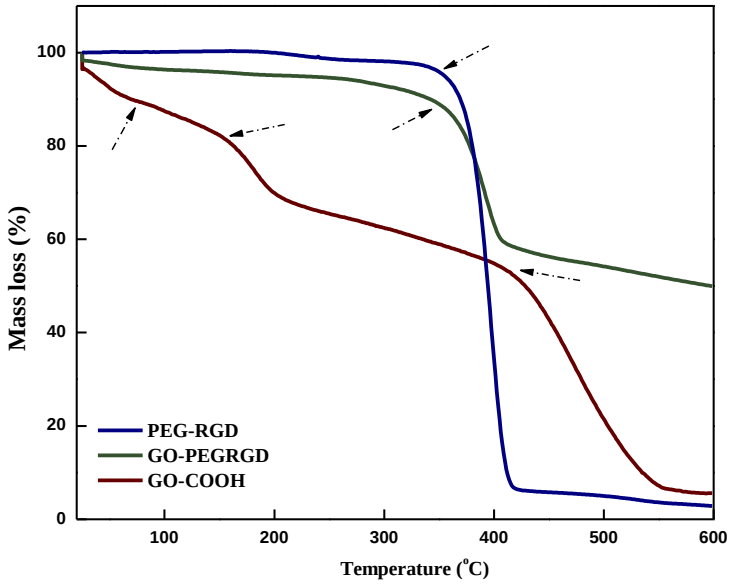

Figure 5-16. TGA curves of GO-COOH, PEG-RGD and GO-PEGRGD.

Three main degradation temperatures are observed for GO-COOH, around 50 °C, 200 °C, and 430 ºC, while the decomposition of PEGylated molecules started at 380 ºC. It is evident that T10 (as measured at the point of 10% mass loss) of GO-PEGRGD was higher than for GO-COOH but lower compared to PEG-RGD.

5.3.3 Characterisation of GO-PEGFARGD network

5.3.3.1 Chemistry

UV-Vis spectroscopy was used to confirm that both PEG-RGD and PEG-FA were conjugated to GO-COOH (Figure 5-17). The peak around 280 nm in GO-PEGFARGD is the common absorbance peak of PEG-RGD [391], while the peak at 370 nm was assigned to PEG-FA [382]. The shift from 280 nm to 275 nm after GO conjugation may be due to the chemical interaction of GO and the PEG-FA and PEG/RGD components. Given that, the spectrum of GO-PEG-FARGD had common elements of the spectra of GO-PEGFA and GO-PEGRGD and yet was distinct, confirmed that the final product had dual ligands.

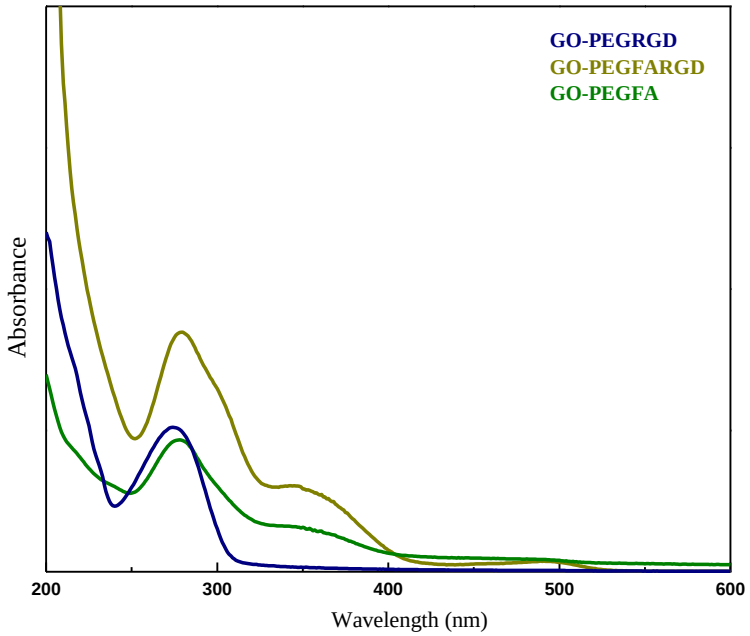

Figure 5-17. UV-Vis spectra of GO-PEGFA, GO-PEGRGD and GO-PEGFARGD.

The peak around 280 nm in GO-PEGFARGD is the common absorbance peak of PEG-RGD, while the peak at 370 nm is assigned to PEG-FA. The shift from 280 nm to 275 nm after GO conjugation is due to the chemical interaction of GO and the PEG-FA and PEG/RGD.

The existence of an amide bond in GO-PEG-FARGD was indicated by N-H stretching (2800 cm^{-1}), N-H bending (1500-1650 cm^{-1}), C-N (alkyl) stretching (1025-1200 cm^{-1}) and NH-CO stretching (1600 cm^{-1}) [395] , that together confirmed the successful conjugation of PEG-FA and PEG-RGD to GO-COOH (Figure 5-18).

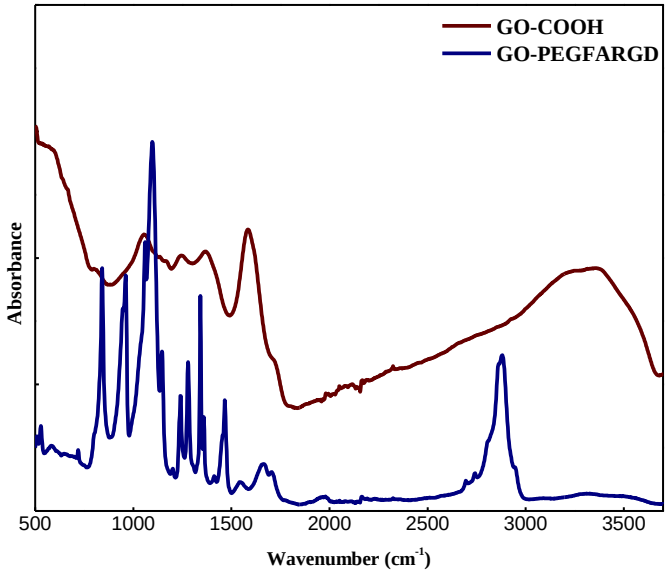

Figure 5-18. FTIR spectra of GO-COOH and GO-PEGFARGD.

The existence of an amide bond in GO-PEG-FARGD is indicated by N-H stretching (2800 cm^{-1}), N-H bending (1500-1650 cm^{-1}), C-N (alkyl) stretching (1025-1200 cm^{-1}), NH-CO stretching (1600 cm^{-1}).

5.3.3.2 Size and thickness

The effective grafting of PEG-FA and PEG-RGD molecules for dual ligand modified GO (GO-PEGFARGD) was assessed by visualizing the physical features of the functionalised GO sheets using AFM (Figure 5-19). GO-PEGFARGD had an average thickness of 6.0 nm, similar to GO-PEGRGD (Figure 5-14B). The measured thickness, compared with that of GO (1.2 nm, Figure 5-9B), and the rough surface were evidence of the existence of PEG chains across the GO sheets. Figure 5-19B also shows that the longest axis of the modified GO sheets ranged from 200 nm to 600 nm. The size could be induced by the surface modification and sonication steps [389].

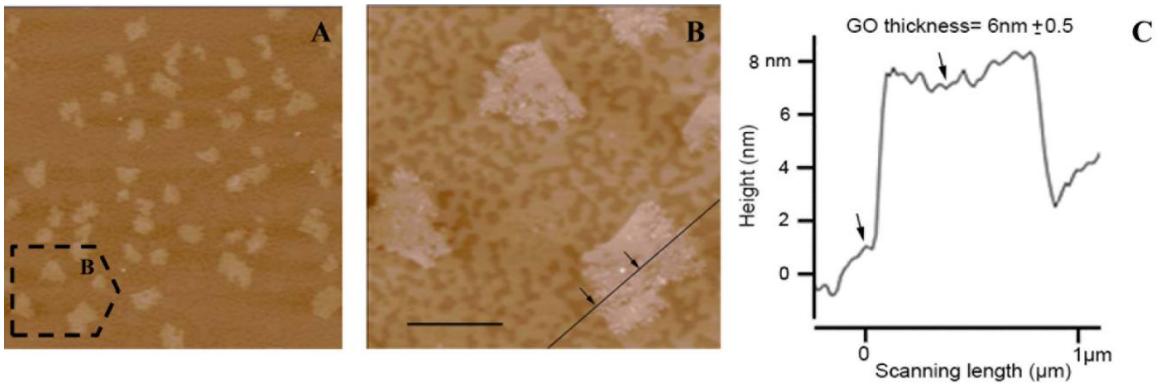

Figure 5-19. Tapping mode AFM images.

(A) low magnification and (B) higher magnification of the region marked in (A), and (C) height profile of the GO-PEGFARGD shows the average thickness of 6.0 nm, similar to GO-PEGRGD. (Scale bar: 500 nm)

GO-PEGFARGD was also visualised by SEM (Figure 5-20). This network appeared to be porous, and at low magnification somewhat fluffy, compared to GO-PEGFA and GO-PEGRGD which showed a flexible, plate-like shape with a flaky, layered microstructure (Figures 5-10B and 5-15B, respectively). Considering the spongy structure of this dual ligand modified GO, it might be potentially suitable for the loading and targeted delivery of anticancer drugs [397], e.g. DOX or MTX, or a diagnostic compound.

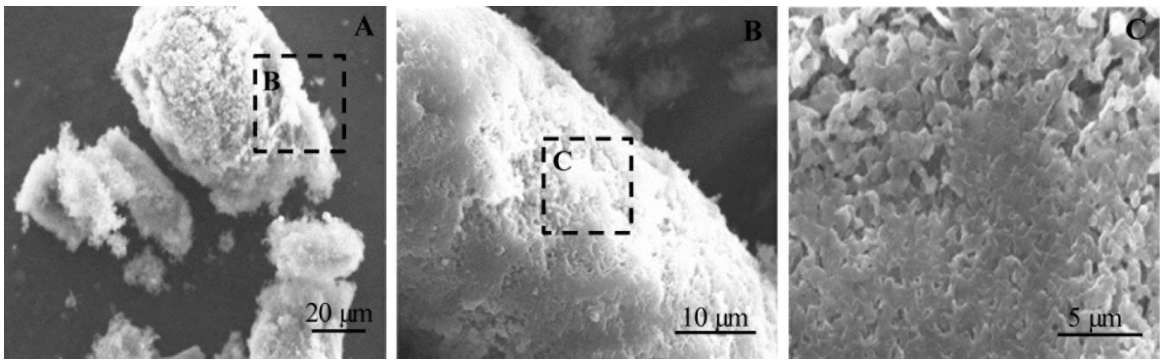

Figure 5-20. SEM images of GO-PEGFARGD.

(A) low, (B) moderate and (C) high magnifications of selected areas shows the porous and fluffy structure, compared to GO-PEGFA and GO-PEGRGD with a flexible, plate-like and layered microstructure (Figures 5-10B and 5-15B, respectively).

5.3.4 Cell studies

5.3.4.1 Toxicity effects

To study the cytotoxicity of modified GO sheets, specifically GO-PEGFA, the concentration-dependence of KB cell responses was examined after 48 h of exposure (Figure 5-21). Based on the formation of the WST formazan reaction product, the cell viability reduced by 30% when the concentration of the modified GO sheets was increased up to 1.3 $mg.ml^{-1}$. However, at higher concentrations (up to 10 $mg.ml^{-1}$) the less cytotoxicity was observed. This bell-shaped concentration response curve may be due to the aggregation of GO sheets at higher concentration, effectively hampering the ligand-receptor interaction with cell surface.

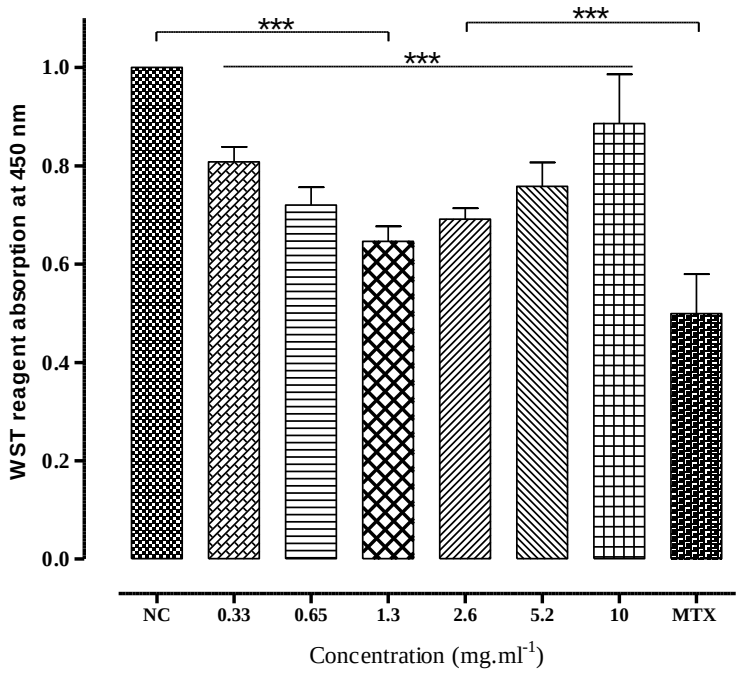

Figure 5-21. Viability of KB cells after 48 hours exposure to increasing concentrations of the modified GO sheets.

The vertical axis represents the cell viability measured by the absorbance of WST reagent at 450 nm; MTX (1×10^{-4} M) was used as the positive control, whereas NC shows the negative control which has not exposed to the reagents. Values are mean ± sem from four independent experiments. Triplicate incubations for each treatment were conducted in each independent experiment. P values were calculated using one-way ANOVA test (***$P < 0.0001$).

The cytotoxicity of the modified GO networks (GO-PEG-RGD, GO-PEG-FA and GO-PEG-FARGD) was measured after 48 hours incubation (Figure 5-22).

BEAS-2B cells (transformed primary cell line) are considered suitable to screen chemical and biological agents for differentiation and/or carcinogenesis effects [398]). This non- tumorigenic transformed cell line was used to examine the cytotoxicity of the modified GO sheets after 48 hours incubation (Figure 5-22A). The viability of BEAS-2B cells was decreased by 20%, while the positive control (MTX) decreased cell viability by 45%. The constitutive proliferation of BEAS-2B cell line, which makes its behaviour similar to tumour cells, may be reduced by exposure to the modified GO networks resulting in a decrease of the WST reaction product. The FA-modified GO reduced KB cell viability as a tumour cell line by 30%, with RGD and FARGD-modified GO showing similar reductions (35%) in cell viability (Figure 5-22B). Compared to the maximum effect of MTX (50% reduction in cell viability), the level of observed cytotoxicity for the modified GO networks provided encouragement for further investigation.

Lung fibroblasts were used as a primary human cell line to provide some initial insight into the potential for selective cytotoxicity of the modified GO sheets (Figure 5-22C). The modified GO did not significantly affect WST product formation in this non-tumour primary cell line. Notably, due to the time restriction, fibroblasts (a non-tumorigenic cell line) were studied for a fewer number of experiments.

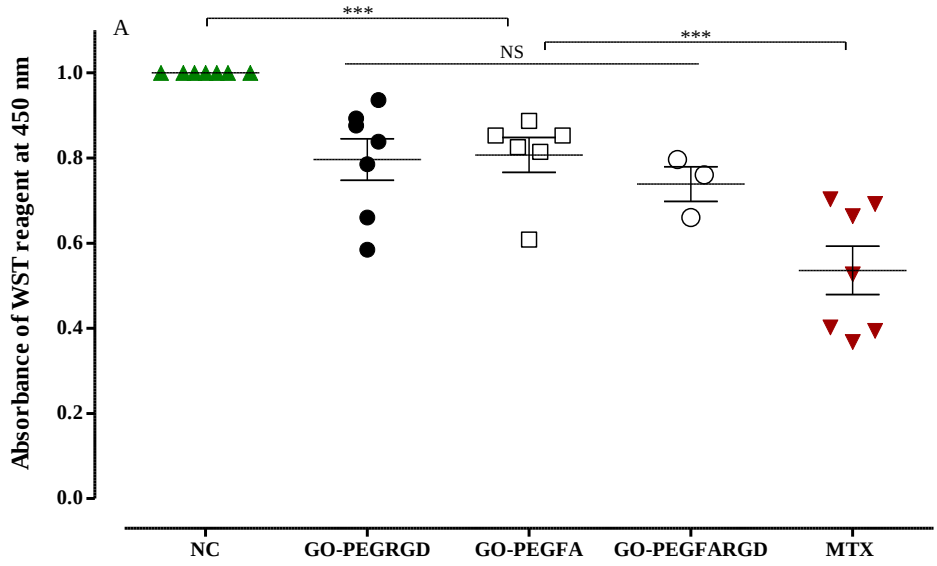

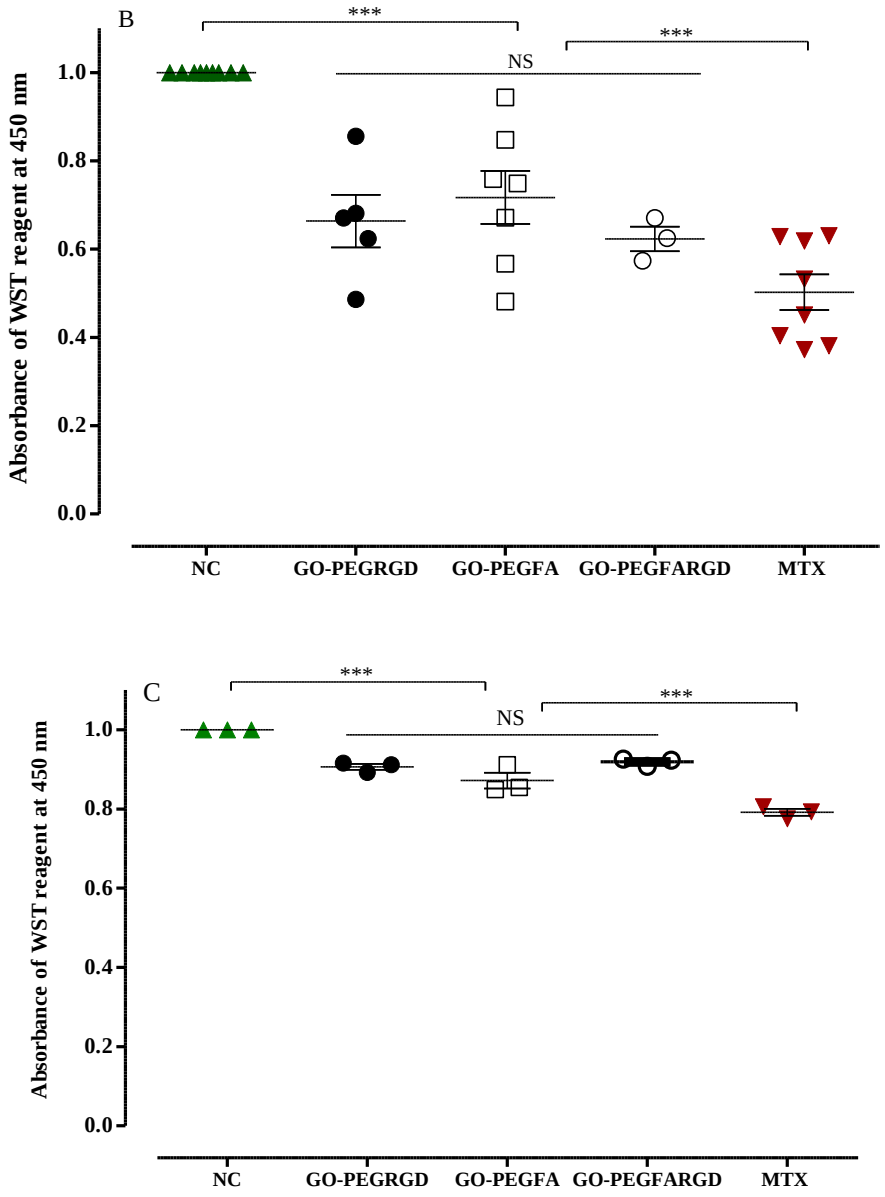

Figure 5-22. Viability of KB cells, BEAS-2B cells and Fibroblasts.

Viability of (A) BEAS-2B cells, (B) KB cells and (C) Fiboblastsr after 48 h exposure to 1.3 mg.ml^{-1} of GO-PEGRGD, GO-PEGFA and GO-PEGFARGD. The vertical axis represents the cell viability measured by the absorbance of WST reagent at 450 nm; MTX (1×10^{-4} M) was used as the positive control, whereas NC shows the negative control which has not exposed to the reagents. Values are mean ± sem from three independent experiments. Triplicate incubations for each treatment were conducted in each independent experiment. P values were calculated using one-way ANOVA test (***P < 0.0001, NS: Not significant). Due to the time restriction, fibroblasts (a non-turmeric cell line) were studied for a fewer number of experiments.

The differential effect of MTX and the modified GO on the three different cell lines may be due to differences in proliferation rates. Tumour and transformed cell lines typically show a higher fraction of cells in cell cycle due to their higher proliferation rate, which increases their sensitivity to the MTX, as well as to the ligand modified GO. Less proliferative cell types are relatively resistant to the MTX and modified GO sheets, since a lower fraction of cells are cycling reducing the requirement for cellular metabolism and nucleic acid synthesis [399, 400].

To better understand the cell responses over the incubation time, the KB cell growth was monitored up to 48 h after treatment by single ligand modified GO sheets. The viability of the KB cells was examined using the WST reagent (Figure 5-23). The toxicity effects of modified GO sheets compared to non-treated cells (NC) is evident. The highest cytotoxicity effect was observed within the first 7 h of exposure whereby the cell viability was decreased by 50 %. As ongoing cell proliferation is slow, the WST reagent showed only 20% reduction in negative control for the first 20 h, while the incubated GO sheets reduced cell viability to around 50% for the same period. Indeed, for the first 20 h the treated KB cell viability tracked the anticancer MTX for both single ligand GO conjugates. Then in just 8 h the cells roughly stabilised at around 60% viability for the remainder of the experiment.

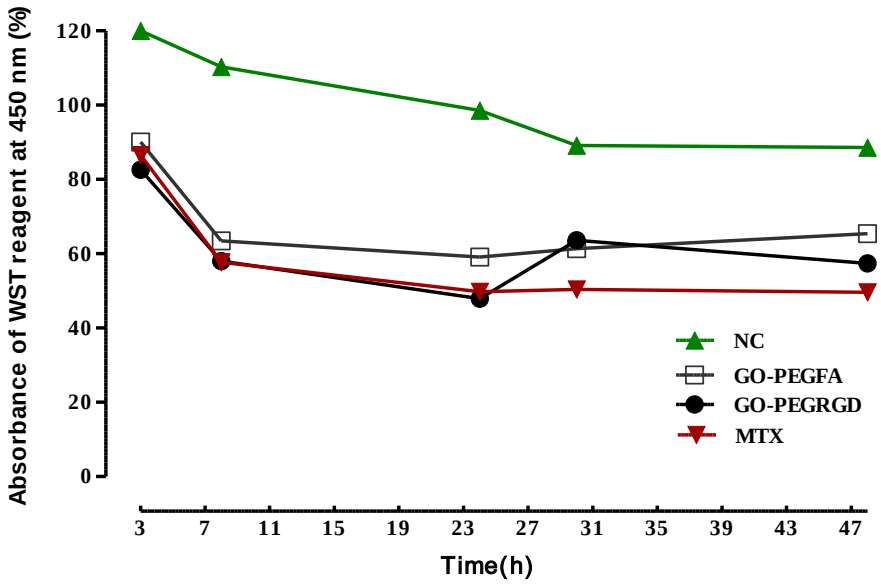

Figure 5-23. Viability of KB cells with time up to 48 h exposure to 1.3 mg.ml^{-1} of GO-PEG-FA and GO-PEGRGD.

Vertical axis represents the cell viability measured by the absorbance of WST reagent at 450 nm (%); MTX (1×10^{-4} M) was used as the positive control; in the negative control (NC) the cells were not exposed to modified GO. The vertical axis and error bars represent means ± sem of cell viability from 4 independent experiments. Triplicate incubations for each treatment were conducted in each independent experiment.

5.3.4.2 Synergistic effects

The combinations of single ligand modified GO with anti-cancer agents MTX or DOX appeared to be more effective than individual toxic drugs or GO sample (Figure 5-24). Looking at the literature, the maximum cytotoxicity of MTX and DOX (50% reduction in cell viability) was observed at the particular concentrations of 10^{-6} M [401] and 10^{-7} M [402, 403] respectively and the concentration response relationship for both MTX and DOX were similar across the different tumor cell lines [401, 404, 405]. Our results confirmed that the viability of KB cells was reduced by 50% at the optimum concentration of 10^{-4} M of MTX [406] and 10^{-5}M of DOX [407]. However, when MTX (10^{-4} M) was co-incubated with modified GO-PEGFA or GO-PEGRGD sheets (1.3 mg ml^{-1}), the cytotoxicity towards the KB cancer cell lines improved markedly to 80% (Figure 5-24A). The combinations of GO-PEGFA or GO-PEGRGD with DOX (10^{-5}M) also showed higher cytotoxicity towards the KB cancer cell lines 65% compared to each

individual component (Figure 5-24B). Given these observations, there is a considerable synergy between the modified GO sheets and the examined anti-cancer drugs in which the cytotoxic effect was significantly increased by using GO sheets and drugs in combination.

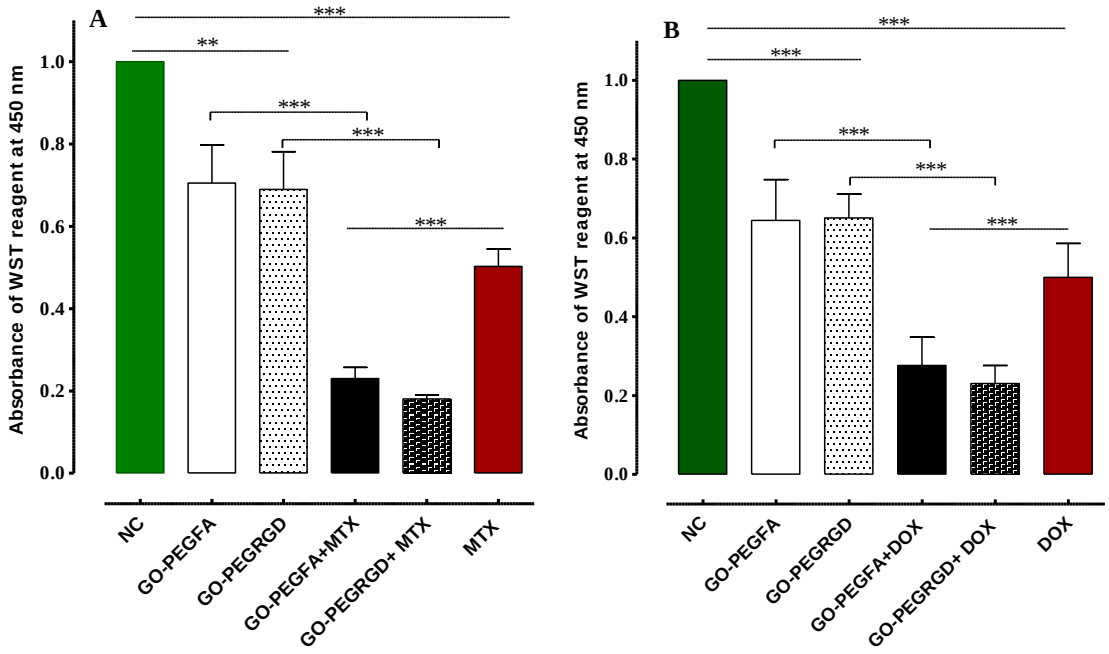

Figure 5-24. The combinations of single ligand modified GO with anti-cancer agents MTX or DOX.

Viability of KB cells after 48 h exposure to 1.3 mg.ml^{-1} of GO-PEGFA or GO-PEGRGD and their combination with (A) MTX (1×10^{-4} M) and (B) DOX (1×10^{-5} M). Straight MTX and DOX were used as positive controls, whereas NC stands for negative control with no reagent. (n=4) Values are mean ± sem from four independent experiments. Triplicate incubations for each treatment were conducted in each independent experiment.

5.3.4.3 Confocal microscopy imaging

In order to understand this synergistic effects between the modified GO and DOX/MTX, the cellular interaction between the modified GO and the cancer lines was investigated using confocal life imaging at 10-minute intervals. GO and its derivatives exhibit auto-fluorescence over a wide range of emission wavelengths [336, 408]. This

fluorescence enables the cellular interactions and potential biological effects to be studied without staining the cells [409].

The series of images from sequential focal planes acquired through the samples (Z-stack) interpreted using Imaris software (Imaris 8.1, Bitplane) [368, 369], show the location of GO sheets either at the cell membrane or intracellular. In order to ascertain whether or not the FA-modified GO sheets were located in the intracellular compartment, sequential focal planes were acquired through the selected area and converted into a Z-stack. Following 16 h incubation of KB cells with different reagents (GO-PEGFA, GO-PEGRGD and GO-PEG-FARGD), GO-PEGFA sheets were observed to be inside the cells (Figure 5-25A). The series of images from different focal planes (Z-stack) was acquired through the selected area to determine the location of GO sheets within cellular structure in 3 dimension (Figure 5-25B).

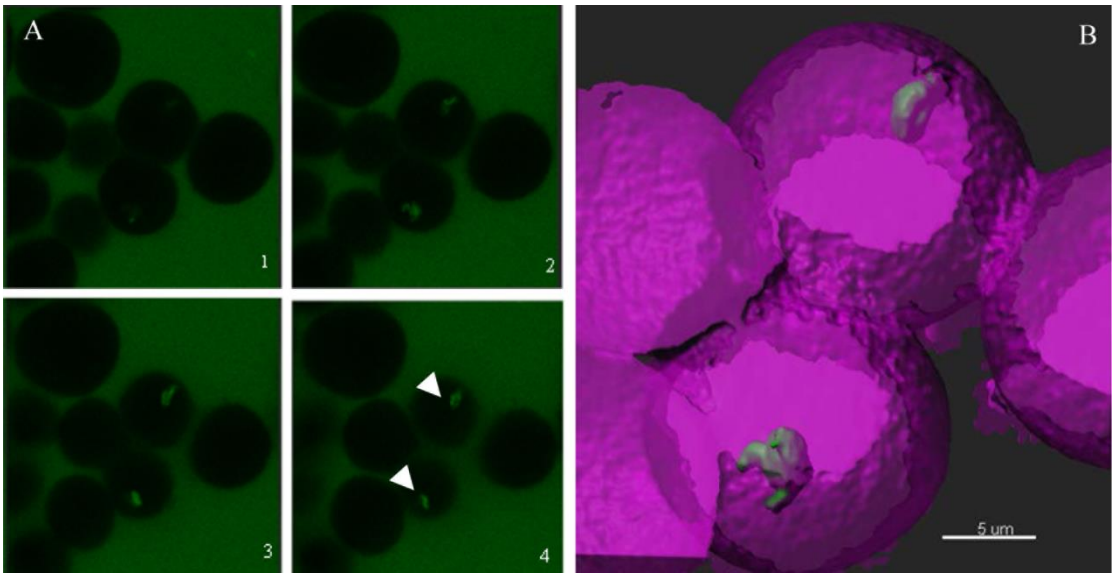

Figure 5-25. Confocal images of individual planes from Z-stack of KB cells after 16 h incubation with GO-PEGFA.

A) The series of time-lapse images from sequential focal planes acquired through the samples were taken at 10 min intervals and interpreted using Imaris software (refer to experimental section 5.2.4.3). Green spots in A2-4 (marked with arrowhead in A4) represent the auto-fluorescence of modified GO sheets inside the cells. A1 shows the middle plane of the cell where the GO sheet is not located. B) 3D reconstruction of a composite Z-stack. Surface of the cells (purple) were rendered as partially transparent in order to show the internalized GO-PEGFA sheets (green). (n=3) Z-stack images were acquired on three occasions.

The interaction of KB cells with RGD-modified GO was also examined under the same conditions (Figure 5-26). Due to the low background fluorescence contrast, the cell area was identified from bright field image. In contrast to the FA-modified GO, RGD-modified GO sheets associated with the cell membrane, no evidence of endocytic uptake was expected.

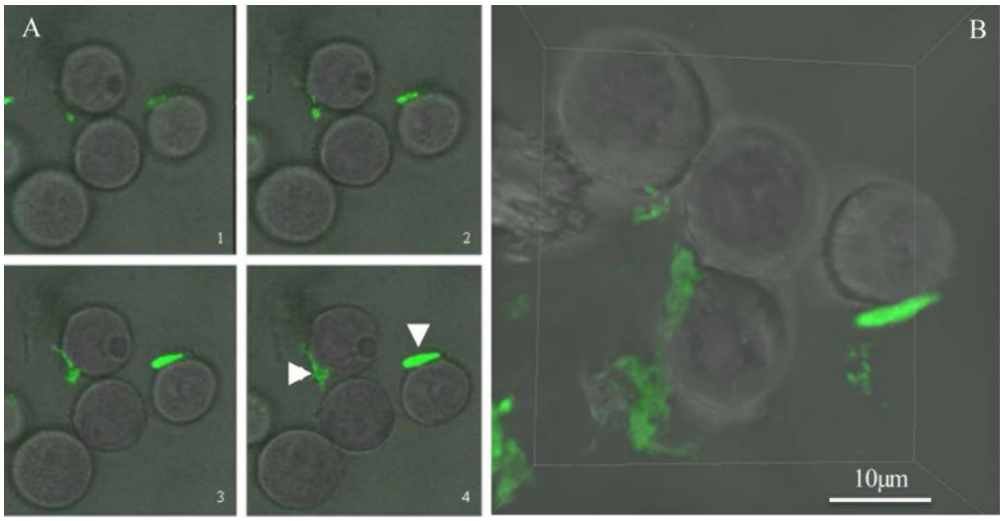

Figure 5-26. Confocal images of individual planes from Z-stack of the KB cells after 16 h incubation with GO-PEGRGD.

A) The series of time-lapse images from sequential focal planes acquired through the samples were taken at 10 min intervals and interpreted using Imaris software (refer to experimental section 5.2.4.3). Green spots (arrowhead in A4) represent the auto-fluorescence of modified GO sheets. B) 3D visualisation of the Z-stack representing the cells (grey) with their associated GO-PEGRGD sheets (green). (n=3) Z-stack images were acquired on three occasions.

The dual ligand modified GO showed the same behaviour as RGD-modified GO which associated to the cell membrane without internalisation (Figure 5-27). After their association with the dual ligand, KB cells partially detached from the culture plates, possibly as a result of integrin binding limiting interaction with nascent ECM deposited onto the plastic culture dish [410].

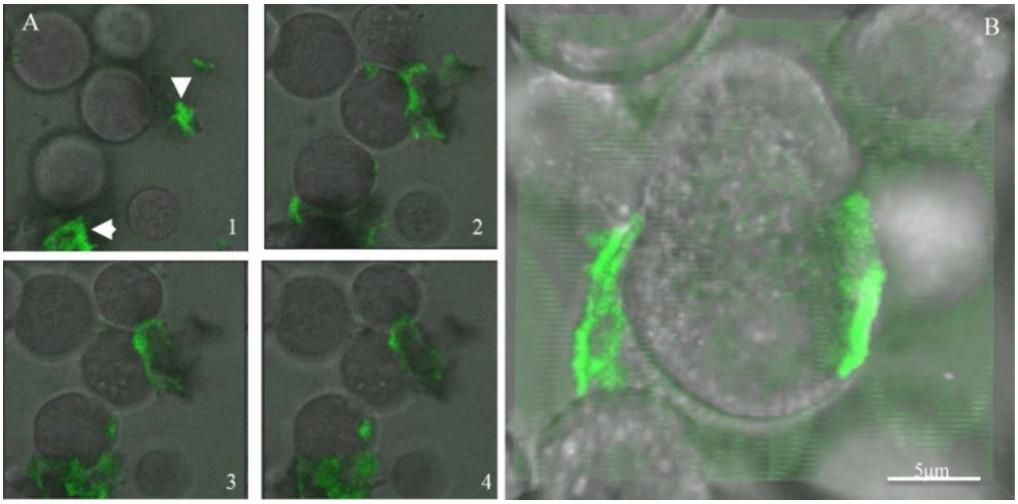

Figure 5-27. Confocal images of individual planes from Z-stack of KB cells after 16 h incubation with GO-PEGFARGD.

A) The series of time-lapse images from sequential focal planes acquired through the samples were taken at 10 min intervals and interpreted using Imaris software (refer to experimental section 5.2.4.3). Green spots (arrowhead in A1) represent the auto-fluorescence of modified GO sheets. B) 3D visualisation of the Z-stack representing the cells (grey) with their associated GO-PEGFARGD sheets (green). (n=3) Z-stack images were acquired on three occasions.

The results from the confocal imaging suggest that the chemistry of the functionalised PEG ligand used to modify GO networks promoted different cell interaction mechanisms. FA-modified GO probably caused an internal change which slowed down the proliferation of the KB cells and activated mechanisms mediating cell death. Conversely, the RGD conjugate might block the integrin receptors to prevent their clustering, which disturbs the cell-matrix adhesion and increases cell death [411, 412].

It can be postulated that the synergistic effects of MTX/DOX with single ligand modified GO to kill cancer cells was due to the ability of the modified GO to increase the proportion of drug accumulation in cell surface or internalisation [82]. The confocal images showed that FA-modified GO appears to be taken up by the treated cells. Considering the possibility of physical adsorption of anti-cancer agents [240] due to their particular structure [413, 414], this type of conjugate may facilitate the transmission of the combined drugs into the tumour cells. However, RGD-modified

networks that associate on the cells surface may facilitate the accumulation of MTX/DOX at the cell membrane, and thus increasing their cytotoxicity effects.

5.4 Conclusions

The modified net-like conjugate utilising graphene oxide, folate and RGD peptide was developed to target certain over-expressed receptors to block endocytosis and impede cell proliferation. The effective surface modification was assessed using spectroscopic characterisation. The PEGylation chemistry was found to be effective and upon TGA analysis up to 50% (w/w) of the superficial carboxyl groups was found to have reacted. The appropriate dimensional size over the range of 200-600 nm and the thickness of 6 nm were also determined using AFM. The reagents showed a 35% reduction in KB cell viability compared to 50% reduction caused by methotrexate, a commonly used anti-cancer agent. Minimal cytotoxicity was evident for BEAS-2B or lung fibroblasts exposed to the reagent.

The cellular interaction of these modified GO networks was observed to be dependent on surface chemistry. FA-modified GO was taken up by tumour cells, whereas, RGD and FARGD-modified GO were only associated with cell membrane. Although the modified GO sheets caused similar levels of cytotoxicity, the mechanisms may differ, as the RGD conjugate and the mixed RGD/FA conjugate are excluded from the intracellular compartment, limiting targets to those on the cell surface.

The combination of the modified GO sheets (FA/RGD-PEGylated GO) with MTX or DOX showed greater maximum toxicity of around 80% reduction in cell viability reflecting the synergistic/additive effects of the system. The particular structure of DOX or MTX facilitates the physical adsorption onto GO surface by π-π interactions. Therefore, GO can promote more accumulation of anti-cancer agent due to the nature of GO-cell interaction. Considering the detected variation in the cytotoxicity mechanisms of FA- and RGD-modified GO, the observed similarity in their synergistic effects needs further study based on intra cellular pathways.

Chapter 6

Conclusions

6 Conclusions

Over-expressed receptors in cancer targeting therapy have been thoroughly studied over the decades to increase the efficiency of cancer treatments, while concurrently reducing the typical adverse/toxic side effects. However, despite remarkable efforts in recently developed targeting therapies, the targeting receptors have been only utilised to deliver anti-cancer drugs or diagnostic compounds to the tumour cells. The transported drugs can still cause unpredicted negative effects in adjacent tissues and non-tumour cells.

This thesis was focused on the synthesis and evaluation of a novel cancer therapeutic system without the use of anti-cancer compounds. The modified net-like conjugate utilizing graphene oxide (GO) polymer, PEG molecule, folate and RGD peptide was developed to target certain over-expressed receptors, blocking endocytosis in tumor cells and resulting in cell metabolic deprivation and death. Such systems explore new strategies for cancer therapy in a selectively toxic way.

Due to the importance of particle size in biomedical applications, a water-glycerol gradient centrifugation method was developed to separate the appropriate sizes of GO. GO sheets are entirely exfoliated in water at concentrations below ~10^{-2} $mg.ml^{-1}$. From these, GO single sheets in the size range of 150 to 850 nm (GOF1-GOF4) were successfully separated. The effective surface modification (ligand-PEGylation) was assessed using spectroscopic characterization. The PEGylation yield was analysed to be around 50% using TGA analysis. The appropriate dimensional sizes of the modified GO over the range of 200-600 nm and the thickness of 5 nm were also determined using AFM.

To explore the optical properties of the modified GO sheets, the auto fluorescence of the introduced networks was studied. Photoluminescence of GO and its fluorescence quenching effect with various attached fluorescents have been widely studied. It has been shown that the quenching effect arises from either fluorescence energy transmission from sp2 domains to the attached fluorescent molecules, or non-fluorescent dipole–dipole coupling between the fluorescent reagent and GO. There are currently no studies into the auto fluorescence of individual GO sheets using fluorescence microscopy. GO and its derivatives show the ability to emit in almost three

main fluorescence regions (blue, green and red). Spectroscopic measurements show that the GO single sheets can auto fluoresce over the range of 400 nm to 700 nm when excitement occurs at the range of 200 nm to 250 nm. The wide emission spectrum covers the main fluorescence regions. However, the emission spectra of GO in other ranges of excitation wavelengths (400 nm to 600 nm) show that GO is able to reflect excitation wavelengths. Furthermore, there are some detected emission peaks at 480 nm, 540 nm, and the broad peaks in 580 nm to 640 nm. This fluorescence could also be used to trace GO sheets in the solution. With different sizes of GO, the same pattern of auto-fluorescence was observed at 200 nm excitation wavelength, which suggests that the observed emission intensity is size independent. GO and derivatized GO have stronger fluorescence at higher pH, while lowering the pH reduces the measured intensity. This may be due to the protonation and deprotonation effects in acidic and alkaline conditions respectively, depending on the chemistry of the molecules (oxidized groups and the adjacent sp2 domains). The data also indicated that functionalized groups make an important contribution to the fluorescence. Fluorescence microscopy also demonstrated the photoluminescence of individual GO sheets in the blue, green and red regions. The lack of fluorescence of some GO sheets in cell media could be attributed to aggregation of the sheets. The attached functionalized groups can change the observed fluorescence emission of the GO sheets in cellular experiment. RGD-PEGylated GO emits in the green fluorescent area, while FA-PEGylated GO emits in the red and blue regions. Designed PEGylated GO sheets (GO-PEG-FA or RGD) significantly affect the appearance of treated cells. Based on these observations, GO auto-fluorescence seems to be complex and dependent on various chemical and physical factors. However, further work is required to understand the influence of the environmental and aggregation effects on auto-fluorescence of GO. As a result, GO sheets have the potential to be used as tracers in biological systems, provided further tests prove positive which includes animal testing.

To study the cytotoxicity effects of the introduced ligand-modified GO, three different cell lines were examined using WST assay and trypan blue. KB as a malignant cervix tumor cells showed 35% reduction in viability, compared to the 50% reduction caused by the common anti-cancer agent methotrexate. BEAS-2B as a proliferative non-tumor cell line and lung fibroblasts as normal resting connective cells exhibited 20% and 10%

reduction in cell viability respectively. The difference in observed cytotoxicity may be due to the cell proliferation rate, which is expected to enhance their sensitivity to the antiproliferative agents (MTX or the introduced modified GO sheets). Notably, the cytotoxicity of the PEGylated GO (GO-PEG) was concentration-dependent. Only small-reduced cell viability is observed at the concentration of 2.6 $mg.ml^{-1}$. This initial observation showed the promising capability of the modified GO sheets leading cancer approaches to the new therapeutic methods.

The cellular interaction of the GO networks was also observed to be dependent on surface chemistry. FA-modified GO was taken up by tumour cells, whereas, RGD and FARGD-modified GO were only associated with the cell membrane. The modified GO sheets appeared to cause the same cytotoxicity in two different ways: FA-modified GO may activate intracellular mechanisms, which mediate cell death. The RGD conjugate, however, might block the integrin receptors, disturbing the appropriate cell-matrix adhesion leading to cell death. The combination of the modified GO sheets (FA/RGD-PEGylated GO) with MTX or DOX showed greater maximum toxicity of around 80% reduction in cell viability, reflecting the synergistic/additive effect of this combination. The particular structure of DOX and MTX facilitate the physical adsorption onto GO surface via π-π interactions. The initial assumption behind this observation is that FA-modified GO facilitate the uptake of anti-cancer agents into the tutor cells, increasing their cytotoxic effects. However, RGD-modified networks that only associate with the treated cells may assist increased accumulation of MTX/DOX next to the cell membrane, enhancing their mediated cytotoxicity. This assumption and the similar synergistic effects of these two single ligand-modified GO needs further investigation considering their different cellular interactions.

Based on the results demonstrated in this thesis, it is concluded that the proposed separation and fractionation method is relatively simple and easy to use in biomedical studies where the appropriate nano-sizes of GO is desired (from 100 nm to less than 800 nm depending on the intended application). Moreover, the modified GO sheets have the potential in cell signalling and tracking in clinical studies based on the observed auto fluorescence effects. This system showed encouraging results for cancer therapy in a selectively toxic way considering the observed cytotoxic and synergistic effects.

7 References

1. Ferlay, J., et al., *Cancer incidence and mortality worldwide: sources, methods and major patterns in GLOBOCAN 2012.* International Journal of Cancer, 2015. **136**(5): p. E359-E386.
2. Farber, E., *The multistep nature of cancer development.* Cancer research, 1984. **44**(10): p. 4217-4223.
3. Gillies, R.J. and R.A. Gatenby, *Hypoxia and adaptive landscapes in the evolution of carcinogenesis.* Cancer and Metastasis Reviews, 2007. **26**(2): p. 311-317.
4. Gatenby, R.A. and R.J. Gillies, *A microenvironmental model of carcinogenesis.* Nature Reviews Cancer, 2008. **8**(1): p. 56-61.
5. Polyak, K. and R.A. Weinberg, *Transitions between epithelial and mesenchymal states: acquisition of malignant and stem cell traits.* Nature Reviews Cancer, 2009. **9**(4): p. 265-273.
6. Yoshioka, K.-I., et al., *Development of cancer-initiating cells and immortalized cells with genomic instability.* World journal of stem cells, 2015. **7**(2): p. 483-9.
7. Weinberg, R., *The biology of cancer*. 2013: Garland science.
8. Evan, G.I. and K.H. Vousden, *Proliferation, cell cycle and apoptosis in cancer.* Nature, 2001. **411**(6835): p. 342-348.
9. Cohen, S.M. and L.B. Ellwein, *Cell proliferation in carcinogenesis.* 1990.
10. Schwartz, M.A., *Signaling by integrins: implications for tumorigenesis.* Cancer Research, 1993. **53**(7): p. 1503-1506.
11. Chang, C. and Z. Werb, *The many faces of metalloproteases: cell growth, invasion, angiogenesis and metastasis.* Trends in cell biology, 2001. **11**(11): p. S37-S43.
12. Reya, T., et al., *Stem cells, cancer, and cancer stem cells.* nature, 2001. **414**(6859): p. 105-111.
13. Jin, Z. and W.S. El-Deiry, *Overview of cell death signaling pathways.* Cancer biology & therapy, 2005. **4**(2): p. 147-171.
14. McKenzie, S. and N. Kyprianou, *Apoptosis evasion: The role of survival pathways in prostate cancer progression and therapeutic resistance.* Journal of Cellular Biochemistry, 2006. **97**(1): p. 18-32.
15. Broekgaarden, M., et al., *Tumor cell survival pathways activated by photodynamic therapy: a molecular basis for pharmacological inhibition strategies.* Cancer and Metastasis Reviews, 2015. **34**(4): p. 643-690.
16. W Fisher, K., et al., *Molecular foundations for personalized therapy in prostate cancer.* Current drug targets, 2015. **16**(2): p. 103-114.
17. Singh, N., et al., *Clinical aspects for survivin: a crucial molecule for targeting drug-resistant cancers.* Drug discovery today, 2015. **20**(5): p. 578-587.
18. Coward, J.I., K. Middleton, and F. Murphy, *New perspectives on targeted therapy in ovarian cancer.* International journal of women's health, 2015. **7**: p. 189.
19. Salk, J.J., E.J. Fox, and L.A. Loeb, *Mutational heterogeneity in human cancers: origin and consequences.* Annual review of pathology, 2010. **5**: p. 51.

20. Mardis, E.R. and R.K. Wilson, *Cancer genome sequencing: a review.* Human molecular genetics, 2009. **18**(R2): p. R163-R168.
21. Langley, R.R. and I.J. Fidler, *The seed and soil hypothesis revisited—The role of tumor-stroma interactions in metastasis to different organs.* International Journal of Cancer, 2011. **128**(11): p. 2527-2535.
22. Duffy, M.J., *The war on cancer: are we winning?* Tumor Biology, 2013. **34**(3): p. 1275-1284.
23. Baskar, R., et al., *Cancer and radiation therapy: current advances and future directions.* Int J Med Sci, 2012. **9**(3): p. 193-9.
24. Chen, Y., et al., *Collateral damage in cancer chemotherapy: oxidative stress in nontargeted tissues.* Molecular interventions, 2007. **7**(3): p. 147.
25. Phillips, T.L., M.D. Wharam, and L.W. Margolis, *Modification of radiation injury to normal tissues by chemotherapeutic agents.* Cancer, 1975. **35**(6): p. 1678-1684.
26. Lee, C.S., E.J. Ryan, and G.A. Doherty, *Gastro-intestinal toxicity of chemotherapeutics in colorectal cancer: the role of inflammation.* World J Gastroenterol, 2014. **20**(14): p. 3751-61.
27. Trueb, R.M., *Chemotherapy-induced hair loss.* Skin Therapy Lett, 2010. **15**(7): p. 5-7.
28. Brigden, M. and M. McKenzie, *Treating cancer patients. Practical monitoring and management of therapy-related complications.* Canadian Family Physician, 2000. **46**(11): p. 2258-68.
29. Zhang, Y., *FOLATE RECEPTOR-TARGETED DELIVERY OF SMALL INTERFERING RNA TO CANCER CELLS*. December 2010, The University of Southern Mississippi. p. 143.
30. Gilstrap, K., *SYNTHESIS AND CHARACTERIZATION OF THERMALLY RESPONSIVE NANOCAPSULES SURFACE DECORATED WITH FOLIC ACID FOR TARGETED DRUG DELIVERY AND CANCER DESTRUCTION*, in *Biomedical Engineering*. 2011, University of South Carolina. p. 55.
31. Stan Kaye, R.B., Hani Gabra, Martin Gore, *Emerging Therapeutic Targets in Ovarian Cancer* 2010, London: Springer.
32. Margaret Barton-Burke, G.M.W., *Cancer therapies*. 2006: Jones and Bartlett
33. Sui, M., W. Liu, and Y. Shen, *Nuclear drug delivery for cancer chemotherapy.* Journal of Controlled Release, 2011.
34. Meng, H., et al., *Conjugates of folic acids with BSA-coated quantum dots for cancer cell targeting and imaging by single-photon and two-photon excitation.* Journal of Biological Inorganic Chemistry, 2011. **16**(1): p. 117-123.
35. Saul, J.M., et al., *Controlled targeting of liposomal doxorubicin via the folate receptor in vitro.* Journal of Controlled Release, 2003. **92**(1): p. 49-67.
36. Pasut, G. and F.M. Veronese, *PEG conjugates in clinical development or use as anticancer agents: an overview.* Advanced drug delivery reviews, 2009. **61**(13): p. 1177-1188.
37. Amiji, M.M., *Polymeric Gene Delivery: Principles and Applications*. 2005: CRC Publisher

38. Lu, D., et al., *Comparison of candidate serologic markers for type I and type II ovarian cancer.* Gynecologic Oncology, 2011.
39. Magee, J.A., E. Piskounova, and S.J. Morrison, *Cancer Stem Cells: Impact, Heterogeneity, and Uncertainty.* Cancer Cell, 2012. **21**(3): p. 283-296.
40. Dakshinamurti, K., *Vitamin Receptors: Vitamins As Ligands in Cell Communication* 1994, New York: Cambridge University Press.
41. Mayani, D.D., *Proton therapy for cancer treatment.* Journal of Oncology Pharmacy Practice, 2011. **17**(3): p. 186-190.
42. Slater, J.D., et al., *Proton therapy for prostate cancer: the initial Loma Linda University experience.* International Journal of Radiation Oncology* Biology* Physics, 2004. **59**(2): p. 348-352.
43. Ferrara, N. *Role of vascular endothelial growth factor in physiologic and pathologic angiogenesis: therapeutic implications*. in *Seminars in oncology*. 2002. Elsevier.
44. Bergers, G. and L.E. Benjamin, *Tumorigenesis and the angiogenic switch.* Nature reviews cancer, 2003. **3**(6): p. 401-410.
45. Folkman, J. *Role of angiogenesis in tumor growth and metastasis*. in *Seminars in oncology*. 2002. Elsevier.
46. Carmeliet, P., *Angiogenesis in life, disease and medicine.* Nature, 2005. **438**(7070): p. 932-936.
47. Wang, Z., et al., *Broad targeting of angiogenesis for cancer prevention and therapy.* Seminars in Cancer Biology, 2015(0).
48. Deryugina, E.I. and J.P. Quigley, *Tumor angiogenesis: MMP-mediated induction of intravasation- and metastasis-sustaining neovasculature.* Matrix Biology, (0).
49. Vogelstein, B., et al., *Cancer genome landscapes.* science, 2013. **339**(6127): p. 1546-1558.
50. Grivennikov, S.I., F.R. Greten, and M. Karin, *Immunity, inflammation, and cancer.* Cell, 2010. **140**(6): p. 883-899.
51. Alizadeh, A., S. Shiri, and S. Farsinejad, *Metastasis review: from bench to bedside.* Tumor Biology, 2014. **35**(9): p. 8483-8523.
52. Feng Wan1, *, Christel Herold-Mende1,*, Benito Campos1,*, Franz-Simon Centner1, Christine Dictus1, Natalia Becker3, Frauke Devens3, Carolin Mogler4, Jörg Felsberg5, Niels Grabe6, Guido Reifenberger5, Peter Lichter3, Andreas Unterberg1, Justo Lorenzo Bermejo7,8, Rezvan Ahmadi1, *Association of Stem Cell-Related Markers and Survival in Astrocytic Gliomas.* Biomarkers, 2011. **16**(2): p. 136–143.
53. Shao, M., et al., *A subset of breast cancer predisposes to brain metastasis.* Medical Molecular Morphology, 2011. **44**(1): p. 15-20.
54. Haley, B. and E. Frenkel. *Nanoparticles for drug delivery in cancer treatment*. in *Urologic Oncology: Seminars and original investigations*. 2008. Elsevier.
55. Shackleton, M. *Normal stem cells and cancer stem cells: similar and different*. 2010. Elsevier.
56. Dalerba, P., R.W. Cho, and M.F. Clarke, *Cancer stem cells: models and concepts.* Annu. Rev. Med., 2007. **58**: p. 267-284.

57. Sellheyer, K., *Basal cell carcinoma: cell of origin, cancer stem cell hypothesis and stem cell markers.* British Journal of Dermatology, 2011.
58. Cheng, J.X., B.L. Liu, and X. Zhang, *How powerful is CD133 as a cancer stem cell marker in brain tumors?* Cancer treatment reviews, 2009. **35**(5): p. 403-408.
59. Brannon-Peppas, L. and J.O. Blanchette, *Nanoparticle and targeted systems for cancer therapy.* Advanced drug delivery reviews, 2012. **64**: p. 206-212.
60. Singh, T. and S.K. Katiyar, *Green Tea Catechins Reduce Invasive Potential of Human Melanoma Cells by Targeting COX-2, PGE2 Receptors and Epithelial-to-Mesenchymal Transition.* PloS one, 2011. **6**(10): p. e25224.
61. Liu, L.L., et al., *The power and the promise of liver cancer stem cell markers.* Stem Cells and Development, 2011. **20**(12): p. 2023-2030.
62. Fargeas, C.A., D. Corbeil, and W.B. Huttner, *AC133 Antigen, CD133, Prominin-1, Prominin-2, Etc.: Prominin Family Gene Products in Need of a Rational Nomenclature.* Stem Cells, 2003. **21**(4): p. 506-508.
63. Shmelkov, S.V., et al., *AC133/CD133/Prominin-1.* The international journal of biochemistry & cell biology, 2005. **37**(4): p. 715-719.
64. Mak, A.B., et al., *CD133 Protein N-Glycosylation Processing Contributes to Cell Surface Recognition of the Primitive Cell Marker AC133 Epitope.* Journal of Biological Chemistry, 2011. **286**(47): p. 41046-41056.
65. Lee, S.W., et al., *Tumor cell growth inhibition by caveolin re-expression in human breast cancer cells.* Oncogene, 1998. **16**(11): p. 1391.
66. Friedrichson, T. and T.V. Kurzchalia, *Microdomains of GPI-anchored proteins in living cells revealed by crosslinking.* Nature, 1998. **394**(6695): p. 802-805.
67. Jacobson, K. and C. Dietrich, *Looking at lipid rafts?* Trends in cell biology, 1999. **9**(3): p. 87-91.
68. Simons, K. and R. Ehehalt, *Cholesterol, lipid rafts, and disease.* Journal of Clinical Investigation, 2002. **110**(5): p. 597-604.
69. Parveen, S., R. Misra, and S.K. Sahoo, *Nanoparticles: a boon to drug delivery, therapeutics, diagnostics and imaging.* Nanomedicine: Nanotechnology, Biology and Medicine, 2012. **8**(2): p. 147-166.
70. Cho, K., et al., *Therapeutic nanoparticles for drug delivery in cancer.* Clinical cancer research, 2008. **14**(5): p. 1310-1316.
71. Peer, D., et al., *Nanocarriers as an emerging platform for cancer therapy.* Nature nanotechnology, 2007. **2**(12): p. 751-760.
72. Ruenraroengsak, P., J.M. Cook, and A.T. Florence, *Nanosystem drug targeting: facing up to complex realities.* Journal of Controlled Release, 2010. **141**(3): p. 265-276.
73. Davis, M.E. and D.M. Shin, *Nanoparticle therapeutics: an emerging treatment modality for cancer.* Nature reviews Drug discovery, 2008. **7**(9): p. 771-782.
74. Zhang, L., et al., *Nanoparticles in medicine: therapeutic applications and developments.* Clinical pharmacology and therapeutics, 2008. **83**(5): p. 761-769.
75. Brigger, I., C. Dubernet, and P. Couvreur, *Nanoparticles in cancer therapy and diagnosis.* Advanced drug delivery reviews, 2002. **54**(5): p. 631-651.
76. Saltzman, W.M., T. Fahmy, and P. Fong, *Targeted and high density drug loaded polymeric materials*. 2009, Google Patents.

77. Heneweer, C., S.E. Gendy, and O. Peñate-Medina, *Liposomes and inorganic nanoparticles for drug delivery and cancer imaging.* Therapeutic delivery, 2012. **3**(5): p. 645-656.
78. Albanese, A., P.S. Tang, and W.C. Chan, *The effect of nanoparticle size, shape, and surface chemistry on biological systems.* Annual review of biomedical engineering, 2012. **14**: p. 1-16.
79. Perrault, S.D., et al., *Mediating tumor targeting efficiency of nanoparticles through design.* Nano letters, 2009. **9**(5): p. 1909-1915.
80. Taurin, S., H. Nehoff, and K. Greish, *Anticancer nanomedicine and tumor vascular permeability; where is the missing link?* Journal of Controlled Release, 2012. **164**(3): p. 265-275.
81. Bertrand, N., et al., *Cancer nanotechnology: the impact of passive and active targeting in the era of modern cancer biology.* Advanced drug delivery reviews, 2014. **66**: p. 2-25.
82. Allen, T.M. and P.R. Cullis, *Drug delivery systems: entering the mainstream.* Science, 2004. **303**(5665): p. 1818-1822.
83. Singh, R. and J.W. Lillard, *Nanoparticle-based targeted drug delivery.* Experimental and molecular pathology, 2009. **86**(3): p. 215-223.
84. Ijeoma F. Uchegbu, A.G.S., *Polymers in drug delivery* 2006: CRC Press.
85. Soppimath, K.S., et al., *Biodegradable polymeric nanoparticles as drug delivery devices.* Journal of controlled release, 2001. **70**(1): p. 1-20.
86. Silverman, J.A. and S.R. Deitcher, *Marqibo®(vincristine sulfate liposome injection) improves the pharmacokinetics and pharmacodynamics of vincristine.* Cancer chemotherapy and pharmacology, 2013. **71**(3): p. 555-564.
87. Mistro, S., et al., *Cost-effectiveness of caspofungin versus liposomal amphotericin B in the treatment of systemic fungal infections: a systematic review of economic analyses.* Expert Review of Pharmacoeconomics & Outcomes Research, 2016. **16**(4): p. 465-473.
88. Cunha, M.A., et al., *Efficacy and safety of liposomal amphotericin B for the treatment of mucosal leishmaniasis from the New World: a retrospective study.* The American journal of tropical medicine and hygiene, 2015. **93**(6): p. 1214-1218.
89. Hu, C.-M.J., S. Aryal, and L. Zhang, *Nanoparticle-assisted combination therapies for effective cancer treatment.* Therapeutic delivery, 2010. **1**(2): p. 323-334.
90. Kumari, A., S.K. Yadav, and S.C. Yadav, *Biodegradable polymeric nanoparticles based drug delivery systems.* Colloids and Surfaces B: Biointerfaces, 2010. **75**(1): p. 1-18.
91. He, C., et al., *Effects of particle size and surface charge on cellular uptake and biodistribution of polymeric nanoparticles.* Biomaterials, 2010. **31**(13): p. 3657-3666.
92. Lee, C.C., et al., *Designing dendrimers for biological applications.* Nature biotechnology, 2005. **23**(12): p. 1517-1526.
93. Gillies, E.R. and J.M. Frechet, *Dendrimers and dendritic polymers in drug delivery.* Drug discovery today, 2005. **10**(1): p. 35-43.

94. Madjd Z , H.F., Shayanfar N, Farahani E , Zarnani AH, Sharifi AM, Akbari ME, *OCT-4, an Embryonic Stem Cell Marker Expressed in Breast, Brain and Thyroid Carcinomas Compared to Testicular Carcinoma.* Iranian Journal of Cancer Prevention, 2009. **2**(4): p. 167-173.
95. Sanna, V., N. Pala, and M. Sechi, *Targeted therapy using nanotechnology: focus on cancer.* International journal of nanomedicine, 2014. **9**: p. 467.
96. Maruyama, K., *Intracellular targeting delivery of liposomal drugs to solid tumors based on EPR effects.* Advanced drug delivery reviews, 2011. **63**(3): p. 161-169.
97. Jang, C., et al., *The synergistic effect of folate and RGD dual ligand of nanographene oxide on tumor targeting and photothermal therapy in vivo.* Nanoscale, 2015.
98. Maeda, H., *Vascular permeability in cancer and infection as related to macromolecular drug delivery, with emphasis on the EPR effect for tumor-selective drug targeting.* Proceedings of the Japan Academy. Series B, Physical and biological sciences, 2012. **88**(3): p. 53.
99. Junttila, M.R. and F.J. de Sauvage, *Influence of tumour micro-environment heterogeneity on therapeutic response.* Nature, 2013. **501**(7467): p. 346-354.
100. Srinivasarao, M., C.V. Galliford, and P.S. Low, *Principles in the design of ligand-targeted cancer therapeutics and imaging agents.* Nature Reviews Drug Discovery, 2015.
101. Naci, D., K. Vuori, and F. Aoudjit. *Alpha2beta1 integrin in cancer development and chemoresistance*. in *Seminars in cancer biology*. 2015. Elsevier.
102. Frieboes, H.B., et al., *A computational model for predicting nanoparticle accumulation in tumor vasculature.* PloS one, 2013. **8**(2): p. e56876.
103. Song, G., et al., *Effects of tumor microenvironment heterogeneity on nanoparticle disposition and efficacy in breast cancer tumor models.* Clinical Cancer Research, 2014. **20**(23): p. 6083-6095.
104. Petros, R.A. and J.M. DeSimone, *Strategies in the design of nanoparticles for therapeutic applications.* Nature reviews Drug discovery, 2010. **9**(8): p. 615-627.
105. Choi, H.S., et al., *Design considerations for tumour-targeted nanoparticles.* Nature nanotechnology, 2010. **5**(1): p. 42-47.
106. Wang, X., et al., *Application of nanotechnology in cancer therapy and imaging.* CA: a cancer journal for clinicians, 2008. **58**(2): p. 97-110.
107. Karra, N. and S. Benita, *The ligand nanoparticle conjugation approach for targeted cancer therapy.* Current drug metabolism, 2012. **13**(1): p. 22-41.
108. Xia, W. and P.S. Low, *Folate-targeted therapies for cancer.* Journal of medicinal chemistry, 2010. **53**(19): p. 6811-6824.
109. Ishida, T. and R. Ueda, *CCR4 as a novel molecular target for immunotherapy of cancer.* Cancer science, 2006. **97**(11): p. 1139-1146.
110. Waehler, R., S.J. Russell, and D.T. Curiel, *Engineering targeted viral vectors for gene therapy.* Nature Reviews Genetics, 2007. **8**(8): p. 573-587.
111. Scott, A.M., J.D. Wolchok, and L.J. Old, *Antibody therapy of cancer.* Nature Reviews Cancer, 2012. **12**(4): p. 278-287.
112. Ozpolat, B., A.K. Sood, and G. Lopez-Berestein, *Liposomal siRNA nanocarriers for cancer therapy.* Advanced drug delivery reviews, 2014. **66**: p. 110-116.

113. Prager, G., et al., *CD98hc (SLC3A2), a novel marker in renal cell cancer.* European journal of clinical investigation, 2009. **39**(4): p. 304-310.
114. Rocco, A., et al., *CD133 and CD44 Cell surface markers do not identify cancer stem cells in primary human gastric tumors.* Journal of Cellular Physiology, 2012. **227**(6): p. 2686-2693.
115. Paratore, S., et al., *CXCR4 and CXCL12 immunoreactivities differentiate primary non-small-cell lung cancer with or without brain metastases.* Cancer Biomarkers, 2011. **10**(2): p. 79-89.
116. Manoj, L., et al., *REVIEW OF BRAIN AND BRAIN CANCER TREATMENT.*
117. Agarwal, S., et al., *Breast Cancer Resistance Protein and P-Glycoprotein in Brain Cancer: Two Gatekeepers Team Up.* Current pharmaceutical design, 2011. **17**(26): p. 2793.
118. Dudu, V., V. Rotari, and M. Vazquez, *Targeted extracellular nanoparticles enable intracellular detection of activated epidermal growth factor receptor in living brain cancer cells.* Nanomedicine: Nanotechnology, Biology and Medicine, 2011.
119. Parker, N., et al., *Folate receptor expression in carcinomas and normal tissues determined by a quantitative radioligand binding assay.* Analytical biochemistry, 2005. **338**(2): p. 284-293.
120. Antony, A.C., *Folate receptors.* Annual review of nutrition, 1996. **16**(1): p. 501-521.
121. Ross, J.F., P.K. Chaudhuri, and M. Ratnam, *Differential regulation of folate receptor isoforms in normal and malignant tissues in vivo and in established cell lines. Physiologic and clinical implications.* Cancer, 1994. **73**(9): p. 2432-2443.
122. Galanzha, E.I., et al., *In vivo magnetic enrichment and multiplex photoacoustic detection of circulating tumour cells.* Nature nanotechnology, 2009. **4**(12): p. 855-860.
123. Sudimack, J. and R.J. Lee, *Targeted drug delivery via the folate receptor.* Advanced drug delivery reviews, 2000. **41**(2): p. 147-162.
124. Fröhlich, E. and R. Wahl, *Do antidiabetic medications play a specific role in differentiated thyroid cancer compared to other cancer types?* Diabetes, Obesity and Metabolism, 2012.
125. Allen, T.M., *Ligand-targeted therapeutics in anticancer therapy.* Nature Reviews Cancer, 2002. **2**(10): p. 750-763.
126. Elias, D.R., et al., *Effect of ligand density, receptor density, and nanoparticle size on cell targeting.* Nanomedicine: nanotechnology, biology and medicine, 2013. **9**(2): p. 194-201.
127. Ahmed, S. and Z.Q. Samra, *Engineering Transferrin and Epirubicin onto Magnetic Nanoparticles for Targeting Drug Delivery Through Transferrin Receptors.* Pakistan J. Zool, 2016. **48**(4): p. 1117-1124.
128. Chen, J., et al., *Post-coupling strategy enables true receptor-targeted nanoparticles.* J RNAi Gene Silencing, 2011. **7**: p. 449-455.
129. Farokhzad, O.C., et al., *Targeted Polymeric Inflammation-Resolving Nanoparticles*. 2014, Google Patents.

130. Pereira, P.M., et al., *Antibodies armed with photosensitizers: from chemical synthesis to photobiological applications.* Organic & biomolecular chemistry, 2015. **13**(9): p. 2518-2529.
131. Sykes, E.A., et al., *Investigating the impact of nanoparticle size on active and passive tumor targeting efficiency.* ACS nano, 2014. **8**(6): p. 5696-5706.
132. Jain, R.K. and T. Stylianopoulos, *Delivering nanomedicine to solid tumors.* Nature reviews Clinical oncology, 2010. **7**(11): p. 653-664.
133. Leamon, C.P. and J.A. Reddy, *Folate-targeted chemotherapy.* Advanced drug delivery reviews, 2004. **56**(8): p. 1127-1141.
134. Schneider, R., et al., *Design, synthesis, and biological evaluation of folic acid targeted tetraphenylporphyrin as novel photosensitizers for selective photodynamic therapy.* Bioorganic & medicinal chemistry, 2005. **13**(8): p. 2799-2808.
135. Chiu, C.C., et al., *Anticancer Activity of Released Doxorubicin from a Folate-Mediated Polyelectrolyte Complex.* Journal of Biomaterials Science, Polymer Edition, 2011. **22**(11): p. 1487-1507.
136. Park, E.K., et al., *Folate-conjugated methoxy poly (ethylene glycol)/poly (ε-caprolactone) amphiphilic block copolymeric micelles for tumor-targeted drug delivery.* Journal of Controlled Release, 2005. **109**(1): p. 158-168.
137. Strękowski, L., *Heterocyclic Polymethine Dyes: Synthesis, Properties and Applications* 2008: Springer. 241.
138. TIKEKAR, S., *DEVELOPMENT OF INDOCYANINE GREEN LOADED LONG CniCULATING AND FOLATE-RECEPTOR-TARGETED PLGA NANOPARTICLES FOR PHOTODYNAMIC THERAPY OF BREAST CANCER*, in *COLLEGE OF PHARMACY AND ALLIED HEALTH PROFESSIONS*. 2011, ST. JOHN'S UNIVERSITY: Jamaica, New York. p. 196.
139. Amiji, M.M., *Nanotechnology for Cancer Therapy* 2007: CRC Press.
140. Gabizon, A., et al., *Tumor cell targeting of liposome-entrapped drugs with phospholipid-anchored folic acid–PEG conjugates.* Advanced drug delivery reviews, 2004. **56**(8): p. 1177-1192.
141. Jones, T. and N. Saba, *Nanotechnology and Drug Delivery: An Update in Oncology.* Pharmaceutics, 2011. **3**(2): p. 171-185.
142. Deepak Thassu, M.D., Yashwant Path, *Nanoparticulate Drug Delivery Systems* 2007, New York: CRC Press.
143. Miraglia, S., et al., *A novel five-transmembrane hematopoietic stem cell antigen: isolation, characterization, and molecular cloning.* Blood, 1997. **90**(12): p. 5013-5021.
144. Vu, L., *A Focused Poly(Aminoether) Library for Transgene Delivery to Cancer Cells*. August 2011, ARIZONA STATE UNIVERSITY. p. 61.
145. Jaracz, S., et al., *Recent advances in tumor-targeting anticancer drug conjugates.* Bioorganic & medicinal chemistry, 2005. **13**(17): p. 5043-5054.
146. Weng, J., et al., *High sensitive detection of cancer cell with a folic acid-based boron-doped diamond electrode using an AC impedimetric approach.* Biosensors and Bioelectronics, 2011. **26**(5): p. 1847-1852.

147. Kristel Kemper1, M.R.S., Martijn de Bree1, Alessandro Scopelliti3, Louis Vermeulen1, Maarten Hoek4, Jurrit Zeilstra2, Steven T. Pals2, Huseyin Mehmet4, Giorgio Stassi3, and Jan Paul Medema1, *The AC133 Epitope, but not the CD133 Protein, Is Lost upon Cancer Stem Cell Differentiation.* Tumor and Stem Cell Biology, 2010. **12**.
148. Quintana, A., et al., *Design and function of a dendrimer-based therapeutic nanodevice targeted to tumor cells through the folate receptor.* Pharmaceutical research, 2002. **19**(9): p. 1310-1316.
149. Lu, Y. and P.S. Low, *Immunotherapy of folate receptor-expressing tumors: review of recent advances and future prospects.* Journal of Controlled Release, 2003. **91**(1): p. 17-29.
150. Destito, G., et al., *Folic acid-mediated targeting of cowpea mosaic virus particles to tumor cells.* Chemistry & biology, 2007. **14**(10): p. 1152-1162.
151. Turek, J.J., C.P. Leamon, and P.S. Low, *Endocytosis of folate-protein conjugates: ultrastructural localization in KB cells.* Journal of cell science, 1993. **106**(1): p. 423-430.
152. Cheristofer P. Leamon, R.B.D., R. Wayne Hendren, *Folate mediated drug delivery: effect of alternative conjugative chemistry.* Journal of Drug Targeting, 1999. **7**(3): p. 157-169.
153. Melpomeni Fani, Maria-Luisa Tamma, Guillaume P. Nicolas, Elisabeth Lasri, Christelle Medina, and M.P. Isabelle Raynal, Wolfgang A. Weber, and Helmut R. Maecke, *In Vivo Imaging of Folate Receptor Positive Tumor Xenografts Using Novel 68Ga-NODAGA-Folate Conjugates.* Molecular . Pharmaceutics, 2012. **9**: p. 1136−1145.
154. Coney, L.R., et al., *Cloning of a tumor-associated antigen: MOv18 and MOv19 antibodies recognize a folate-binding protein.* Cancer research, 1991. **51**(22): p. 6125.
155. Swihart, F.E.a.M.T., *Imaging Pancreatic Cancer with Folic Acid Terminated Luminescent Silicon Nanocrystals*.
156. Zou, T., et al., *Synthesis of Poly (,-[N-(2-hydroxyethyl)-L-aspartamide])-folate for Drug Delivery.* Journal of Biomaterials Science, Polymer Edition, 21, 2010. **6**(7): p. 759-770.
157. Rosenholm, J.M., et al., *Targeted intracellular delivery of hydrophobic agents using mesoporous hybrid silica nanoparticles as carrier systems.* Nano letters, 2009. **9**(9): p. 3308-3311.
158. Leamon, C.P. and A.L. Jackman, *Exploitation of the folate receptor in the management of cancer and inflammatory disease.* Vitamins & Hormones, 2008. **79**: p. 203-233.
159. Wu, D. and W.M. Pardridge, *Blood-brain barrier transport of reduced folic acid.* Pharmaceutical research, 1999. **16**(3): p. 415-419.
160. Low, P.S., W.A. Henne, and D.D. Doorneweerd, *Discovery and development of folic-acid-based receptor targeting for imaging and therapy of cancer and inflammatory diseases.* Accounts of chemical research, 2007. **41**(1): p. 120-129.
161. Lu, Y. and P.S. Low, *Folate-mediated delivery of macromolecular anticancer therapeutic agents.* Advanced drug delivery reviews, 2012. **64**: p. 342-352.

162. Hilgenbrink, A.R. and P.S. Low, *Folate receptor-mediated drug targeting: From therapeutics to diagnostics.* Journal of pharmaceutical sciences, 2005. **94**(10): p. 2135-2146.
163. Arima, H., et al., *Folate-PEG-appended dendrimer conjugate with α-cyclodextrin as a novel cancer cell-selective siRNA delivery carrier.* Molecular pharmaceutics, 2012. **9**(9): p. 2591-2604.
164. Kang, C., et al., *Evaluation of folate-PAMAM for the delivery of antisense oligonucleotides to rat C6 glioma cells in vitro and in vivo.* Journal of Biomedical Materials Research Part A, 2010. **93**(2): p. 585-594.
165. Guo, F., et al., *Smart IR780 Theranostic Nanocarrier for Tumor-Specific Therapy: Hyperthermia-Mediated Bubble-Generating and Folate-Targeted Liposomes.* ACS applied materials & interfaces, 2015. **7**(37): p. 20556-20567.
166. Shao, D., et al., *Noninvasive theranostic imaging of HSV-TK/GCV suicide gene therapy in liver cancer by folate-targeted quantum dot-based liposomes.* Biomaterials Science, 2015. **3**(6): p. 833-841.
167. Wu, D., et al., *Anti-tumor activity of folate targeted biodegradable polymer–paclitaxel conjugate micelles on EMT-6 breast cancer model.* Materials Science and Engineering: C, 2015. **53**: p. 68-75.
168. Syu, W.J., et al., *Improved photodynamic cancer treatment by folate-conjugated polymeric micelles in a KB xenografted animal model.* Small, 2012. **8**(13): p. 2060-2069.
169. Ndong, C., et al., *Antibody-mediated targeting of iron oxide nanoparticles to the folate receptor alpha increases tumor cell association in vitro and in vivo.* International journal of nanomedicine, 2015. **10**: p. 2595.
170. Idris, N.M., et al., *In vivo photodynamic therapy using upconversion nanoparticles as remote-controlled nanotransducers.* Nature medicine, 2012. **18**(10): p. 1580-1585.
171. Ruoslahti, E. and M.D. Pierschbacher, *New perspectives in cell adhesion: RGD and integrins.* Science, 1987. **238**(4826): p. 491-497.
172. Akiyama, S.K., *Integrins in cell adhesion and signaling.* Human cell, 1996. **9**(3): p. 181-186.
173. Böger, C., et al., *Integrins αvβ3 and αvβ5 as prognostic, diagnostic, and therapeutic targets in gastric cancer.* Gastric Cancer, 2014: p. 1-12.
174. Naci, D., K. Vuori, and F. Aoudjit. *Alpha2beta1 integrin in cancer development and chemoresistance*. in *Seminars in cancer biology*. 2015. Elsevier.
175. Duperret, E.K., A. Dahal, and T.W. Ridky, *Integrin αv is necessary for skin tissue generation and SCC tumor invasion, but dispensable for tissue maintenance.* Cancer Research, 2015. **75**(15 Supplement): p. 2380-2380.
176. Lee, C.S., E.J. Ryan, and G.A. Doherty, *Gastro-intestinal toxicity of chemotherapeutics in colorectal cancer: the role of inflammation.* World J Gastroenterol, 2014. **20**(14): p. 3751-3761.
177. Trüeb, R., *Chemotherapy-induced hair loss.* Skin Therapy Lett, 2010. **15**(7): p. 5-7.

178. Valencia, P.M., et al., *Effects of ligands with different water solubilities on self-assembly and properties of targeted nanoparticles.* Biomaterials, 2011. **32**(26): p. 6226-6233.
179. Suri, S.S., H. Fenniri, and B. Singh, *Nanotechnology-based drug delivery systems.* Journal of Occupational Medicine and Toxicology, 2007. **2**(1): p. 16.
180. Ferrari, M., *Cancer nanotechnology: opportunities and challenges.* Nature Reviews Cancer, 2005. **5**(3): p. 161-171.
181. Ruoslahti, E., S.N. Bhatia, and M.J. Sailor, *Targeting of drugs and nanoparticles to tumors.* The Journal of cell biology, 2010. **188**(6): p. 759-768.
182. Mansur, A.A., S.M. de Carvalho, and H.S. Mansur, *Bioengineered Quantum Dot/Chitosan-Tripeptide Nanoconjugates for Targeting the Receptors of Cancer Cells.* International journal of biological macromolecules, 2015.
183. Wang, Z., W.-K. Chui, and P.C. Ho, *Design of a multifunctional PLGA nanoparticulate drug delivery system: evaluation of its physicochemical properties and anticancer activity to malignant cancer cells.* Pharmaceutical research, 2009. **26**(5): p. 1162-1171.
184. Gu, F.X., et al., *Targeted nanoparticles for cancer therapy.* Nano today, 2007. **2**(3): p. 14-21.
185. Wilson, M.J., et al., *Hydrogels with well-defined peptide-hydrogel spacing and concentration: impact on epithelial cell behavior.* Soft matter, 2012. **8**(2): p. 390-398.
186. Petrie, T.A., et al., *Integrin specificity and enhanced cellular activities associated with surfaces presenting a recombinant fibronectin fragment compared to RGD supports.* Biomaterials, 2006. **27**(31): p. 5459-5470.
187. Bellis, S.L., *Advantages of RGD peptides for directing cell association with biomaterials.* Biomaterials, 2011. **32**(18): p. 4205-4210.
188. Lammers, T., et al., *Drug targeting to tumors: principles, pitfalls and (pre-) clinical progress.* Journal of controlled release, 2012. **161**(2): p. 175-187.
189. Li, Z., et al., *RGD-Conjugated Dendrimer-Modified Gold Nanorods for in Vivo Tumor Targeting and Photothermal Therapy†.* Molecular pharmaceutics, 2009. **7**(1): p. 94-104.
190. Pandita, D., et al., *Gene delivery into mesenchymal stem cells: a biomimetic approach using RGD nanoclusters based on poly (amidoamine) dendrimers.* Biomacromolecules, 2011. **12**(2): p. 472-481.
191. Wang, K., et al., *Development of biodegradable polymeric implants of RGD-modified PEG-PAMAM-DOX conjugates for long-term intratumoral release.* Drug delivery, 2014(0): p. 1-11.
192. Majzoub, R.N., et al., *Uptake and transfection efficiency of PEGylated cationic liposome–DNA complexes with and without RGD-tagging.* Biomaterials, 2014. **35**(18): p. 4996-5005.
193. Dubey, P.K., et al., *Liposomes modified with cyclic RGD peptide for tumor targeting.* Journal of drug targeting, 2004. **12**(5): p. 257-264.
194. Chen, J.-X., et al., *Construction of surfactant-like tetra-tail amphiphilic peptide with RGD ligand for encapsulation of porphyrin for photodynamic therapy.* Biomaterials, 2011. **32**(6): p. 1678-1684.

195. Chen, X., et al., *A stapled peptide antagonist of MDM2 carried by polymeric micelles sensitizes glioblastoma to temozolomide treatment through p53 activation.* Journal of Controlled Release, 2015. **218**: p. 29-35.
196. Lee, S.-M., et al., *Targeted chemo-photothermal treatments of rheumatoid arthritis using gold half-shell multifunctional nanoparticles.* ACS nano, 2012. **7**(1): p. 50-57.
197. Maeda, H., et al., *Tumor vascular permeability and the EPR effect in macromolecular therapeutics: a review.* Journal of controlled release, 2000. **65**(1): p. 271-284.
198. *TINY TECH TO TREAT CANCER.*
199. Bae, K.H., H.J. Chung, and T.G. Park, *Nanomaterials for cancer therapy and imaging.* Molecules and cells, 2011. **31**(4): p. 295-302.
200. Fan Yuan, M.D., Dai Fukumura, Michael Leunig, David A. Berk, Vladimir P. Torchilin, and Rakesh K. Jain, *Vascular Permeability in a Human Tumor Xenograft: Molecular Size Dependence and Cutoff Size.* CANCER RESEARCH. , 1995. **55**: p. 3752-3756.
201. Haraldsson, B., J. Nyström, and W.M. Deen, *Properties of the glomerular barrier and mechanisms of proteinuria.* Physiological reviews, 2008. **88**(2): p. 451-487.
202. Rolfe, V., *The Physiology of the Kidneys* 2007, School of Nursing and Academic Division of Midwifery, University of Nottingham.
203. Michael Hall, A.N., Susan Smith, *A Foundation for Neonatal Care: A Multi-Disciplinary Guide edited* 2009: FSC.
204. Saba, T.M., *Physiology and physiopathology of the reticuloendothelial system.* Archives of internal medicine, 1970. **126**(6): p. 1031-1052.
205. Neuberger, T., et al., *Superparamagnetic nanoparticles for biomedical applications: possibilities and limitations of a new drug delivery system.* Journal of Magnetism and Magnetic Materials, 2005. **293**(1): p. 483-496.
206. Bamrungsap, S., et al., *Nanotechnology in therapeutics: a focus on nanoparticles as a drug delivery system.* Nanomedicine, 2012. **7**(8): p. 1253-1271.
207. Stella, B., et al., *Design of folic acid-conjugated nanoparticles for drug targeting.* Journal of pharmaceutical sciences, 2000. **89**(11): p. 1452-1464.
208. Chan, P., et al., *Synthesis and characterization of chitosan-< i> g</i>-poly (ethylene glycol)-folate as a non-viral carrier for tumor-targeted gene delivery.* Biomaterials, 2007. **28**(3): p. 540-549.
209. Shao, P., et al., *The application of thermosensitive nanocarriers in controlled drug delivery.* Journal of Nanomaterials, 2011. **2011**: p. 17.
210. Veronese, F.M. and G. Pasut, *PEGylation, successful approach to drug delivery.* Drug discovery today, 2005. **10**(21): p. 1451-1458.
211. Ashley, C.E., et al., *The targeted delivery of multicomponent cargos to cancer cells by nanoporous particle-supported lipid bilayers.* Nature materials, 2011. **10**(5): p. 389-397.
212. Li, L., et al., *Monodispersed DOTA-PEG–Conjugated Anti-TAG-72 Diabody Has Low Kidney Uptake and High Tumor-to-Blood Ratios Resulting in Improved 64Cu PET.* Journal of Nuclear Medicine, 2010. **51**(7): p. 1139-1146.

213. Morphy, R. and Z. Rankovic, *Designed multiple ligands. An emerging drug discovery paradigm.* Journal of medicinal chemistry, 2005. **48**(21): p. 6523-6543.
214. Morphy, R. and Z. Rankovic, *Fragments, network biology and designing multiple ligands.* Drug discovery today, 2007. **12**(3): p. 156-160.
215. Ruoff, R., *Graphene: Calling all chemists.* Nature Nanotechnology, 2008. **3**(1): p. 10-11.
216. Wang, Y., et al., *Graphene and graphene oxide: biofunctionalization and applications in biotechnology.* Trends in biotechnology, 2011. **29**(5): p. 205-212.
217. Novoselov, K.S., et al., *Electric field effect in atomically thin carbon films.* science, 2004. **306**(5696): p. 666-669.
218. Wang, H., T. Maiyalagan, and X. Wang, *Review on recent progress in nitrogen-doped graphene: synthesis, characterization, and its potential applications.* Acs Catalysis, 2012. **2**(5): p. 781-794.
219. Allen Mattew, J., C. Tung Vincent, and B. Kaner Richard, *Honeycomb carbon a review of graphene.* Chem. Rev, 2010. **110**(1): p. 132-145.
220. Dikin, e.a., *Preparation and characterization of graphene oxide paper.* Nature, 2007. **448**(7152): p. 457-460.
221. Kuila, T., et al., *Chemical functionalization of graphene and its applications.* Progress in Materials Science, 2012. **57**(7): p. 1061-1105.
222. Yang, e.a., *Nano-graphene in biomedicine: theranostic applications.* Chemical Society Reviews, 2013. **42**(2): p. 530-547.
223. Rong, e.a., *Photosensitizer loaded nano-graphene for multimodality imaging guided tumor photodynamic therapy.* Theranostics, 2014. **4**(3): p. 229-239.
224. Shen, e.a., *Biomedical applications of graphene.* Theranostics, 2012. **2**(3): p. 283.
225. Sumer, B. and J. Gao, *Theranostic nanomedicine for cancer.* Nanomedicine, 2008. **3**(2): p. 137-140.
226. Goenka, e.a., *Graphene-based nanomaterials for drug delivery and tissue engineering.* Journal of Controlled Release, 2014. **173**: p. 75-88.
227. Shi, e.a., *Surface engineering of graphene-based nanomaterials for biomedical applications.* Bioconjugate chemistry, 2014. **25**(9): p. 1609-1619.
228. Huang, X., et al., *Graphene-based electrodes.* Advanced Materials, 2012. **24**(45): p. 5979-6004.
229. Huang, X., et al., *Graphene-based composites.* Chemical Society Reviews, 2012. **41**(2): p. 666-686.
230. Hamilton, C. and C. Functionalization, *Coating of Carbon Nanomaterials*. 2009, PhD Thesis, University of Rice.
231. Liu, J., L. Cui, and D. Losic, *Graphene and graphene oxide as new nanocarriers for drug delivery applications.* Acta biomaterialia, 2013. **9**(12): p. 9243-9257.
232. Chung, C., et al., *Biomedical applications of graphene and graphene oxide.* Accounts of chemical research, 2013. **46**(10): p. 2211-2224.
233. Shao, Y., et al., *Graphene based electrochemical sensors and biosensors: a review.* Electroanalysis, 2010. **22**(10): p. 1027-1036.

234. Mohanty, N. and V. Berry, *Graphene-based single-bacterium resolution biodevice and DNA transistor: interfacing graphene derivatives with nanoscale and microscale biocomponents.* Nano letters, 2008. **8**(12): p. 4469-4476.
235. Patil, A.J., et al., *Aqueous Stabilization and Self-Assembly of Graphene Sheets into Layered Bio-Nanocomposites using DNA.* Advanced Materials, 2009. **21**(31): p. 3159-3164.
236. Liang, H., et al., *Functional DNA-containing nanomaterials: cellular applications in biosensing, imaging, and targeted therapy.* Accounts of chemical research, 2014. **47**(6): p. 1891-1901.
237. Yang, K., L. Feng, and Z. Liu, *The advancing uses of nano-graphene in drug delivery.* Expert opinion on drug delivery, 2015. **12**(4): p. 601-612.
238. Hsieh, C.-J., et al., *A Graphene Oxide-Based Nanocarrier Combined with a pH-Sensitive Tracer: a Vehicle for Concurrent pH Sensing and pH-Responsive Oligonucleotide Delivery.* ACS applied materials & interfaces, 2015.
239. Sun, X., et al., *Nano-graphene oxide for cellular imaging and drug delivery.* Nano research, 2008. **1**(3): p. 203-212.
240. Liu, Z., et al., *PEGylated nanographene oxide for delivery of water-insoluble cancer drugs.* Journal of the American Chemical Society, 2008. **130**(33): p. 10876-10877.
241. Zhang, L., et al., *Functional graphene oxide as a nanocarrier for controlled loading and targeted delivery of mixed anticancer drugs.* Small, 2010. **6**(4): p. 537-544.
242. Yang, K., et al., *Graphene in mice: ultrahigh in vivo tumor uptake and efficient photothermal therapy.* Nano letters, 2010.
243. Sun, X. and e. al, *Nano-graphene oxide for cellular imaging and drug delivery.* Nano research, 2008. **1**(3): p. 203-212.
244. Smith, B.C., *Fundamentals of Fourier transform infrared spectroscopy*. 2011: CRC press.
245. Weckhuysen, B.M., *Ultraviolet-visible spectroscopy.* In situ Spectroscopy of Catalysts, American Scientific Publishers, Stevenson Ranch, 2004: p. 255-270.
246. Lakowicz, J.R., *Principles of fluorescence spectroscopy*. 2013: Springer Science & Business Media.
247. Owen-Reece, H., et al., *Near infrared spectroscopy.* British journal of anaesthesia, 1999. **82**(3): p. 418-426.
248. Winter, A., *Organic chemistry I for dummies*. 2005: John Wiley & Sons.
249. Förster, H., *UV/vis spectroscopy*, in *Characterization I*. 2004, Springer. p. 337-426.
250. Perkampus, H.-H., H.-C. Grinter, and T. Threlfall, *UV-VIS Spectroscopy and its Applications*. 1992: Springer.
251. Valeur, B. and M.N. Berberan-Santos, *Molecular fluorescence: principles and applications*. 2012: John Wiley & Sons.
252. Lackowicz, J., *Principle of Fluorescence Spectroscopy, 2006.* Chapter. **1**: p. 10.
253. Weiss, S., *Fluorescence spectroscopy of single biomolecules.* Science, 1999. **283**(5408): p. 1676-1683.
254. Modes, V., *Vibrational Modes.*

255. Stuart, B., *Infrared spectroscopy*. 2005: Wiley Online Library.
256. Griffiths, P.R. and J.A. De Haseth, *Fourier transform infrared spectrometry*. Vol. 171. 2007: John Wiley & Sons.
257. Levitt, M.H., *Nuclear spin relaxation.* Resonance, 2015. **20**(11): p. 986-994.
258. Levitt, M.H., *Spin dynamics: basics of nuclear magnetic resonance*. 2001: John Wiley & Sons.
259. Günther, H., *NMR spectroscopy: basic principles, concepts and applications in chemistry*. 2013: John Wiley & Sons.
260. Minsky, M., *Microscopy apparatus*. 1961, Google Patents.
261. Murphy, D.B., *Fundamentals of light microscopy and electronic imaging*. 2002: John Wiley & Sons.
262. Banks, P., *Development of the Optical Microscope*. 2014: Biotek. p. 1-10.
263. Lichtman, J.W. and J.-A. Conchello, *Fluorescence microscopy.* Nature methods, 2005. **2**(12): p. 910-919.
264. Bassell, G.J., Y. Oleynikov, and R.H. Singer, *The travels of mRNAs through all cells large and small.* The FASEB Journal, 1999. **13**(3): p. 447-454.
265. Hibbs, A.R., *Confocal microscopy for biologists*. 2004: Springer Science & Business Media.
266. Holmes, T., D. Biggs, and A. Abu-Tarif, *Handbook of biological confocal microscopy.* Light microscopic images reconstructed by maximum likelihood deconvolution, 2006: p. 389-402.
267. Wilson, T., *Optical sectioning in confocal fluorescent microscopes.* Journal of Microscopy, 1989. **154**(2): p. 143-156.
268. Reynaud, K., et al., *Confocal microscopy: principles and applications to the field of reproductive biology.* Folia histochemica et cytobiologica/Polish Academy of Sciences, Polish Histochemical and Cytochemical Society, 2000. **39**(2): p. 75-85.
269. Williams, D.B. and C.B. Carter, *The transmission electron microscope*, in *Transmission electron microscopy*. 1996, Springer. p. 3-17.
270. Williams, D.B. and C.B. Carter, *The transmission electron microscope*. 1996: Springer.
271. Bozzola, J.J. and L.D. Russell, *Electron microscopy: principles and techniques for biologists*. 1999: Jones & Bartlett Learning.
272. *Nanotechnology: A Brief Overview , HTTP://MAPPINGIGNORANCE.ORG/2013/12/23/BESSEL-BEAM-PLANE-ILLUMINATION-MICROSCOPY-ANOTHER-SMART-SOLUTION-FOR-AN-OLD-CHALLENGE/*. Available from: HTTP://BARRETT-GROUP.MCGILL.CA/TUTORIALS/NANOTECHNOLOGY/NANO02.HTM.
273. Suganuma, T., *Measurement of surface topography using SEM with two secondary electron detectors.* Journal of electron microscopy, 1985. **34**(4): p. 328-337.
274. Sealy, C.P., M.R. Castell, and P.R. Wilshaw, *Mechanism for secondary electron dopant contrast in the SEM.* Journal of electron microscopy, 2000. **49**(2): p. 311-321.

275. Goldstein, J., et al., *Scanning electron microscopy and X-ray microanalysis: a text for biologists, materials scientists, and geologists*. 2012: Springer Science & Business Media.
276. Elings, V.B. and J.A. Gurley, *Tapping atomic force microscope*. 1995, Google Patents.
277. Radmacher, M., *Measuring the elastic properties of biological samples with the AFM.* IEEE Engineering in Medicine and Biology Magazine, 1997. **16**(2): p. 47-57.
278. Jandt, K.D., *Atomic force microscopy of biomaterials surfaces and interfaces.* Surface Science, 2001. **491**(3): p. 303-332.
279. Nonnenmacher, M. and H. Wickramasinghe, *Scanning probe microscopy of thermal conductivity and subsurface properties.* Applied Physics Letters, 1992. **61**(2): p. 168-170.
280. Prime, R.B., et al., *Thermogravimetric analysis (TGA).* Thermal Analysis of Polymers: Fundamentals and Applications, 2009: p. 241-317.
281. Beyler, C.L. and M.M. Hirschler, *Thermal decomposition of polymers.* SFPE handbook of fire protection engineering, 2002. **2**: p. 110-131.
282. Dreyer, e.a., *Harnessing the chemistry of graphene oxide.* Chemical Society Reviews, 2014. **43**(15): p. 5288-5301.
283. Parab, H.J., et al., *Biosensing, cytotoxicity, and cellular uptake studies of surface-modified gold nanorods.* The Journal of Physical Chemistry C, 2009. **113**(18): p. 7574-7578.
284. Coluci, e.a., *Noncovalent interaction with graphene oxide: the crucial role of oxidative debris.* The Journal of Physical Chemistry 2014. **118**(4): p. 2187-2193.
285. Loh, K.P. and e. al, *Graphene oxide as a chemically tunable platform for optical applications.* Nature chemistry, 2010. **2**(12): p. 1015-1024.
286. Huang, X., et al., *Graphene-based materials: synthesis, characterization, properties, and applications.* Small, 2011. **7**(14): p. 1876-1902.
287. Tan, C., X. Huang, and H. Zhang, *Synthesis and applications of graphene-based noble metal nanostructures.* Materials Today, 2013. **16**(1): p. 29-36.
288. Kim, e.a., *Two dimensional soft material: new faces of graphene oxide.* Accounts of chemical research, 2012. **45**(8): p. 1356-1364.
289. Aboutalebi, e.a., *Spontaneous formation of liquid crystals in ultralarge graphene oxide dispersions.* Advanced Functional Materials, 2011. **21**(15): p. 2978-2988.
290. Kim, e.a., *Graphene oxide sheets at interfaces.* Journal of the American Chemical Society, 2010. **132**(23): p. 8180-8186.
291. Park, S., et al., *Hydrazine-reduction of graphite-and graphene oxide.* Carbon, 2011. **49**(9): p. 3019-3023.
292. Kaminska, e.a., *Reduction and functionalization of graphene oxide sheets using biomimetic dopamine derivatives in one step.* ACS applied materials & interfaces, 2012. **4**(2): p. 1016-1020.
293. Compton, O.C. and S.T. Nguyen, *Graphene Oxide, Highly Reduced Graphene Oxide, and Graphene: Versatile Building Blocks for Carbon-Based Materials.* small, 2010. **6**(6): p. 711-723.

294. Zhang, e.a., *Functional graphene oxide as a nanocarrier for controlled loading and targeted delivery of mixed anticancer drugs.* Small, 2010. **6**(4): p. 537-544.
295. Qi, e.a., *Size-specified graphene oxide sheets: ultrasonication assisted preparation and characterization.* Journal of Materials Science, 2014. **49**(4): p. 1785-1793.
296. Cai, e.a., *Methods of graphite exfoliation.* Journal of Materials Chemistry, 2012. **22**(48): p. 24992-25002.
297. Sun, e.a., *Actuation triggered exfoliation of graphene oxide at low temperature for electrochemical capacitor applications.* Carbon, 2014. **68**: p. 748-754.
298. Schlierf, e.a., *Exfoliation of graphene with an industrial dye: teaching an old dog new tricks.* 2D Materials, 2014. **1**(3): p. 035006-035019.
299. Acik, M. and Y.J. Chabal, *A review on thermal exfoliation of graphene oxide.* Journal of Materials Science Research, 2013. **2**(1): p. 101-112.
300. Barroso-Bujans, F., et al., *Permanent adsorption of organic solvents in graphite oxide and its effect on the thermal exfoliation.* Carbon, 2010. **48**(4): p. 1079-1087.
301. Si, Y. and E.T. Samulski, *Synthesis of water soluble graphene.* Nano letters, 2008. **8**(6): p. 1679-1682.
302. Mu, e.a., *Size-dependent cell uptake of protein-coated graphene oxide nanosheets.* ACS applied materials & interfaces, 2012. **4**(4): p. 2259-2266.
303. Botas, e.a., *Optimization of the size and yield of graphene oxide sheets in the exfoliation step.* Carbon, 2013. **63**: p. 576-578.
304. He, e.a., *Processable aqueous dispersions of graphene stabilized by graphene quantum dots.* Chemistry of Materials, 2014. **27**(1): p. 218-226.
305. Sun, X. and e. al, *Monodisperse chemically modified graphene obtained by density gradient ultracentrifugal rate separation.* ACS nano, 2010. **4**(6): p. 3381-3389.
306. Wiederseiner, e.a., *Refractive-index and density matching in concentrated particle suspensions: a review.* Experiments in fluids, 2011. **50**(5): p. 1183-1206.
307. Ammons, e.a., *An apparatus to control and automate the formation of continuous density gradients.* Analytical biochemistry, 2012. **427**(2): p. 124-126.
308. Lee, e.a., *Liquid crystal size selection of large-size graphene oxide for size-dependent N-doping and oxygen reduction catalysis.* ACS nano, 2014. **8**(9): p. 9073-9080.
309. Wang, e.a., *Size fractionation of graphene oxide sheets by pH-assisted selective sedimentation.* Journal of the American Chemical Society, 2011. **133**(16): p. 6338-6342.
310. Chen, J. and e. al, *Size Fractionation of Graphene Oxide Sheets via Filtration through Track-Etched Membranes.* Advanced Materials, 2015. **27**: p. 3654–3660.
311. Zhang, W. and e. al, *Size fractionation of graphene oxide sheets by the polar solvent-selective natural deposition method.* RSC Advances, 2015. **5**(1): p. 146-152.
312. Chen, J. and e. al, *Size Fractionation of Graphene Oxide Sheets via Filtration through Track-Etched Membranes.* Advanced Materials, 2015.

313. Stankovich, S. and e. al, *Synthesis of graphene-based nanosheets via chemical reduction of exfoliated graphite oxide.* Carbon, 2007. **45**(7): p. 1558-1565.
314. Yu, Z. and e. al, *Dual function of Rpn5 in two PCI complexes, the 26S proteasome and COP9 signalosome.* Molecular biology of the cell, 2011. **22**(7): p. 911-920.
315. Yang, W. and e. al, *Stirring-induced aggregation of graphene in suspension.* New Journal of Chemistry, 2011. **35**(4): p. 780-783.
316. Green, A.A. and M.C. Hersam, *Solution phase production of graphene with controlled thickness via density differentiation.* Nano letters, 2009. **9**(12): p. 4031-4036.
317. Cvjetkovic, A. and e. al, *The influence of rotor type and centrifugation time on the yield and purity of extracellular vesicles.* Journal of extracellular vesicles, 2014. **3**: p. 23111-23122.
318. Stankovich, S., et al., *Synthesis of graphene-based nanosheets via chemical reduction of exfoliated graphite oxide.* carbon, 2007. **45**(7): p. 1558-1565.
319. Montibon, E., *Preparation of electroconductive paper by deposition of conducting polymer.* 2009.
320. Whitby, R.L. and e. al, *Driving forces of conformational changes in single-layer graphene oxide.* ACS nano, 2012. **6**(5): p. 3967-3973.
321. Abramson, H.A., *ELECTROKINETIC PHENOMENA VI. RELATIONSHIP BETWEEN ELECTRIC MOBILITY, CHARGE, AND TITRATION OF PROTEINS.* The Journal of general physiology, 1932. **15**(5): p. 575-603.
322. Anderson, R., et al., *Potocytosis: sequestration and transport of small molecules by caveolae.* Science, 1992. **255**(5043): p. 410-411.
323. Paredes, J., et al., *Graphene oxide dispersions in organic solvents.* Langmuir, 2008. **24**(19): p. 10560-10564.
324. Fu, L., G. Lai, and A. Yu, *Electroanalysis of Dopamine Using Polydopamine Functionalized Reduced Graphene Oxide-Gold Nanocomposite.*
325. Akhavan, O., E. Ghaderi, and H. Emamy, *Nontoxic concentrations of PEGylated graphene nanoribbons for selective cancer cell imaging and photothermal therapy.* Journal of Materials Chemistry, 2012. **22**(38): p. 20626-20633.
326. El-Gammal, B. and K. Allan, *Ion exchange reversibility of some radionuclides on zirconium tungstosuccinate and zirconium tungstosalicylate at their solid-liquid interfaces.* Separation Science and Technology, 2012. **47**(1): p. 131-146.
327. Ren, P.-G., et al., *Temperature dependence of graphene oxide reduced by hydrazine hydrate.* Nanotechnology, 2010. **22**(5): p. 055705.
328. Zhu, Y., et al., *Microwave assisted exfoliation and reduction of graphite oxide for ultracapacitors.* Carbon, 2010. **48**(7): p. 2118-2122.
329. Ganguly, A., et al., *Probing the thermal deoxygenation of graphene oxide using high-resolution in situ X-ray-based spectroscopies.* The Journal of Physical Chemistry C, 2011. **115**(34): p. 17009-17019.
330. Stankovich, S., et al., *Synthesis and exfoliation of isocyanate-treated graphene oxide nanoplatelets.* Carbon, 2006. **44**(15): p. 3342-3347.
331. Raza, H., *Graphene nanoelectronics: Metrology, synthesis, properties and applications*. 2012: Springer Science & Business Media. 578.

332. Han, F., et al., *A study on near-UV blue photoluminescence in graphene oxide prepared by Langmuir–Blodgett method.* Applied Surface Science, 2015. **345**: p. 18-23.
333. Elham, B., David D. , Alastair S., *Graphene Oxide as a photoluminated carrier.* Materials Today: Proceedings. , 2015. **Accepted**.
334. Shimada, M. and e. al, *Optical Properties of Disilane-Bridged Donor–Acceptor Architectures: Strong Effect of Substituents on Fluorescence and Nonlinear Optical Properties.* Journal of the American Chemical Society, 2015. **137**(3): p. 1024-1027.
335. Eda, G., et al., *Blue photoluminescence from chemically derived graphene oxide.* Advanced Materials, 2010. **22**(4): p. 505.
336. Loh, K.P., et al., *Graphene oxide as a chemically tunable platform for optical applications.* Nature chemistry, 2010. **2**(12): p. 1015-1024.
337. Pan, D., et al., *Hydrothermal route for cutting graphene sheets into blue-luminescent graphene quantum dots.* Advanced Materials, 2010. **22**(6): p. 734-738.
338. Shang, J., et al., *The origin of fluorescence from graphene oxide.* Scientific reports, 2012. **2**.
339. Sheng, L., et al., *PVP-coated graphene oxide for selective determination of ochratoxin A via quenching fluorescence of free aptamer.* Biosensors and Bioelectronics, 2011. **26**(8): p. 3494-3499.
340. Kim, J., et al., *Visualizing graphene based sheets by fluorescence quenching microscopy.* Journal of the American Chemical Society, 2009. **132**(1): p. 260-267.
341. Luo, Z., et al., *Photoluminescence and band gap modulation in graphene oxide.* Applied physics letters, 2009. **94**(11): p. 111909.
342. Yang, X., et al., *High-efficiency loading and controlled release of doxorubicin hydrochloride on graphene oxide.* The Journal of Physical Chemistry C, 2008. **112**(45): p. 17554-17558.
343. Li, J., C.-y. Liu, and Y. Liu, *Au/graphene hydrogel: synthesis, characterization and its use for catalytic reduction of 4-nitrophenol.* Journal of Materials Chemistry, 2012. **22**(17): p. 8426-8430.
344. Skoog, D., F. Holler, and T. Nieman, *Principles of Instrumental Analysis; Hartcourt Brace & Company: Philadelphia, 1998; Chapter 13.* There is no corresponding record for this reference.
345. Yang, F., et al., *Influence of pH on the fluorescence properties of graphene quantum dots using ozonation pre-oxide hydrothermal synthesis.* Journal of Materials Chemistry, 2012. **22**(48): p. 25471-25479.
346. Galande, C., et al., *Quasi-molecular fluorescence from graphene oxide.* Scientific reports, 2011. **1**.
347. Magadala, P. and M. Amiji, *Epidermal growth factor receptor-targeted gelatin-based engineered nanocarriers for DNA delivery and transfection in human pancreatic cancer cells.* The AAPS journal, 2008. **10**(4): p. 565-576.

348. Kelemen, L.E., *The role of folate receptor α in cancer development, progression and treatment: cause, consequence or innocent bystander?* International journal of cancer, 2006. **119**(2): p. 243-250.
349. Bhattacharya, R., et al., *Attaching folic acid on gold nanoparticles using noncovalent interaction via different polyethylene glycol backbones and targeting of cancer cells.* Nanomedicine: Nanotechnology, Biology and Medicine, 2007. **3**(3): p. 224-238.
350. Shen, Z., et al., *Improved drug targeting of cancer cells by utilizing actively targetable folic acid-conjugated albumin nanospheres.* Pharmacological Research, 2011. **63**(1): p. 51-58.
351. Sulistio, A., et al., *Folic Acid Conjugated Amino Acid-Based Star Polymers for Active Targeting of Cancer Cells.* Biomacromolecules, 2011. **12**(10): p. 3469-3477.
352. Varma, R. and S. Mayor, *GPI-anchored proteins are organized in submicron domains at the cell surface.* Nature, 1998. **394**(6695): p. 798-801.
353. Daniel J. O'Shannessy1, E.B.S., Earl Albone1, Xin Cheng1, Young Chul Park1, Brian E. Tomkowicz2, Yoshitomo Hamuro3, Thomas O. Kohl4, Tracy M. Forsyth4, Robert Smale5, Yao-Shi Fu5, Nicholas C. Nicolaides1, *Characterization of the Human Folate Receptor Alpha Via Novel Antibody-Based Probes.* Oncotarget, 2011. **2**: p. 1227 - 1243.
354. Brannon-Peppas, L. and J.O. Blanchette, *Nanoparticle and targeted systems for cancer therapy.* Advanced drug delivery reviews, 2004. **56**(11): p. 1649-1659.
355. Vergote, I.B., C. Marth, and R.L. Coleman, *Role of the folate receptor in ovarian cancer treatment: evidence, mechanism, and clinical implications.* Cancer and Metastasis Reviews, 2015. **34**(1): p. 41-52.
356. Morris, R., et al., *Phase II study of treatment of advanced ovarian cancer with folate-receptor-targeted therapeutic (vintafolide) and companion SPECT-based imaging agent (99mTc-etarfolatide).* Annals of oncology, 2014. **25**(4): p. 852-858.
357. Wen, Y., et al., *Immunotherapy targeting folate receptor induces cell death associated with autophagy in ovarian cancer.* Clinical Cancer Research, 2015. **21**(2): p. 448-459.
358. Wang, F., et al., *The functions and applications of RGD in tumor therapy and tissue engineering.* International journal of molecular sciences, 2013. **14**(7): p. 13447-13462.
359. Gottesman, M.M., *Mechanisms of cancer drug resistance.* Annual review of medicine, 2002. **53**(1): p. 615-627.
360. Lucock, M., *Folic acid: nutritional biochemistry, molecular biology, and role in disease processes.* Molecular genetics and metabolism, 2000. **71**(1-2): p. 121-138.
361. Lu, Y. and P.S. Low, *Folate-mediated delivery of macromolecular anticancer therapeutic agents.* Advanced drug delivery reviews, 2002. **54**(5): p. 675-693.
362. Mizejewski, G.J., *Role of integrins in cancer: survey of expression patterns.* Experimental Biology and Medicine, 1999. **222**(2): p. 124-138.

363. Giancotti, F.G. and E. Ruoslahti, *Integrin signaling.* Science, 1999. **285**(5430): p. 1028-1033.
364. Xiao, L., H. Wang, and Z.D. Schultz, *Selective Detection of RGD-Integrin Binding in Cancer Cells Using Tip Enhanced Raman Scattering Microscopy.* Analytical chemistry, 2016.
365. Dreyer, D.R., et al., *The chemistry of graphene oxide.* Chemical Society Reviews, 2010. **39**(1): p. 228-240.
366. Nobs, L., et al., *Current methods for attaching targeting ligands to liposomes and nanoparticles.* Journal of pharmaceutical sciences, 2004. **93**(8): p. 1980-1992.
367. Guo, W. and R.J. Lee, *Receptor-targeted gene delivery viafolate-conjugated polyethylenimine.* Aaps Pharmsci, 1999. **1**(4): p. 20-26.
368. Dray, N., et al., *Large-scale live imaging of adult neural stem cells in their endogenous niche.* Development, 2015. **142**(20): p. 3592-3600.
369. Lorenzo, C., et al., *Live cell division dynamics monitoring in 3D large spheroid tumor models using light sheet microscopy.* Cell division, 2011. **6**(1): p. 1.
370. Champion, J.A. and S. Mitragotri, *Role of target geometry in phagocytosis.* Proceedings of the National Academy of Sciences of the United States of America, 2006. **103**(13): p. 4930-4934.
371. Conner, S.D. and S.L. Schmid, *Regulated portals of entry into the cell.* Nature, 2003. **422**(6927): p. 37-44.
372. Yan, Y., et al., *Engineering particles for therapeutic delivery: prospects and challenges.* ACS nano, 2012. **6**(5): p. 3663-3669.
373. Simons, K. and D. Toomre, *Lipid rafts and signal transduction.* Nature Reviews Molecular Cell Biology, 2000. **1**(1): p. 31-39.
374. Bijnsdorp, I.V., E. Giovannetti, and G.J. Peters, *Analysis of drug interactions.* Cancer Cell Culture: Methods and Protocols, 2011: p. 421-434.
375. Chou, T.-C., *Drug combination studies and their synergy quantification using the Chou-Talalay method.* Cancer research, 2010. **70**(2): p. 440-446.
376. Lehár, J., et al., *Synergistic drug combinations tend to improve therapeutically relevant selectivity.* Nature biotechnology, 2009. **27**(7): p. 659-666.
377. Hu, C.-M.J. and L. Zhang, *Nanoparticle-based combination therapy toward overcoming drug resistance in cancer.* Biochemical pharmacology, 2012. **83**(8): p. 1104-1111.
378. Milano, G., J. Spano, and B. Leyland-Jones, *EGFR-targeting drugs in combination with cytotoxic agents: from bench to bedside, a contrasted reality.* British journal of cancer, 2008. **99**(1): p. 1-5.
379. Bergamo, A., et al., *Preclinical combination therapy of the investigational drug NAMI-A+ with doxorubicin for mammary cancer.* Investigational new drugs, 2015. **33**(1): p. 53-63.
380. Mayer, L.D., et al., *Ratiometric dosing of anticancer drug combinations: controlling drug ratios after systemic administration regulates therapeutic activity in tumor-bearing mice.* Molecular cancer therapeutics, 2006. **5**(7): p. 1854-1863.

381. Ryall, K.A. and A. Tan, *Systems biology approaches for advancing the discovery of effective drug combinations.* J. Cheminformatics, 2015. **7**: p. 7.
382. Juzeniene, A., et al., *The action spectrum for folic acid photodegradation in aqueous solutions.* Journal of Photochemistry and Photobiology B: Biology, 2013. **126**: p. 11-16.
383. Yang, X., et al., *The preparation of functionalized graphene oxide for targeted intracellular delivery of siRNA.* Journal of Materials Chemistry, 2012. **22**(14): p. 6649-6654.
384. Rozenberg, M. and G. Shoham, *FTIR spectra of solid poly-l-lysine in the stretching NH mode range.* Biophysical chemistry, 2007. **125**(1): p. 166-171.
385. Zhang, Y., N. Kohler, and M. Zhang, *Surface modification of superparamagnetic magnetite nanoparticles and their intracellular uptake.* Biomaterials, 2002. **23**(7): p. 1553-1561.
386. Wang, Y., et al., *High-quality reduced graphene oxide-nanocrystalline platinum hybrid materials prepared by simultaneous co-reduction of graphene oxide and chloroplatinic acid.* Nanoscale Research Letters, 2011. **6**(1): p. 1.
387. Paredes, J., et al., *Graphene oxide dispersions in organic solvents.* Langmuir, 2008. **24**(19): p. 10560-10564.
388. Shen, J., et al., *Facile synthesis and application of Ag-chemically converted graphene nanocomposite.* Nano research, 2010. **3**(5): p. 339-349.
389. Pan, S. and I.A. Aksay, *Factors controlling the size of graphene oxide sheets produced via the graphite oxide route.* ACS nano, 2011. **5**(5): p. 4073-4083.
390. Mukhopadhyay, A., et al., *A facile synthesis of PEG-coated magnetite (Fe3O4) nanoparticles and their prevention of the reduction of cytochrome C.* ACS applied materials & interfaces, 2011. **4**(1): p. 142-149.
391. Shukla, R., et al., *Tumor microvasculature targeting with dendrimer-entrapped gold nanoparticles.* Soft Matter, 2008. **4**(11): p. 2160-2163.
392. Liu, F., J.Y. Choi, and T.S. Seo, *Graphene oxide arrays for detecting specific DNA hybridization by fluorescence resonance energy transfer.* Biosensors and Bioelectronics, 2010. **25**(10): p. 2361-2365.
393. Aust, O., et al., *Lycopene oxidation product enhances gap junctional communication.* Food and Chemical Toxicology, 2003. **41**(10): p. 1399-1407.
394. Sengupta, P., S. Ghosh, and T.C. Mak, *A new route for the synthesis of bis (pyridine dicarboxylato) bis (triphenylphosphine) complexes of ruthenium (II) and X-ray structural characterisation of the biologically active trans-[Ru (PPh 3) 2 (L 1 H) 2](L 1 H 2= pyridine 2, 3-dicarboxylic acid).* Polyhedron, 2001. **20**(9): p. 975-980.
395. Mitchell, M.L. and R.A. Dluhy, *In situ FT-IR investigation of phospholipid monolayer phase transitions at the air water interface.* Journal of the American Chemical Society, 1988. **110**(3): p. 712-718.
396. Gurunathan, S., et al., *Enhanced green fluorescent protein-mediated synthesis of biocompatible graphene.* Journal of nanobiotechnology, 2014. **12**(1): p. 41.
397. Vallet-Regí, M., F. Balas, and D. Arcos, *Mesoporous materials for drug delivery.* Angewandte Chemie International Edition, 2007. **46**(40): p. 7548-7558.

398. Reddel, R., et al., *Immortalized human bronchial epithelial mesothelial cell lines.* USA: Department of Health and Human Services, 1989. **4885238**.
399. Liu, J.J.S.-C. and M. Karasek, *Isolation and growth of adult human epidermal keratinocytes in cell culture.* Journal of Investigative Dermatology, 1978. **71**(2): p. 157-164.
400. Johnson, L.F., C.L. Fuhrman, and H.T. Abelson, *Resistance of resting 3T6 mouse fibroblasts to methotrexate cytotoxicity.* Cancer research, 1978. **38**(8): p. 2408-2412.
401. Herman, S., N. Zurgil, and M. Deutsch, *Low dose methotrexate induces apoptosis with reactive oxygen species involvement in T lymphocytic cell lines to a greater extent than in monocytic lines.* Inflammation Research, 2005. **54**(7): p. 273-280.
402. Germain, E., et al., *Enhancement of doxorubicin cytotoxicity by polyunsaturated fatty acids in the human breast tumor cell line MDA-MB-231: relationship to lipid peroxidation.* International journal of cancer, 1998. **75**(4): p. 578-583.
403. Speth, P., Q. Van Hoesel, and C. Haanen, *Clinical pharmacokinetics of doxorubicin.* Clinical pharmacokinetics, 1988. **15**(1): p. 15-31.
404. Monks, A., et al., *Feasibility of a high-flux anticancer drug screen using a diverse panel of cultured human tumor cell lines.* Journal of the National Cancer Institute, 1991. **83**(11): p. 757-766.
405. Wang, S., et al., *Doxorubicin induces apoptosis in normal and tumor cells via distinctly different mechanisms intermediacy of H2O2-and p53-dependent pathways.* Journal of Biological Chemistry, 2004. **279**(24): p. 25535-25543.
406. Pinedo, H.M., et al., *The reversal of methotrexate cytotoxicity to mouse bone marrow cells by leucovorin and nucleosides.* Cancer research, 1976. **36**(12): p. 4418-4424.
407. Chang, B., D. Brenner, and R. Gutman, *Cellular pharmacology of doxorubicinol alone and combined with verapamil in pancreatic cancer cell lines.* Anticancer research, 1988. **9**(2): p. 341-345.
408. Elham, Dave, and Alastair, *Graphene Oxide as a Photoluminated Carrier.* Materials Today: Proceedings, 2016. **3**(2): p. 240-244.
409. Nel, A.E., et al., *Understanding biophysicochemical interactions at the nano–bio interface.* Nature materials, 2009. **8**(7): p. 543-557.
410. Loessner, D., et al., *Bioengineered 3D platform to explore cell–ECM interactions and drug resistance of epithelial ovarian cancer cells.* Biomaterials, 2010. **31**(32): p. 8494-8506.
411. Bissell, M.J. and D. Radisky, *Putting tumours in context.* Nature Reviews Cancer, 2001. **1**(1): p. 46-54.
412. Kenny, H.A., et al., *Organotypic models of metastasis: A three-dimensional culture mimicking the human peritoneum and omentum for the study of the early steps of ovarian cancer metastasis*, in *Ovarian Cancer*. 2009, Springer. p. 335-351.
413. Mo, R., et al., *ATP-responsive DNA-graphene hybrid nanoaggregates for anticancer drug delivery.* Biomaterials, 2015. **50**: p. 67-74.

414. Dong, H., et al., *Surface-engineered graphene-based nanomaterials for drug delivery.* Journal of biomedical nanotechnology, 2014. **10**(9): p. 2086-2106.